DISS. ETH NO. 18575

Quantitative Assessment of Atherosclerosis in Coronary Arteries

A dissertation submitted to

ETH ZURICH

for the degree of

Doctor of Sciences (Dr. sc. ETH Zürich)

presented by

Stefan Saur
Dipl.-Ing. Elektrotechnik und Informationstechnik
born December 1, 1979
citizen of Germany

accepted on the recommendation of

Prof. Dr. Gábor Székely, examiner
Prof. Dr.-Ing. Horst Hahn, co-examiner
PD Dr. med. Hatem Alkadhi, co-examiner
Prof. Dr. Philippe Cattin, co-examiner

2009

TO MY PARENTS AND GRANDPARENTS.

Abstract

Cardiovascular diseases represent the leading cause of death in developed countries. In the presence of atherosclerosis, plaques develop by the accumulation of lipid or calcified deposits in the vessel walls. Coronary plaques may rupture and lead to acute coronary syndromes. Therefore, early detection and quantification of plaques is of high interest.

These days, computed tomography (CT) has emerged as a robust and accurate modality for the assessment of coronary arteries and the detection and characterization of coronary plaques. For the assessment of atherosclerosis, a reader – supported by software tools – searches the acquired data for characteristic anomalies. The decision for the presence of plaques is then mainly based upon the reader's experience. Once found, several scores exist for a detailed analysis. However, this manual assessment induces errors due to the absence of clear decision criteria. As a consequence, the decisions between different readers vary. Furthermore, the CT intensities even change between examinations such that these additional variabilities also effect measurements.

This thesis aims in reducing these aforementioned variabilities by presenting automatic and semi-automatic algorithms or tools for an improved assessment of atherosclerosis in coronary arteries. The work at hand advances the state-of-the-art with four main contributions.

Firstly, a robust method for the volumetric assessment of calcified plaques in non-enhanced CT data sets is presented that overcomes the variabilities and parameter dependencies of the currently applied method.

The second contribution comprehends the development of a framework for the automatic extraction of calcified coronary plaques. For this purpose, new automatic and semi-automatic algorithms for the extraction of anatomical features in CT data sets are introduced.

The third contribution is given for the assessment of noncalcified plaques. Dual Energy CT – the image acquisition at two different energy levels – is used to propose an algorithm that enhances the contrast between tissues as compared to a conventional CT examination.

The final contribution lies in the research of spatial plaque distribution patterns with frequent itemset mining. Knowledge about these patterns is used to propose a guided review of coronary segments for improving the manual detection of coronary plaques.

Zusammenfassung

Koronare Herzkrankheiten sind die Haupttodesursache in entwickelten Ländern. Im Falle einer Atherosklerose entstehen Plaques durch die Akkumulation von fettigen oder kalzifierten Ablagerungen in Gefäßwänden. Da diese Plaques aufplatzen und zu akuten Herzsyndromen führen können, ist deren frühzeitige Erkennung von großem Interesse.

Die Computertomographie (CT) hat sich als zuverlässige und genaue Modalität zur Beurteilung von Koronararterien und zur Detektion und Charakterisierung von Koronarplaques etabliert. Zur Beurteilung von Plaques untersucht ein Radiologe – mit Hilfe von Software Tools – die aufgenommenen Daten nach charakteristischen Anomalien. Die Entscheidung für ein Plaque basiert dabei hauptsächlich auf Erfahrungswerten. Zur genauen Beschreibung von Plaques existieren anschließend verschiedene Messgrößen. Die manuelle Plaque Beurteilung erzeugt jedoch Fehler, da keine klaren Entscheidungskriterien gegeben sind, so dass Resultate verschiedener Radiologen varieren können. Ferner schwanken auch die Messungen, da CT Intensitäten zwischen verschiedenen Untersuchungen variieren.

Ziel dieser Dissertation ist es daher die genannten Variabilitäten zu reduzieren indem neue (semi-)automatische Algorithmen und Tools vorgestellt werden, welche die Beurteilung von Atherosklerosen in Koronararterien verbessern. Die vorliegende Arbeit erweitert dabei den aktuellen Forschungsstand mit vier wesentlichen Beiträgen.

Zuerst wird eine Methode zur robusten volumetrischen Beurteilung von kalzifizierten Plaques in unkontrastierten CT Aufnahmen beschrieben, welche sowohl die Variabilitäten als auch die Abhängigkeit von der Parametrisierung der bisherigen Methode beseitigt.

Der zweite Beitrag besteht in der Entwicklung eines Frameworks zur automatischen Erkennung von kalzifizierten Koronarplaques. Dazu werden neue (semi-)automatische Algorithmen zur Lokalisation und Extraktion von verschiedenen Anatomien vorgestellt.

Der dritte Beitrag widmet sich der Erkennung von nicht kalzifizierten Plaques. Dazu werden Dual Energy CT Aufnahmen verwendet, um den Kontrast zwischen verschiedenen Geweben im Vergleich zur konventionellen Aufnahme zu verbessern.

Der letzte Beitrag besteht in der Erforschung von räumlichen Plaqueverteilungsmustern mit Frequent Itemset Mining. Mit Hilfe der gewonnenen Verteilungsmuster wird eine gezielte Überprüfung von Koronarsegmenten entwickelt, um die manuelle Plaquedetektion zu verbessern.

Acknowledgements

This work was supported by the National Center of Competence in Research Co-Me of the Swiss National Science Foundation (http://co-me.ch).

This thesis would have not been possible without the support from many sides. First and foremost I thank my advisor Prof. Dr. Gábor Székely for providing me a great research environment. Special thanks goes to Prof. Dr.-Ing. Horst Hahn, PD MD Hatem Alkadhi, and Prof. Dr. Philippe Cattin for the co-examination of this thesis.

I am very grateful to Prof. Dr. Philippe Cattin for taking the time for regular meetings, discussions and scientific support despite his tight schedule.

The clinical trials and evaluations of the developed algorithms would have not been possible without the excellent support through PD MD Hatem Alkadhi from the Institute of Diagnostic Radiology at the University Hospital Zurich. Furthermore, I would like to thank MD Stephan Baumüller, MD Lotus Desbiolles, PD MD Sebastian Leschka, and MD Paul Stolzmann for their medical contributions.

I also thank Thomas Fuchs for his statistical advice and Joseph Knight, Caroline Kühnel, and Philipp Fürnstahl for proofreading.

For the numerous discussions and a great time, I am grateful to my colleagues at the Computer Vision Laboratory of ETH Zurich as well as to my project colleagues from the Laboratory of Thermodynamics in Emerging Technologies of ETH Zurich. Particular thanks goes to Andreas Ess, Philipp Fürnstahl, Axel Krauth, Jan Lesniak, Till Quack, Daniel Roth, Martin von Siebenthal, and Thibaut Weise.

Special thanks goes to my family, especially to my mum and my dad, for their enduring support.

Contents

List of Figures xiii

List of Tables xv

1 Introduction 1
1.1 Cardiac Anatomy and Physiology . . . 1
1.1.1 Heart . . . 2
1.1.2 Coronary Arteries . . . 3
1.1.3 Coronary Tree . . . 4
1.2 Atherosclerosis . . . 5
1.2.1 Development . . . 5
1.2.2 Classification . . . 6
1.2.3 Treatment . . . 9
1.3 Imaging Modalities . . . 11
1.3.1 Coronary Angiography . . . 12
1.3.2 Intravascular Ultrasound . . . 12
1.3.3 Magnetic Resonance Imaging . . . 13
1.3.4 Computed Tomography . . . 14
1.4 Contribution of this Thesis . . . 20
1.5 Organization of this Thesis . . . 23

2 Calcium Scoring 25
2.1 Scores . . . 25
2.1.1 Agatston Score . . . 26
2.1.2 Volume Score . . . 26
2.1.3 Mass Score . . . 27
2.1.4 Other Scores . . . 27
2.2 Factors Influencing the Calcium Scores . . . 27
2.2.1 Reconstruction Kernel . . . 28
2.2.2 Tissue Density . . . 29
2.2.3 Tube Voltage . . . 29
2.2.4 Spatial Resolution . . . 29

2.3 ACCURATUM . . . 29
2.4 Experimental Setup . . . 31
2.4.1 Phantom . . . 31
2.4.2 CT Parameters . . . 32
2.4.3 Training Data Sets . . . 34
2.4.4 Evaluation Data Sets . . . 34
2.4.5 Statistical Analysis . . . 34
2.5 Results . . . 35
2.5.1 Training Data Sets . . . 35
2.5.2 Evaluation Data Sets . . . 35
2.6 Discussion and Conclusion . . . 38

3 Extraction of Anatomical Structures 41
3.1 Ascending Aorta Detection . . . 41
3.1.1 Related Work . . . 42
3.1.2 Methods . . . 43
3.1.3 Experimental Setup and Results . . . 46
3.2 Coronary Artery Tracking . . . 47
3.2.1 Related Work . . . 48
3.2.2 Methods . . . 50
3.2.3 Experimental Setup and Results . . . 54
3.3 Vessel Lumen Segmentation . . . 54
3.3.1 Related Work . . . 55
3.3.2 Methods . . . 56
3.3.3 Experimental Setup and Results . . . 61
3.4 Coronary Artery Tree Labeling . . . 61
3.4.1 Related Work . . . 62
3.4.2 Methods . . . 63
3.4.3 Experimental Setup and Results . . . 67
3.5 Discussion and Conclusion . . . 68

4 Automatic Detection of Calcified Coronary Plaques 71
4.1 Introduction . . . 71
4.1.1 Related Work . . . 72
4.2 Methods . . . 73
4.3 Experimental Setup and Results . . . 77
4.4 Discussion and Conclusion . . . 79

5 Assessment of Lipid Plaque Constituents 83
5.1 Introduction . . . 83
5.1.1 Related Work . . . 85
5.2 Methods . . . 88

5.2.1 Basis Material Decomposition . . . 88
5.2.2 Basis Material Attenuation Coefficients . . . 89
5.2.3 Cancelation Step . . . 92
5.3 Experimental Setup and Results . . . 93
5.4 Discussion and Conclusion . . . 97

6 Spatial Distribution Patterns of Atherosclerosis 101
6.1 Introduction . . . 101
6.1.1 Related Work . . . 102
6.2 Methods . . . 103
6.2.1 Itemset . . . 104
6.2.2 Association Rules . . . 105
6.2.3 Guided Review . . . 108
6.3 Experimental Setup and Results . . . 109
6.3.1 Data Acquisition . . . 110
6.3.2 Spatial Plaque Distribution Patterns . . . 111
6.3.3 Validation of Guided Review . . . 114
6.3.4 Clinical Application of Guided Review . . . 121
6.4 Discussion and Conclusion . . . 122

7 Summary and Outlook 125

Bibliography 129

List of Figures

1.1 The blood vessel with its three layers. 2
1.2 The human heart with its four chambers. 3
1.3 The coronary artery tree with its four main arteries. 4
1.4 The 16-segment model of the coronary artery tree. 5
1.5 CT and histopathological examples for atherosclerotic lesions. . . 7
1.6 Different stages of plaque development. 10
1.7 Treatment options for cardiovascular diseases. 11
1.8 Coronary angiography for the assessment of stenoses. 13
1.9 IVUS for the assessment of atherosclerosis. 14
1.10 MRI image of the heart. 15
1.11 CT system. 16
1.12 Construction of a classical CT device. 17
1.13 Typical HU range for selected tissues. 18
1.14 Appearance of plaques in CT images. 21

2.1 Principle of ACCURATUM algorithm. 30
2.2 Intensity profile of a node along its surface normal. 31
2.3 Antropomorphic phantom with three sets of calcified cylinders. . . 33
2.4 Results of ACCURATUM by varying tube voltage and reconstruction kernel. 36
2.5 Results of ACCURATUM by varying slice thickness. 37

3.1 Propagation of search rays through volume of interest. 43
3.2 Detection of candidate points. 45
3.3 Clustering of candidate points. 45
3.4 Challenging anomalies for tracking algorithms. 47
3.5 Cost functions for the coronary artery tracking algorithm. 52
3.6 Manual bridging of stenoses. 53
3.7 Data structure to store branching information. 54
3.8 Exemplary results of coronary artery tracking. 55
3.9 Pruning of the segmentation result. 61
3.10 Exemplary results of the coronary artery segmentation algorithm. . 62

3.11 Characteristic landmarks for the labeling of the right coronary artery branch. 66

4.1 Workflow of the plaque detection framework. 74
4.2 Registration of plaque candidates. 78
4.3 Distribution of plaques and false positives. 79
4.4 Exemplary results after the various steps of the plaque detection framework. 80

5.1 Workflow of the tissue cancelation algorithm. 88
5.2 Photon energy distribution of a Tungsten X-ray tube. 91
5.3 Basis plane spanned by two selected basis materials. 92
5.4 Contrast enhancement factor and signal to noise ratio in dependence on the cancelation angle. 94
5.5 Contrast enhancement among different tissue types. 96
5.6 Comparison of contrast enhancement. 97
5.7 Comparison of signal to noise ratio. 98

6.1 Itemset tree with its different hierarchical levels (level 1-4). 106
6.2 Itemset tree (level 5-6). 107
6.3 Prototype of guided review as a web application. 109
6.4 Spatial plaque distribution patterns in a schematic representation of the coronary artery tree. 113
6.5 Impact of the minimum confidence parameter. 117
6.6 Impact of the minimum support parameter. 118
6.7 Performance comparison between guided review by frequent itemset mining and guided review by random selection. 119
6.8 Number of segments proposed by frequent itemset mining for guided review. 120
6.9 Improvement with iterative guided review by frequent itemset mining. 120
6.10 Detected plaques by guided review by frequent itemset mining and the reference approach shown in a schematic representation of the coronary artery tree. 122

List of Tables

1.1 Definition of the 16 coronary segments according to the model of the American Heart Association. 6
1.2 Typical parameters for a cardiac CT protocol. 19
1.3 Reported HU values for lipid, fibrous, and calcified tissue. 22

2.1 Characteristics of the nine plaque equivalent cylinders. 33

3.1 Selected parameters for ascending aorta detection. 46

4.1 Results of the plaque detection framework. 81

5.1 Chemical composition of selected body tissues. 90
5.2 Optimal cancelation angle with maximum contrast enhancement between tissues. 94
5.3 Results of the contrast enhancement with one fixed cancelation angle. 95

6.1 Patient demographics and clinical characteristics. 110
6.2 Plaque distribution in the study population. 112
6.3 Association rules showing evidence for plaques at different hierarchical levels. 115
6.4 Association rules showing evidence for mixed plaques. 115

1

Introduction

Cardiovascular diseases represent the leading cause of death in developed western countries [Jougla 2003, Lloyd-Jones *et al.* 2009, Rosamond *et al.* 2008]. In the presence of atherosclerosis, plaques develop by the accumulation of lipid or calcified deposits in the vessel walls (see Section 1.2). Coronary plaques may rupture and lead to acute coronary syndromes [Shinohara *et al.* 2008]. Therefore, early detection and quantification of coronary plaques is of high interest.

This introductory chapter addresses cardiovascular diseases and focuses on the development, classification, and treatment of atherosclerosis. For this purpose, basic anatomical and physiological aspects of the cardiovascular system are briefly reviewed. Additionally, an overview of imaging modalities used for the assessment of atherosclerosis is given. In conclusion of this chapter, the organization of the thesis is outlined.

1.1 Cardiac Anatomy and Physiology

The vascular system, also called the circulatory system, has the task of moving nutrients and gases to all cells in the body and of removing waste (e.g. carbon dioxide) from the cells. The vascular system can be divided into the lymphatic system, which distributes lymph, and the cardiovascular system, which distributes blood through vessels. Two different types of vessels are present in the cardiovascular system: *arteries* transport blood away from the heart, whereas *veins* transport blood to the heart. All arteries, with the exception of the pulmonary and umbilical artery, carry oxygenated blood.

The blood vessel wall consists of three layers (Fig. 1.1). The *tunica externa* or *tunica adventitia* is the outermost layer, which embeds the vessel in its surroundings. It is composed of areolar or fibrous connective tissue. *Tunica media* is the middle layer of a blood vessel. It is made up of smooth muscle cells and elastic tissue and can be distinguished from the inner layer by its color and by the transverse arrangement of its fibers. The *tunica intima* is the innermost layer and is defined as the region of the arterial wall from, and

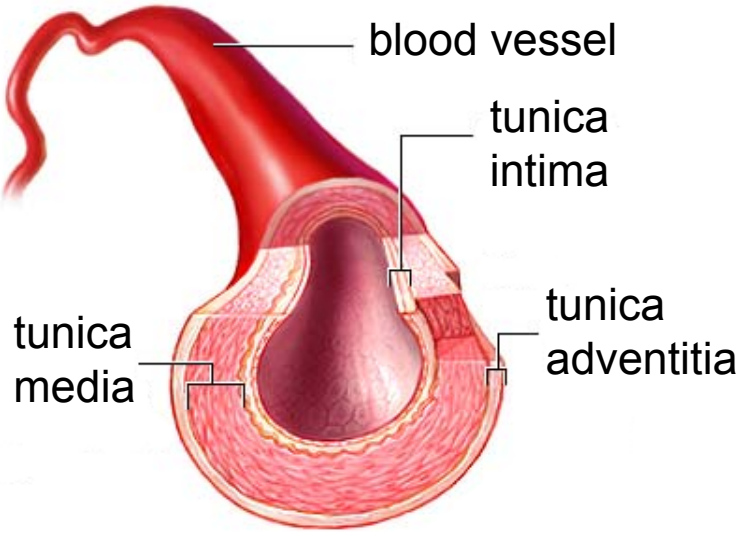

***Figure 1.1**: The blood vessel wall consists of three layers: tunica adventitia, tunica media, and tunica intima. Figure in courtesy of the National Institutes of Health (NIH).*

including, the endothelial surface at the lumen to the luminal margin of the media [Faller and Schünke 2004]. The interior of the vessel enclosed by the wall is the *lumen* of the vessel.

Arteries and veins resemble each other in their three layer composition as aforementioned. However, in contrast to veins, arteries have an elastic, fenestrated membrane between the inner and middle layer. Furthermore, the arterial muscular layer is better developed and contains a varying amount of elastic fiber. This muscular layer is the driving force of the blood vessels as it regulates the blood flow and blood pressure by dilating and constricting the diameter of the blood vessel [Faller and Schünke 2004].

1.1.1 Heart

The human heart is a hollow muscular organ of a somewhat conical form. It is subdivided by the interventricular septum into a right part for the pulmonary circulation and a left part for the systemic circulation throughout the entire body. Furthermore, a constriction divides each half into two cavities, the upper one being the atrium and the lower one the ventricle. All in all, the heart consists of four chambers: the right atrium, the right ventricle, the left atrium and the left ventricle (Fig. 1.2).

The heart functions as the driving engine of the cardiovascular system. The deoxygenated blood from the human body returns through the great venous trunk to the right atrium and then to the right ventricle from where it is pumped through the pulmonary artery to the lung. In the lung the blood is enriched with oxygen and flows back through the

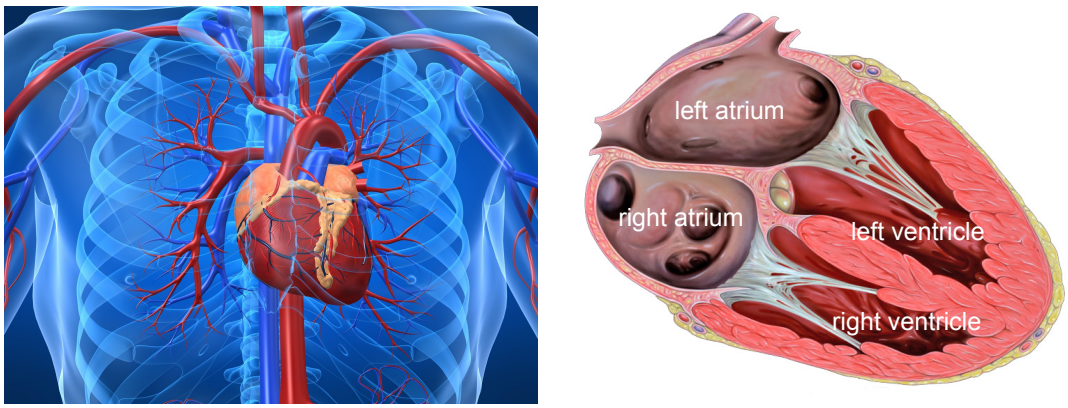

(a) The human heart. *(b)* Heart chambers.

***Figure 1.2**: The human heart (a) with its four chambers (b). Right figure in courtesy of Patrick J. Lynch and C. Carl Jaffe.*

pulmonary veins into the left atrium of the heart. From there, it reaches the left ventricle, which pumps the blood through the aortic valve and the ascending aorta back into the systemic circulation.

1.1.2 Coronary Arteries

The heart as a muscular organ also needs the supply of blood for its metabolism. This is accomplished by the coronary arteries that exclusively supply the heart muscle (*myocardium*) with blood. The coronary arteries arise directly from the ascending aorta, immediately above the aortic valve. In the anatomy of the general population, the ascending aorta contains two outlets for two different branches of coronary arteries. The right branch, named the right coronary artery (RCA), arises from the ascending aorta and runs in the coronary sulcus, at first under the right auricle, then around the right cardiac border toward the diaphragmatic surface and finally to the apex of the heart. The left main artery (LM) arises from the second outlet and divides after a short course into the circumflex artery (CX) and the left anterior descending artery (LAD). The former runs posteriorly whereas the latter runs over the anterior surface. LM, LAD, and CX form the left branch of the coronary arteries. Altogether, the left and right branch build up the coronary artery tree (Fig. 1.3).

Depending on the artery that supplies the posterior descending artery (PDA) and the posterolateral artery (PLA), three different types of coronary artery dominance patterns are differentiated. In a *right-dominant* pattern, the RCA supplies both PDA and PLA whereas in a *left-dominant* pattern, the CX supplies both arteries. A *balanced* pattern is present when the PDA is supplied by the RCA and the CX supplies the PLA. In the general pop-

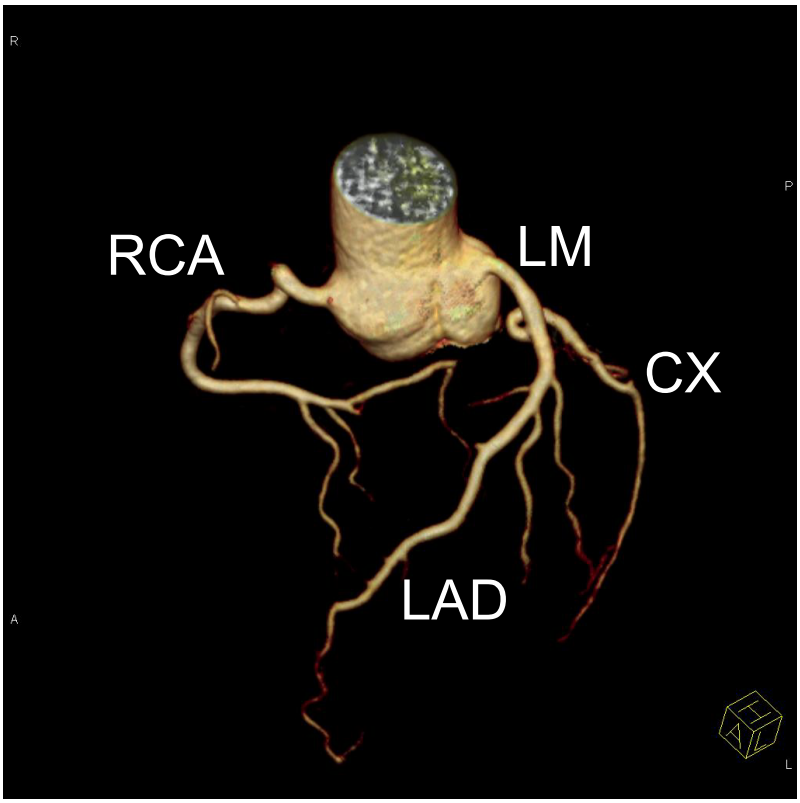

***Figure 1.3**: The coronary artery tree with its four main arteries, the right coronary artery (RCA), the left main artery (LM), the left anterior descending (LAD) and the circumflex artery (CX), respectively.*

ulation, most people have a right-dominant pattern (86.6%), followed by those having a left-dominant (9.2%) and finally a balanced pattern (4.2%) [Cademartiri *et al.* 2008].

1.1.3 Coronary Tree

The division of the coronary artery tree into its four main arteries is not sufficient to allow a detailed reporting of coronary diseases. Therefore, the American Heart Association (AHA) [Austen *et al.* 1975] suggested to divide the coronary artery tree into 16 segments that are defined by anatomical landmarks (Fig. 1.4). Although further divisions of the coronary artery tree into segments were proposed [Alderman and Stadius 1992, Principal Investigators of CASS and their associates 1981], the 16-segment AHA model is well established and widely used in clinical routine such that it will also be applied throughout this thesis for referencing to certain positions within the coronary artery tree. Table 1.1 highlights the 16 segments, and their location within the four main coronary arteries, as well as the anatomical landmarks that define their beginning and ending. For

details about certain specifics, the reader is kindly referred to the original AHA recommendation [Austen *et al.* 1975].

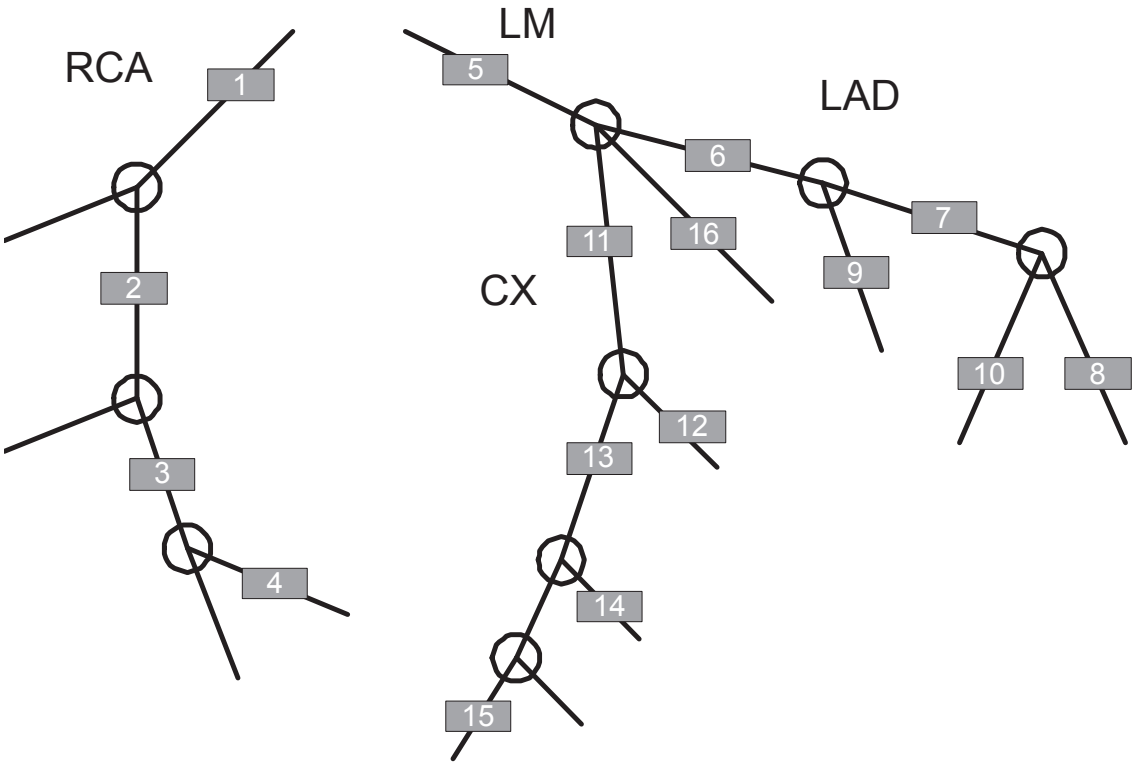

***Figure 1.4**: The 16-segment model of the coronary artery tree.*

1.2 Atherosclerosis

Atherosclerosis (from the greek *athere* – porridge, gruel and *sklerosis* – hardening) is the progressive narrowing and hardening of the arteries over time. It is a natural process, starting already in infancy. However, several risk factors (e.g. diabetes, obesity, high blood pressure, smoking) accelerate the progression of atherosclerosis.

1.2.1 Development

When atherosclerosis develops, different materials like fatty deposits or minerals accumulate in the artery's internal wall. Such an accumulation is referred to as a *plaque* or more generally as a *lesion* within the coronary artery. Both terms will be equivalently used in the course of this thesis.

***Table 1.1**: For reporting, the American Heart Association proposed a 16-segment model of the coronary artery tree [Austen et al. 1975].*

nr.	vessel	anatomical definition (start - end)
1	RCA	ostium RCA - one-half the distance to acute margin of heart
2	RCA	end segment 1 - acute margin of heart
3	RCA	acute margin of heart - origin of posterior descending branch
4	RCA	equal to posterior descending branch
5	LM	ostium LM - bifurcation of LM into CX and LAD
6	LAD	origin LAD - to and including origin of first major septal perforator branch
7	LAD	end segment 6 - orifice of second diagonal branch
8	LAD	end segment 7 - terminal of LAD
9	LAD	equal to first diagonal branch
10	LAD	equal to second diagonal branch
11	CX	origin CX - to and including origin of obtuse marginal branch
12	CX	equal to obtuse marginal branch
13	CX	end segment 11 - terminal of CX
14	CX	equal to posterolateral branch
15	CX	equal to posterior descending
16	-	equal to ramus intermedius

When atherosclerosis develops, advanced lesions (see Section 1.2.2) form first in regions with adaptive intimal thickening [Stary *et al.* 1992]. Intimal thickenings are physiological adaptations to mechanical stresses secondary to variations in flow, wall tension, or both. The thickening process may be thought of as the consequence of a range of physiological stimuli, constituting an attempt by the tissue to maintain normal conditions of flow and wall tension, respectively. Two types of intimal thickening can be observed: eccentric and diffuse intimal thickening. Eccentric intimal thickening is a relatively abrupt and focally increase in the thickness of the intima associated with branches and orifices. Diffuse intimal thickening is a spread-out and often circumferential pattern of adaptive intimal thickening not clearly related to specific geometric configurations of the arteries.

1.2.2 Classification

Depending on various factors, a lesion might develop into an advanced one that may cause a blockage of arteries. A numerical classification of histologically defined lesion types was established by the AHA Committee on Vascular Lesions in 1994 [Stary *et al.* 1994] and 1995 [Stary *et al.* 1995]. New consolidated findings led to an update of the classification in 2000 [Stary 2000]. In the same year, Virmani *et al.* [2000] suggested some changes for the original classification to overcome certain shortcomings. The eight

stages for the plaque development as defined by the AHA committee [Stary 2000] will subsequently be summarized.

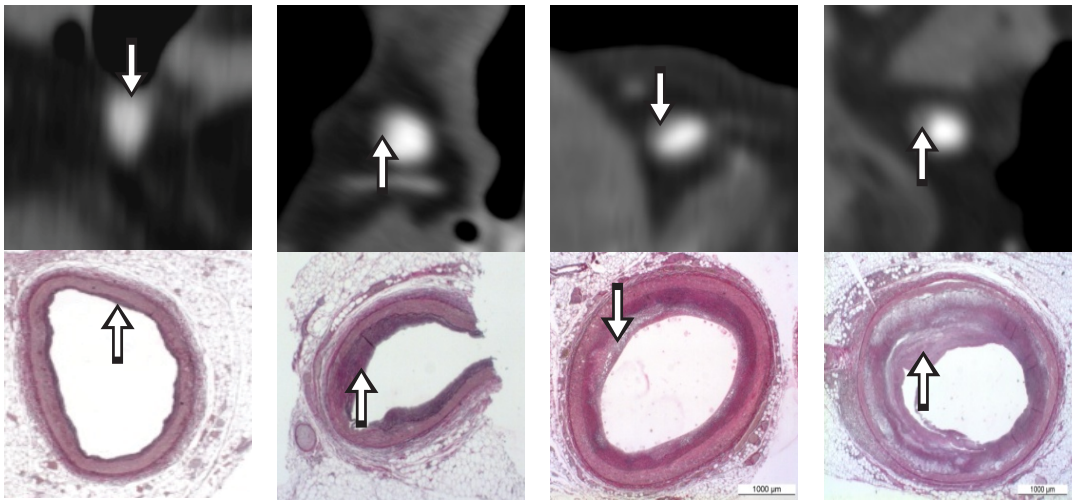

(a) Type I. *(b)* Type II. *(c)* Type III. *(d)* Type IV.

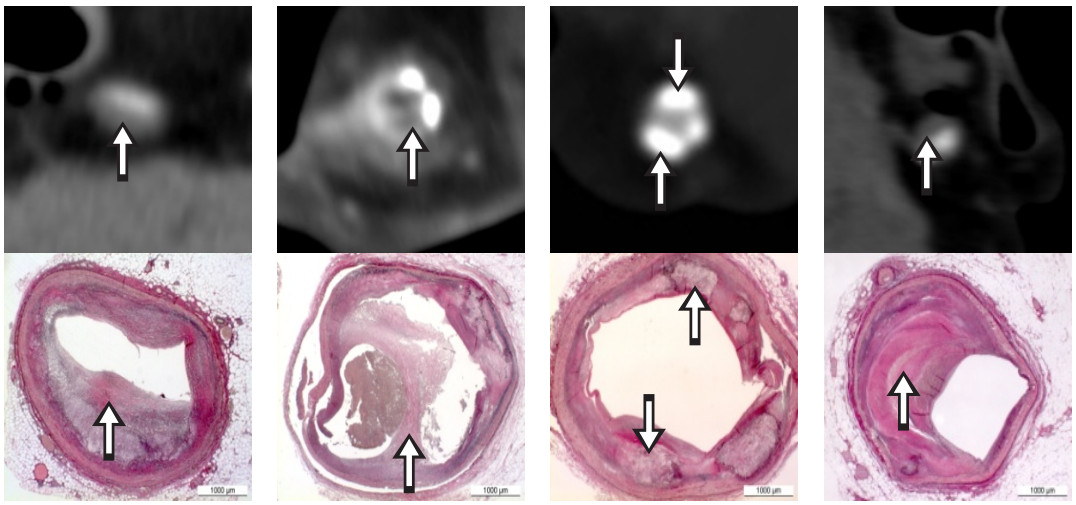

(e) Type V. *(f)* Type VI. *(g)* Type VII. *(h)* Type VIII.

***Figure 1.5**: Computed tomography (top) and histopathological (bottom) examples for atherosclerotic lesions of type I-VIII. Figures in courtesy of Sebastian Leschka, University Hospital Zurich.*

Type I Lesions

Type I lesions consist of the first microscopically and chemically detectable lipid deposits in the intima and the cell reactions associated with such deposits. This type of lesion is

most frequent in infants and children. However, such initial lesions can also be found in adults, particularly in those with little atherosclerosis, or in locations of arteries that are lesion resistant.

Type II Lesions

Type II lesions include fatty streaks, which on gross inspection may be visible as yellow-colored streaks, patches, or spots on the intimal surface of arteries. Fatty streaks begin to develop around the age of 15 years and slowly increase in size and number until about the age of 60. Out of the many type II lesions generally present in a person, only a smaller subgroup – type IIa or progression-prone – will be the first to proceed to type III lesions and then to advanced lesions, if advanced lesions are to develop at all. The larger remaining subgroup of type II lesions – type IIb or progression-resistant – either do not progress, progress slowly, or progress only in persons with very high plasma levels of atherogenic lipoproteins. Whether a type II lesion develops at all, and whether it is progression-prone or progression-resistant, is largely determined by the mechanical forces that act on relevant parts of the vessel wall.

Type III Lesions

Type III lesions form the morphological and chemical bridge between type II lesions and type IV lesions – also called atheromas. The characteristic histological features of type III lesions are microscopically visible extracellular lipid droplets and particles.

Type IV Lesions

In type IV lesions a dense accumulation of extracellular lipid occupies an extensive but well-defined region of the intima. This type of extracellular lipid accumulation is known as the lipid core. A type IV lesion is the first considered *advanced* because of the severe intimal disorganization caused by the lipid core.

Type V Lesions

Type V lesions are defined as lesions, in which prominent new fibrous connective tissue has formed. The new tissue is part of a lesion with a lipid core. A type V lesion may be multilayered: several lipid cores, separated by thick layers of fibrous connective tissue, are stacked irregularly one above the other.

Type VI Lesions

The development of disruptions of the lesion surface, hematoma or hemorrhage, and thrombotic deposits characterizes type VI lesions. While type VI lesions generally have the underlying morphology of type IV or V lesions, surface disruptions, hematoma, and thrombosis may be (although less often) superimposed on any other type of lesion and even on intima without an apparent lesion.

Type VII Lesions

Lesions, in which mineralization is the dominant feature, are summarized as type VII lesions. In previous publications from the AHA committee [Stary *et al.* 1995], this type was also referred to as a type Vb lesion. These lesions generally contain a large amount of calcium (nodules of crystalline hydroxyapatite) and also have an increased fibrous connective tissue.

Type VIII Lesions

In fibrotic – or type VIII (previously known as type Vc) – lesions, the normal intima is replaced and thickened with fibrous connective tissue, while lipid is minimal or even absent. Fibrotic lesions could be the result of one or more processes, including organization of thrombi, extension of the fibrous component of an adjacent fibroatheroma, or regression of lipid cores.

The development of lesions through the several stages (Fig. 1.6) is a natural process. Type I and II lesions already occur in infants and children but may also occur in adults. Type III lesions may evolve soon after puberty and, in their composition, form the bridge between early and advanced lesion. Type IV is the first lesion considered advanced by histological criteria and is frequent from the third decade on. In the AHA classification the term *advanced lesion* is used as an umbrella term for all lesions that disrupt intimal structure, *i.e.* all lesions following type III. Morbidity and mortality from atherosclerosis is largely due to these advanced lesions. After the third decade of life, lesions of type V-VIII start to appear. In middle-aged and older persons, these often become the predominant lesion types. As aforementioned, the development of an early lesion to an advanced lesion depends on many factors and circumstances that are still researched [El Harchaoui *et al.* 2009, Zheng *et al.* 2008] but that are out of the scope of this thesis.

1.2.3 Treatment

Depending on a plaque's morphology and composition and the patient's health state, several treatment options exist for cardiovascular diseases. Medication with a lipid-lowering

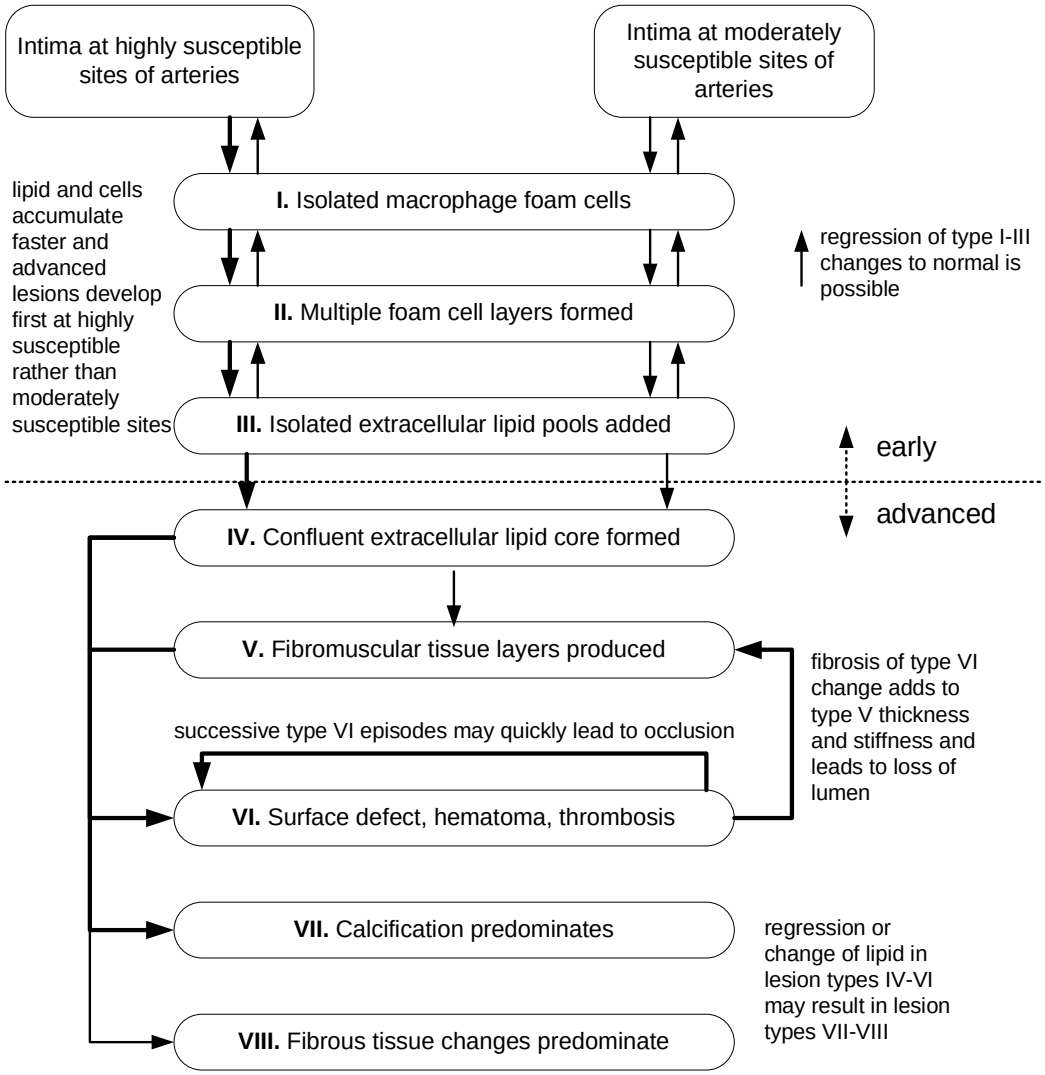

***Figure 1.6**: Stages of plaque development according to scheme proposed by the AHA Committee on Vascular Lesions [Stary 2000]. The diagram lists the main histological characteristics of each sequential step (lesion type). Thick or thin arrows differentiate between the relative ease with which lesions develop at specific sites, or indicate the relative frequency and importance of a pathway section.*

drug might regress a plaque to some extent [Lima *et al.* 2004, Nissen *et al.* 2006]. *Balloon angioplasty* or *coronary angioplasty* (Fig. 1.7(a)) attempts to push the plaque back against the artery wall. In this intervention, a balloon is inserted in a catheter-based procedure and inflated at the plaque's position. In case the artery's wall is weakened and has to be stabilized, a *drug eluting* or bare *metal stent* is inserted by the same catheter-based procedure (Fig. 1.7(b)). The stent – a short, metal mesh tube – keeps the vessel open and the coating with drugs prevents a re-narrowing of the artery (*restenosis*). In a *coronary artery bypass graft* (CABG) surgery, arteries or veins are grafted to the coronary arteries to bypass atherosclerotic narrowings or blockages.

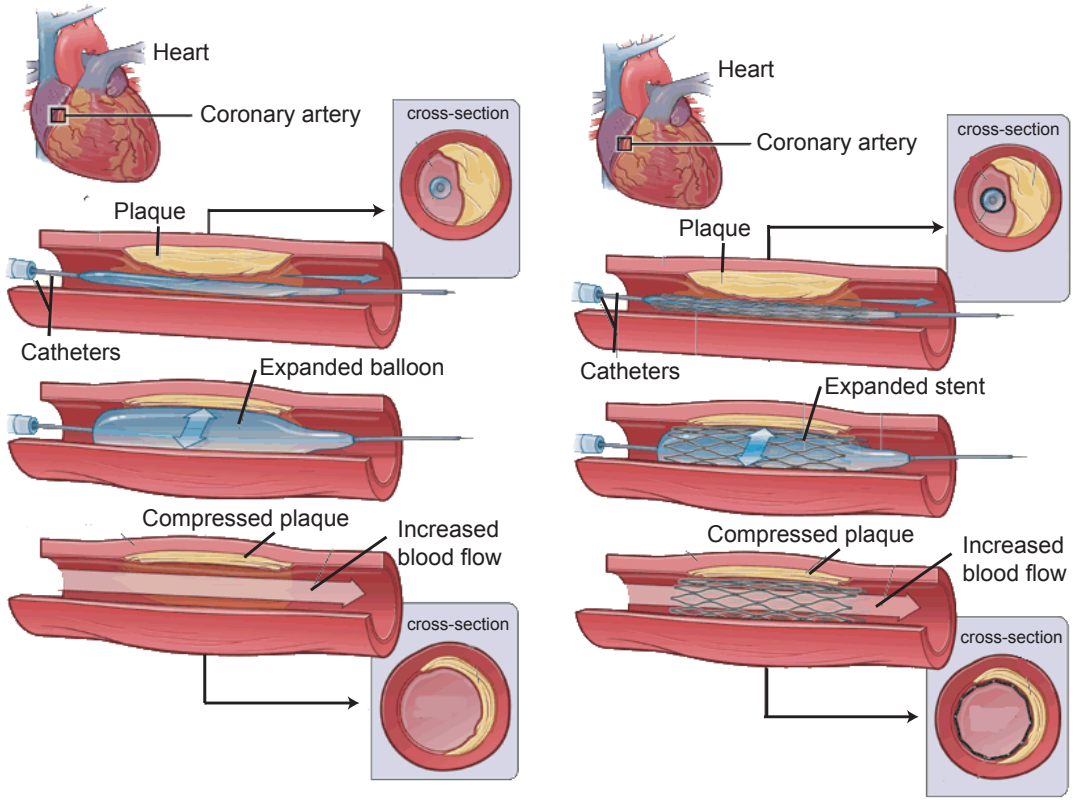

(a) Balloon angioplasty. *(b)* Stent.

Figure 1.7*: Two possible treatment options for cardiovascular diseases. Figures by courtesy of the National Heart, Lung, and Blood Institute as part of the National Institutes of Health and the U.S. Department of Health and Human Services.*

1.3 Imaging Modalities

Cardiac diseases can be diagnosed in several ways. First of all, there are indirect methods like exercise electrocardiography testing, stress echocardiography, and myocardial perfu-

sion imaging (e.g. with single-photon emission computed tomography (SPECT)). Those tests can only predict the presence or absence of cardiovascular diseases in general, but cannot provide details about the presence of atherosclerosis.

To allow a visual localization of the affected coronary artery and the investigation of the remaining lumen, various direct imaging techniques have been established, of which the most common ones will be introduced in this section. Some of the imaging techniques like coronary angiography (Section 1.3.1) and intravascular ultrasound (Section 1.3.2) are *invasive*, *i.e.* an instrument has to be inserted into the human body for image acquisition. Other modalities like magnetic resonance imaging (Section 1.3.3) or computed tomography (Section 1.3.4) are *non-invasive*.

1.3.1 Coronary Angiography

Selective coronary angiography (CA) is considered to be the gold standard for assessing coronary artery lumen (Fig. 1.8). For image acquisition, a catheter is inserted into the arterial system through a peripheral artery, moved along to the aorta, and finally placed into the origins of the coronary arteries. Contrast agent is then administered through the catheter into the coronary arteries and its distribution is imaged from several angles (e.g. bi-plane angio) with a planar X-ray technique in order to identify possible narrowings of the vessel lumen [Ohnsorge *et al.* 2007].

Coronary angiography has both a good spatial and temporal resolution. An earlier drawback of CA, namely the pure two-dimensional (2D) representation of coronary arteries, which was a problem in case of overlapping vessels, could be solved: Through the simultaneous acquisitions of two images with the bi-plane technique and with fast image processing algorithms, a three-dimensional (3D) model of the coronary arteries can be provided with modern systems. However, CA only allows for the detection of stenoses and is therefore not suitable for the evaluation of vessel wall and coronary plaques. Additionally, the invasive character of CA also involves risks [Fauci *et al.* 2008].

1.3.2 Intravascular Ultrasound

Intravascular ultrasound (IVUS), also an invasive imaging modality, measures the sound echo of the human tissue and displays this information as a gray-scale image (Fig. 1.9). For this, a miniaturized ultrasound probe is attached to the distal end of a catheter that is navigated – using CA techniques – into the coronary arteries. After being placed as distally as possible, the ultrasound probe is pulled back with constant speed whereby it rotates around its own axis and acquires the images. Like CA, IVUS also has a good temporal and spatial resolution. With IVUS, the evaluation of the vessel wall and atherosclerotic plaques becomes feasible. IVUS is able to characterize and classify coronary artery

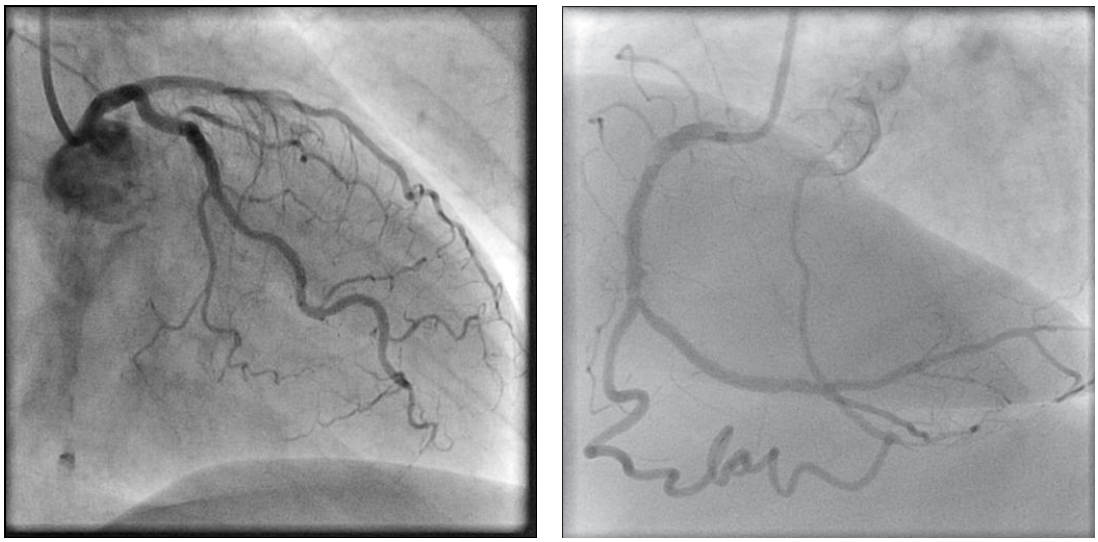

(a) Left coronary tree. *(b)* Right coronary tree.

***Figure 1.8**: Assessment of stenoses with coronary angiography.*

plaques with high accuracy comparable to histopathology [Hiro *et al.* 1997, Palmer *et al.* 1999]. However, IVUS is not able to analyze a vessel distally to a stenosis or in more distal coronary segments due to the diameter of the device [Costa *et al.* 2007, Nissen 2004]. Further, an acoustic shadow might occur behind heavily calcified plaques such that the real extent of those plaques cannot be determined.

1.3.3 Magnetic Resonance Imaging

Magnetic resonance imaging (MRI) is a non-invasive 3D imaging technique to obtain a view of the human body by measuring the oscillating energy of nuclei. It is based on the physical principle that hydrogen nuclei align themselves when exposed to an electromagnetic field and release some characteristic energy when the exposure is stopped. A MRI scanner therefore first aligns the nuclei with a static magnetic field. Afterwards, a second electromagnetic field oscillates at certain pulse rates (RF pulse) to excite a fraction of the nuclei out of alignment with the main field. When the secondary field is turned off, those nuclei precess back to align again with the main field. During this process, they emit their characteristic signal which is received and converted into an image by the MRI system. Tissue that contains a large amount of hydrogen, which occurs abundantly in the human body in the form of water, produces a bright image whereas tissue containing little or no water appears black. In comparison to the subsequently discussed computed tomography technique, MRI shows a good contrast to differentiate soft tissues and it does not expose a patient to any radiation during the examination. However, the spatial resolution is still not acceptable for the assessment of atherosclerosis in coronary arteries.

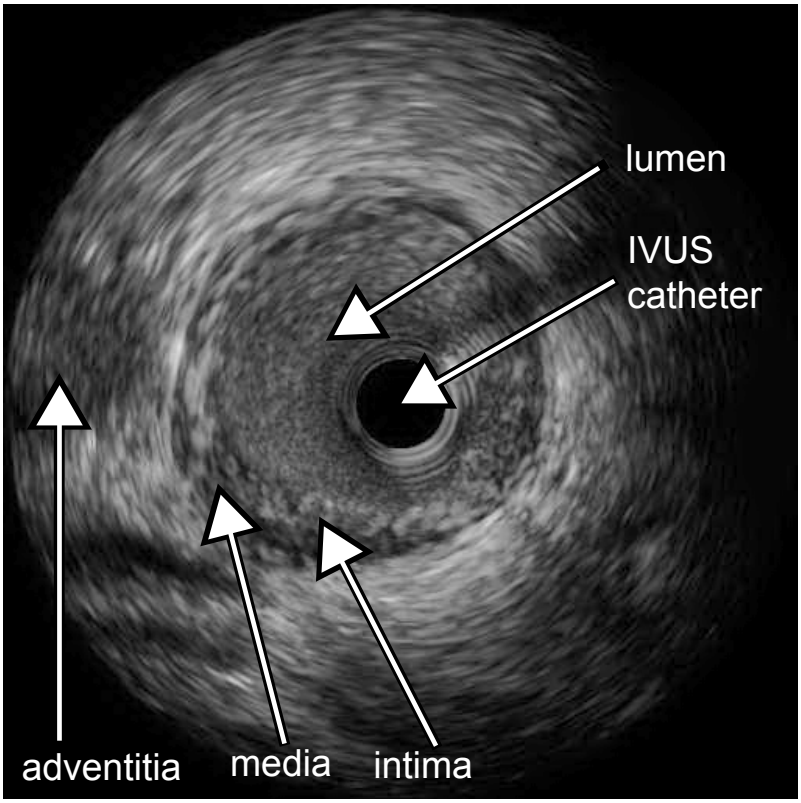

***Figure 1.9**: IVUS acquisition within a coronary artery. The vessel wall and its composition can be clearly determined. Figure in courtesy of Rolf Vogel, Inselspital Bern.*

1.3.4 Computed Tomography

Computed tomography (CT) is a further development of the traditional X-ray technique and allows the acquisition of volumetric 3D image data. In general, a CT data set consists of multiple slices with cross-sectional images of the human body. In contrast to MRI, modern CT systems offer both a good spatial and temporal resolution such that this technique is widely used for the non-invasive diagnosis of coronary heart diseases, although it does come along with a radiation exposure to the patient.

Since its introduction in the early 1970s, computed tomography (CT) has undergone tremendous improvements in terms of performance, technology, and clinical applications. The first systems allowed only the sequential acquisition of cross-sectional images *i.e.* the patient was only moved between slice acquisitions. In todays spiral CT systems, the patient is continuously moved through the CT system while slices are acquired.

In this thesis, CT data sets are the primary imaging modality for the quantitative assessment of atherosclerosis. Therefore, several aspects like the general CT system design, the image acquisition process, the Hounsfield units, and the examination parameters are

***Figure 1.10**: MRI image of the heart. Due to an insufficient spatial resolution, an assessment of coronary arteries is not feasible.*

addressed in closer detail in this section. Further, a typical cardiac CT protocol as well as the appearance of atheroscleroses in CT data sets will be discussed.

System design

For a CT examination the patient is lying on the CT table, which moves the patient during the acquisition process along the longitudinal direction (*i.e.*, along the z-axis) through the gantry (Fig. 1.11(a)). The gantry houses the key components of a CT system, namely X-ray tube, detectors, collimators, and some control units (Fig. 1.11(b)).

A voltage generator produces the power for the X-ray tube generating a cone-beam X-ray distribution that is detected by detectors that are positioned face-to-face to the X-ray tube.

Modern CT systems use an array of solid-state detectors in general to allow the simultaneous acquisition of multiple slices. Each detector element consists of a radiation-sensitive solid-state material, like ceramic, which converts the absorbed X-rays into visible light [Reiser *et al.* 2009]. The light is then detected by a photodiode and converted into an electrical current which is amplified and digitized.

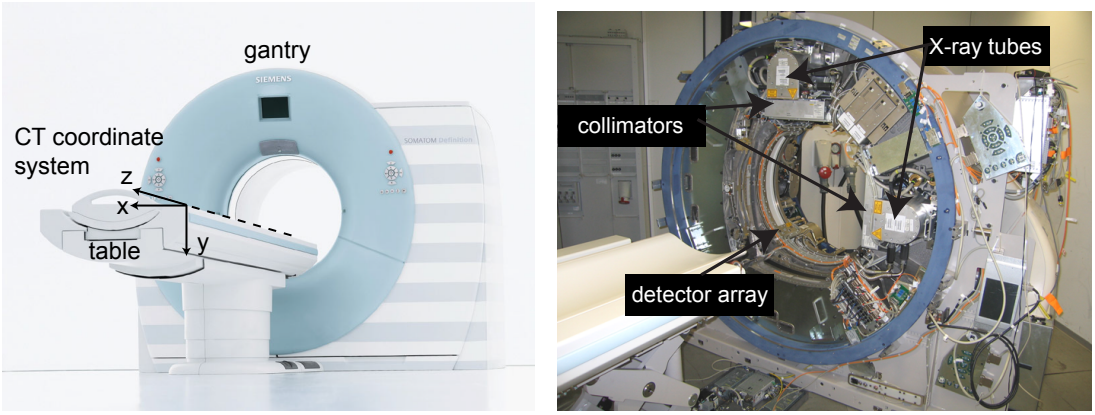

(a) CT system. *(b)* Open gantry.

***Figure 1.11**: Siemens Definition CT system with its various components. Figures in courtesy of Thomas Flohr, Siemens Healthcare.*

Collimators are placed in front of both the X-ray tube and the detectors to shape the radiation beam. The source collimator in front of the X-ray tube reduces the radiation beam to form the maximum required fan beam. The detector collimator – or anti-scatter-grid – in front of the detectors, is primarily used to shield the detector against scattered radiation, thus preventing image artifacts. The size of the detector collimation is a lower boundary for the slice thickness.

Image acquisition

In CT, cross-sectional images of patients are obtained by scanning a transverse slice of the body from different angular positions. Like the traditional X-ray technique, CT measures the attenuation I of a spicular ray with original intensity I_0 after it passed through the human body in a straight line (Eq. 1.1).

$$I = I_0 \cdot e^{-\int \mu(l)\, dl} \tag{1.1}$$

$$\ln \frac{I}{I_0} = \int \mu(l)\, dl \tag{1.2}$$

While pervading the body, the X-ray is attenuated due to the local attenuation coefficient $\mu(x, y)$ of the corresponding tissue. The detector of a CT device can only measure the intensity of the attenuated X-ray beam and not the desired attenuation coefficients $\mu(x, y)$ of the traversed voxels (Fig. 1.12). A transform of the intensity profile (Eq. 1.1) into a so-called attenuation profile (Eq. 1.2) shows that a CT device actually measures the Radon

transform of the function $\mu(x, y)$. An inversion of this Radon transfrom is a computational complex task and can be done using numerical algorithms. Current methods for this reconstruction process like the filtered back projection are discussed by Flohr *et al.* [2005] in more detail.

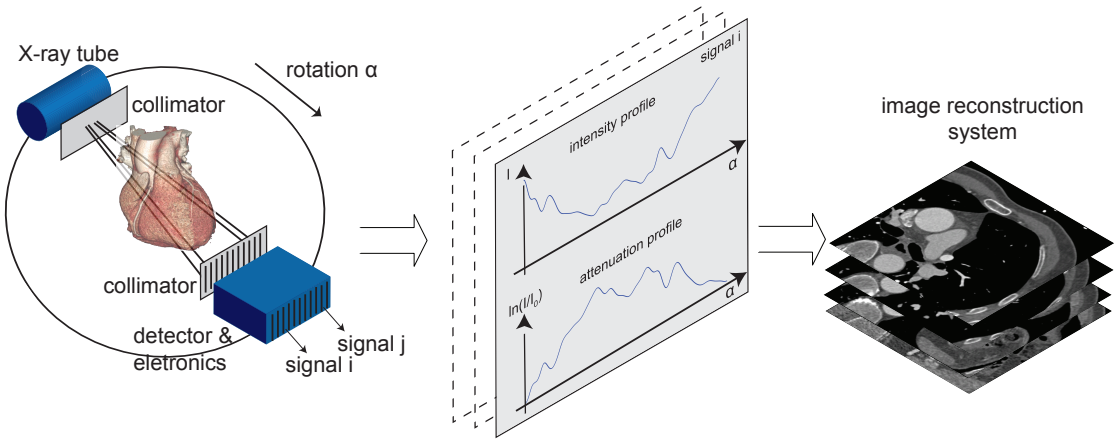

***Figure 1.12**: Construction of a classical CT device. X-ray tube and detector perform a $180°$ rotation while measuring the intensity and attenuation profile. Based on this profile, image reconstruction algorithms are able to determine the attenuation coefficient $\mu(x, y)$ for each voxel.*

Hounsfield units

The measured X-ray attenuation coefficients are normalized to the X-ray attenuation coefficient of water and expressed in Hounsfield units (HU), honoring one of the CT inventors, Sir Godfrey Newbold Hounsfield. Hence, the intensity value I_{HU} for a voxel at position x, y, z is obtained by

$$I_{HU}(x, y, z) = 1000 \cdot \frac{\mu(x, y, z) - \mu_{water}}{\mu_{water}}. \tag{1.3}$$

This normalization makes the comparison of intensity values between different examinations and patients feasible. Further, a characteristic intensity range for certain tissues can be determined (Fig. 1.13). Per definition, water has a HU value of 0. Typical HU values of usual anatomical structures are -1000 HU for air, -100 to -50 HU for fatty tissue, $30 - 70$ HU for blood and muscle tissue, $130 - 500$ HU for calcifications, $200 - 500$ HU for contrast enhanced blood, and $500 - 1500$ HU for bone [Ohnsorge *et al.* 2007].

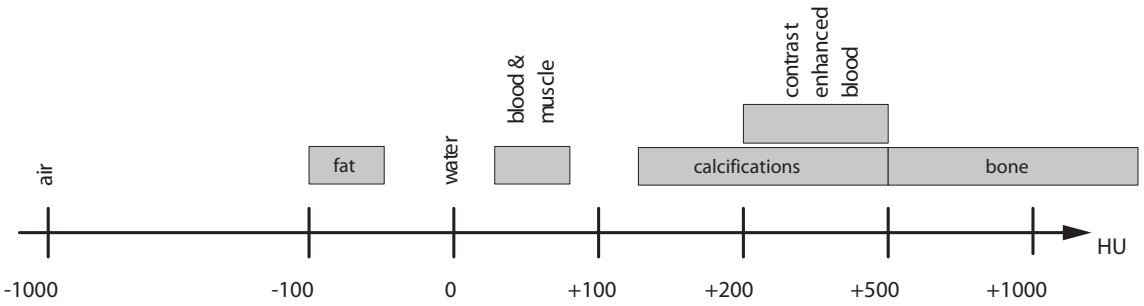

***Figure 1.13**: Typical HU range for selected tissues [Ohnsorge et al. 2007].*

Examination parameters

A CT system has several parameters that can be adjusted to gain the optimal image quality with the lowest possible radiation dose for a specific examination. The most important parameters that are subsequently used throughout this thesis will be briefly introduced. A more detailed discussion of CT examination parameters can be found in [Catalano and Passariello 2005, Ohnsorge *et al.* 2007, Reiser *et al.* 2009].

The *tube potential* or *tube voltage* given in kV determines the spectrum of the X-ray tube and thus the energy distribution of the emitted photons. As the X-ray attenuation coefficient of a tissue depends on the incident energy [Berger and Hubbell 1987], tube potential variations imply a change in the measured intensity values.

The *tube current*, measured in mA, determines the amount of photons emitted by the X-ray tube. The higher the current, the more photons are emitted and received by the detectors such that the amount of noise can be reduced. However, a higher tube current results also in a higher radiation exposure.

The reconstructed cross-sectional image slices are represented by a pixel matrix (usually fixed to 512×512 pixels). Thus, the *field of view* – in general a squared area selected to cover the targeted organ – determines the *in-plane* resolution (in xy-axis direction) of a voxel as the chosen area is mapped to the pixel matrix. The characteristics of a voxel along the CT z-axis are determined by the slice thickness and the reconstruction increment. The *slice thickness* defines the extension (in mm) of a voxel whereas the *reconstruction increment* or *slice spacing* determines the sampling interval along the z-axis direction. A voxel is called *isotropic* when the slice spacing is selected equal to the in-plane resolution.

The *pitch* p is defined as the table feed per rotation of the gantry through the total width of the collimated beam. It shows whether data acquisition occurs with overlap ($p < 1$) or with gaps ($p > 1$).

In CT systems of the latest generation, the pitch is freely selectable and is independent of the slice thickness. As a consequence of the pitch-independent slice thickness, the

image noise for fixed tube currents – measured in milliamperes – would decrease with decreasing pitch due to the increasingly overlapping acquisition. Instead, the tube current is automatically adapted to compensate for dose accumulation and to maintain constant image noise [Catalano and Passariello 2005]. Therefore, the user selects an effective *time tube current product* I_{eff} given in mAs. The tube current I is then automatically adjusted to pitch p and the gantry rotation time T_{rot} according to

$$I = I_{eff}\frac{p}{T_{rot}}. \tag{1.4}$$

Cardiac examination protocol

Typically, two examinations are performed for the assessment of coronary heart diseases. The first one is a *non-enhanced* or *native* examination where the patient is scanned with a low-dose protocol. This examination is used for Calcium scoring – a first risk assessment for cardiovascular diseases (see Chapter 2). Afterwards, CT coronary angiography (CTCA) is performed. For this *contrast-enhanced* or *angio* examination, an iodinated contrast agent is injected through an antecubital vein. Iodine is chosen because it has a high attenuation coefficient and therefore highlights the vessels such that their lumen become clearly visible compared to the non-enhanced examination. Immediately after the contrast agent is injected, *bolus tracking* is performed, *i.e.* a slice showing the ascending aorta is consecutively acquired in constant time-steps. The mean intensity within the ascending aorta is measured and as soon as it reaches a pre-defined threshold, the patient gets the breath-hold command and the examination is performed. Amongst others, contrast-enhanced examinations are used to check thoroughly the coronary artery tree for stenoses, plaques, and other diseases like aneurysms. Table 1.2 compares typical parameter settings for the non-enhanced and contrast-enhanced examination.

***Table 1.2**: Typical CT parameters for a non-enhanced and contrast-enhanced cardiac examination protocol [Alkadhi et al. 2008].*

parameter	non-enhanced	contrast-enhanced
tube voltage [kV]	120	120
time tube current product [mAs]	80	330
pitch	0.2-0.5	0.2-0.5
in-plane resolution [mm]	0.23 - 0.45	0.23 - 0.45
slice thickness [mm]	3.0	0.75
reconstruction increment [mm]	3.0	0.40

Assessment of atherosclerosis

In contrast to the histologically based AHA classification where eight different stages for plaques are differentiated (Section 1.2.2), only lipid, fibrous, and calcified parts can be distinguished in CT images [Schroeder *et al.* 2001, Leber *et al.* 2004]. Three different types of plaques are therefore generally differentiated in CT images, namely *hard* plaques indicating purely calcified plaques, *mixed* plaques indicating a mixture of calcified and noncalcified (*i.e.*, fibrous and lipid) plaques, and *soft* plaques indicating purely noncalcified plaques.

Calcium has a high X-ray attenuation coefficient such that it can be seen as bright spots in CT images. Fibrous and lipid plaques, however, have similar attenuation characteristics compared to the surrounding tissue.

Hence, in non-enhanced examinations, only hard plaques and the calcified parts of mixed plaques can be clearly seen, whereas the noncalcified parts cannot be distinguished from the surrounding tissue or the vessel lumen (Fig 1.14).

To overcome this, a contrast agent is injected in the contrast-enhanced examination to highlight the vessel and therefore to allow a differentiation between noncalcified plaques and the vessel lumen. However, as the contrast agent has a similar HU range than weakly calcified plaques, those may be missed in contrast-enhanced CT images as being no longer distinguishable from the vessel lumen.

In general, there are no clear defined thresholds to differentiate the plaque types as – depending on their density and the selected CT parameters – their appearance may vary. Normally, calcified and noncalcified tissues can be distinguished from each other. However, both tissues may overlap with the intensity range of vessel lumen filled with contrast agent such that a differentiation between noncalcified tissue and lumen as well as between calcified tissue and lumen becomes difficult. Typical ranges for lipid, fibrous, and calcified tissue as reported in several studies for CTCA images are listed in Table 1.3.

1.4 Contribution of this Thesis

These days, the assessment of atherosclerosis is done by manually searching the data set for intensity anomalies. For this, a reader is supported by a software application with different tools, like several views or the automatic delineation of anatomical parts. However, the decision for the presence of plaques itself is based upon the experience of the reader as no clear criteria – like intensity ranges as aforementioned – for the assessment could be defined so far. Once found, several measurements and scores exist for the analysis of plaques.

This manual plaque detection induces errors as due to the absence of clear criteria, the decisions of different readers underlie variabilities. Furthermore, even the intensities in

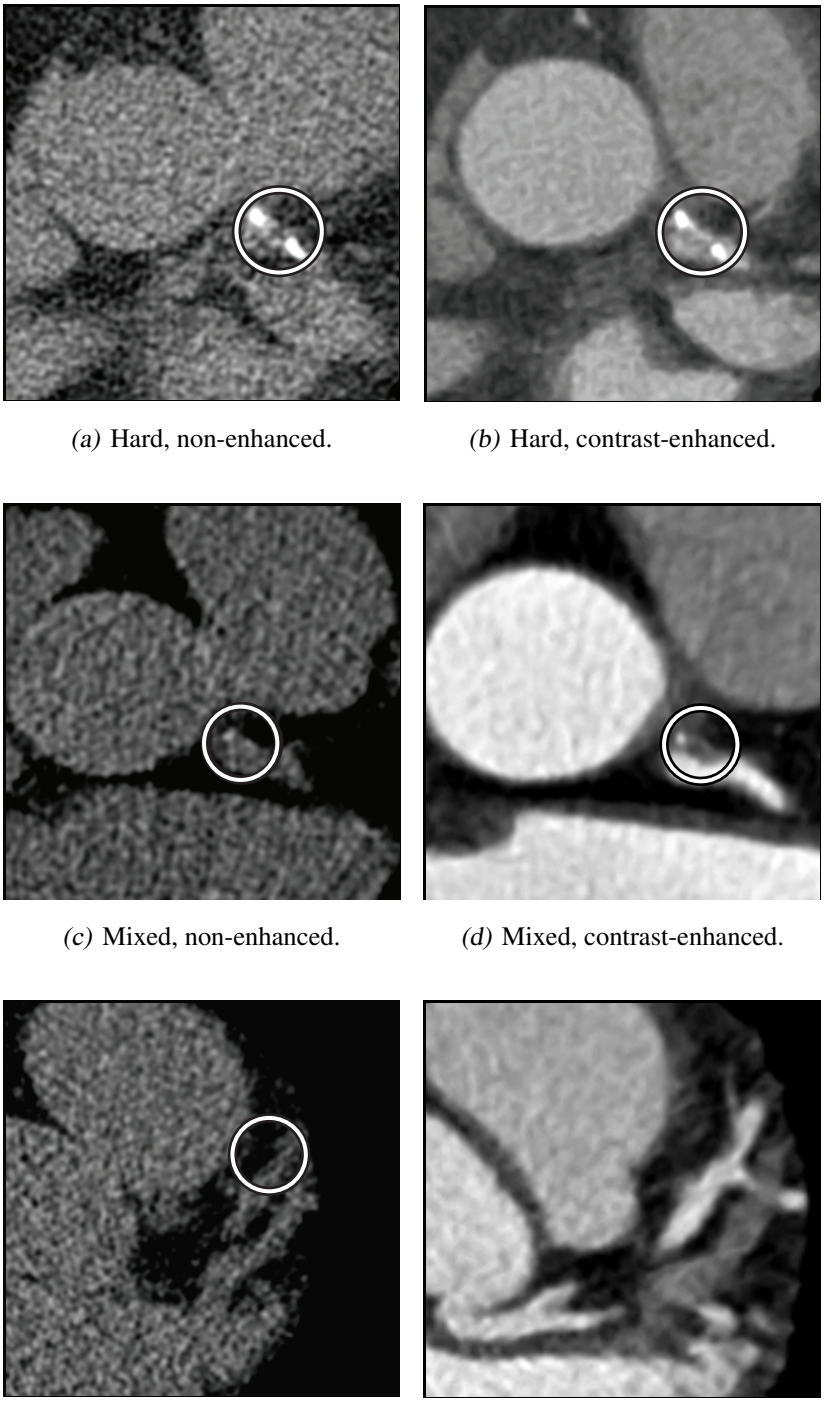

(a) Hard, non-enhanced. *(b)* Hard, contrast-enhanced.

(c) Mixed, non-enhanced. *(d)* Mixed, contrast-enhanced.

(e) Soft, non-enhanced. *(f)* Soft, contrast-enhanced.

***Figure 1.14**: Visibility of plaques (hard, mixed, and soft) in non-enhanced (left column) and contrast-enhanced (right column) CT images. Lipid and fibrous tissue are hardly differentiable from the vessel lumen and the surrounding tissue in non-enhanced examinations. Contrast agent highlights the vessel lumen in contrast-enhanced examinations such that noncalcified plaques can be better detected. However, some calcified plaques might be missed when their intensity is similar to the contrast agent's intensity.*

***Table 1.3**: HU value ranges (mean±std) for lipid, fibrous, and calcified tissue as reported in various CTCA studies.*

study	lipid	fibrous	calcified
Schroeder *et al.* [2001]	-42 to + 47	61 to 112	126 to 736
	(14±26)	(91±21)	(419±194)
Leber *et al.* [2004]	14 to 82	34 to 125	162 to 820
	(49±22)	(91±22)	(391±156)
Brodoefel *et al.* [2008]	-10 to 69	70 to 158	>437
Hein *et al.* [2007]	-100 to 20	20 to 130	350 to 1000
Estes *et al.* [1998]	(39±12)	(90±24)	-
Pohle *et al.* [2007]	-39 to + 167	60 - 201	-
	(58±43)	(121±34)	-
Carrascosa *et al.* [2003]	(76±44)	(149±37)	(449±221)
Motoyama *et al.* [2007a]	-15 to + 33	32 to 130	221 to 1134
	(11±12)	(78±21)	(516±198)
Sun *et al.* [2008b]	7 to 149	22 to 154	295 to 1325
	(79±34)	(90±27)	(772±251)

the CT data sets vary when two data sets are acquired from the same patient. This might also affect plaque analysis.

The aim of this thesis was therefore to reduce these variabilities by presenting automatic and semi-automatic algorithms or tools for an improved assessment of atherosclerosis in coronary arteries. For this, we followed the typical workflow that is routinely performed for an assessment of atherosclerosis in CT data sets. We analyzed existing methods and measurements and proposed new ones where necessary.

Our contribution in this thesis is manifold. First, we will propose a robust procedure for the volumetric assessment of calcified plaques in native data sets. Afterwards, we will introduce new automatic and semi-automatic algorithms for the extraction of anatomical features in CT data sets. These features will then be used to develop a framework for the automatic extraction of calcified coronary plaques. For the assessment of non-calcified plaques, we have researched the potential of Dual Energy CT – the acquisition of CT data at two different energy levels – and we will propose an algorithm that enhances the contrast between tissues as compared to a single energy acquisition. Finally, we have researched for the first time spatial plaque distribution patterns and we will use this knowledge to propose a guided review of coronary segments for an improved detection of coronary plaques in CT data sets.

Part of this work has been published in peer-reviewed journals and proceedings [Saur *et al.* 2009b, Saur *et al.* 2008b, Saur *et al.* 2008a, Saur *et al.* 2009a, Saur *et al.* 2009d, Saur *et al.* 2009c].

1.5 Organization of this Thesis

This thesis is organized as follows:

Chapter 2 gives an overview of existing calcium scores that are used as a first risk assessment for cardiovascular diseases. Subsequently, parameters are discussed that have an impact on those scores. Finally, a robust method for calcium scoring will be proposed and evaluated to overcome the limitations of existing calcium scores.

Chapter 3 introduces specific algorithms for an automatic detection of the ascending aorta, a semi-automatic tracking and subsequent segmentation of the coronary arteries as well as an automatic labeling for the coronary artery tree.

Chapter 4 presents a framework for automatic detection of calcified coronary plaques. The key idea of this framework is to use both the angio and the native examination. For this, plaque candidates are extracted from both examinations and are registered afterwards. Hence, more information is available for each plaque to suppress false positives and to enhance the detection rate.

Chapter 5 discusses current problems for the assessment of lipid plaque constituents in CT data sets in general and furthermore introduces the dual energy technique with potential approaches for the processing of its data. A suitable approach will be selected, described, adapted, and evaluated on clinical dual energy data sets for its feasibility to improve the assessment of lipid plaques by increasing the contrast between tissues.

Chapter 6 presents a framework for the extraction of spatial plaque distribution patterns. Besides an analysis of observed distribution patterns, a guided review process will be defined and intensively evaluated. This guided review will support the manual assessment of atherosclerosis by guiding a reader to segments where no plaques were detected in an initial reading but that show – according to the observed patterns – a high probability of containing initially missed plaques.

Chapter 7 finally summarizes the thesis and points out directions for future research.

2

Calcium Scoring

Calcium scoring measures the amount of coronary calcification through a low-dose, non-enhanced CT acquisition. Calcium scoring is done as a first risk assessment for cardiovascular diseases as the quantity of calcification is a strong predictor for the prognosis of the patient with regard to the development of both non-fatal and fatal cardiovascular events. Despite the good prognostic value for calcium scores, a high variability in the measurement has been reported.

In this work, the aim was to analyze these variabilities of clinically used calcium scores and to develop a calcium score that is more robust against the factors causing the variabilities.

This chapter first provides an overview of existing calcium scores. Subsequently, parameters are discussed that have an influence on those scores. Finally, a robust method for calcium scoring will be proposed and evaluated to overcome the limitations of existing calcium scores.

2.1 Scores

For calcium scoring, a patient is examined with a low-dose, low-resolution, non-enhanced CT protocol. Following this protocol, a tube voltage of $120\ \mathrm{kV}$ with a slice thickness of $3\ \mathrm{mm}$ is used for the acquisition (Section 1.3.4). Afterwards, the amount of calcium is determined by manually selecting calcified spots. In general, calcium scores are then reported separately for the four main vessels of the coronary tree (RCA, LM, LAD, CX). Three different calcium scores are established in clinical routine, namely the *Agatston*, *volume*, and *mass score*, respectively. Other scores have been proposed in the literature for usage in calcium scoring but they have not found their way into clinical praxis.

2.1.1 Agatston Score

Traditionally, the method described by Agatston *et al.* [1990] is used. It selects the maximum calcium density within an area A of at least three adjacent voxels with a density larger than 130 HU for quantification. The fixed attenuation threshold of 130 HU is defined at three standard deviations above the mean soft-tissue attenuation of the heart measured with an electron-beam CT with the assumption that most noncalcified areas would be excluded with this threshold [Hong *et al.* 2003].

The Agatston score

$$S = \sum_i f_i A_i \frac{h}{3} \tag{2.1}$$

accumulates slice-wise the product of plaque area A_i and a factor f_i that depends on the peak-intensity value I_i^{max} within the plaque area at slice i:

$$f_i = \begin{cases} 1: & 130 \text{ HU} \leq I_i^{max} < 200 \text{ HU} \\ 2: & 200 \text{ HU} \leq I_i^{max} < 300 \text{ HU} \\ 3: & 300 \text{ HU} \leq I_i^{max} < 400 \text{ HU} \\ 4: & 400 \text{ HU} \leq I_i^{max} \end{cases} . \tag{2.2}$$

Originally, calcium scoring was done with electron-beam CT (EBCT) and with a fixed slice thickness h of 3 mm. As with modern CT systems, different slice thicknesses are possible, the normalization factor $\frac{h}{3}$ has been introduced to allow an interpretation of the Agatston score based on statistical tables from EBCT studies [Hoff *et al.* 2003].

2.1.2 Volume Score

The *volume score* V introduced by Callister *et al.* [1998] uses the same definition for a plaque area A as the Agatston score and is based on the product of plaque area A_i at slice i and slice thickness h:

$$V = \sum_i A_i h. \tag{2.3}$$

In comparison to the Agatston score, that includes both a volumetric and intensity measure, the *volume score* represents only a single measure.

2.1.3 Mass Score

Another method for quantifying coronary calcium is based on the absolute mass [Hong *et al.* 2002, McCollough *et al.* 2007, Yoon *et al.* 1997]. To obtain absolute values for calcium mass, a calibration measurement of a calcification with known hydroxyapatite density has to be performed to determine a calibration factor c. The mass score is then defined as

$$M = \sum_i c\bar{I}_i A_i h \tag{2.4}$$

with h the slice thickness, A_i the plaque area at slice i and $\bar{I}_i$ the mean intensity value within A_i. Again, a plaque is defined according to the 130 HU intensity threshold criterion of the Agatston score.

2.1.4 Other Scores

Besides the aforementioned scores that are used in clinical routine, several other scores have been proposed for calcium scoring. Dehmeshki *et al.* [2007] proposed a volume score by using a modified expectation maximization of a statistical model for the measurement. Brown *et al.* [2008] suggested a coronary calcium coverage score (CCS) that represents the percentage of coronary arteries affected by calcified plaques. This CCS was highly associated with coronary heart disease events. Rollano-Hijarrubia *et al.* [2006a] proposed the usage of a 50% relative-threshold [Prevrhal *et al.* 1999] for the assessment of small calcified structures, like plaques, as it improved accuracy and strongly reduced inter-scanner and inter-protocol measurement dependency on a phantom study. However, this score assumes a homogeneous tissue around a plaque which may not always be the case in a clinical setting where a plaque can be surrounded by different tissues.

2.2 Factors Influencing the Calcium Scores

The other aforementioned scores were mainly proposed because of the disadvantages shown for the clinically used scores. For the Agatston score, a variability between examinations of up to 43% has been reported [Halliburton *et al.* 2005, Hong *et al.* 2003, Kopp *et al.* 2002, Lu *et al.* 2002, Ohnesorge *et al.* 2002, Oudkerk *et al.* 2008, Yoon *et al.* 2000]. As compared to the Agatston method, the *volume score* reduces the variability between examinations to some degree [Hong *et al.* 2003, Kopp *et al.* 2002, Lu *et al.* 2002, Ohnesorge *et al.* 2002], however, it also has its limitations. The *volume score* tends to overestimate the lesion size owing to the partial volume effect. Objects smaller than

one voxel contribute to the score with the entire voxel volume, and the volume score, which depends on the applied threshold, does not necessarily represent the true volume of calcium [Halliburton *et al.* 2005, Hong *et al.* 2003, Takahashi and Bae 2003, Van Hoe *et al.* 2003]. The errors from the volume and mass score show a clear relationship, whereas the relative error range for the mass score is smaller compared to that of the volume score [Hong *et al.* 2003].

Agatston, volume, and mass score are defined on a discrete voxel grid, *i.e.* a voxel is the smallest possible unit. Normally, the dimension of a plaque is not a multiple of a voxel such that at its border, the intensity value of a voxel represents a mixture of plaque and surrounding tissue. Depending on the examination parameters or the patient's position on the CT table, this intensity value changes from examination to examination. Hence, with the same underlying anatomy, a voxel may exceed in one scan the selected threshold value whereas in another scan, the intensity value can be below this threshold. This aforementioned *partial volume effect* is one of the main causes for the reported high variabilities of the clinically used calcium scores. A good overview of limiting factors for the quantification of small high-density structures and their effect on the visualization of surrounding tissues with CT system can be found in the report of Rollano-Hijarrubia *et al.* [2006b].

In the following, we will focus on the *volume score* and some of its influencing factors to motivate our development of ACCURATUM, a volume measure described in the subsequent section.

2.2.1 Reconstruction Kernel

During image reconstruction, a convolution is applied to either smooth or enhance high frequencies in the image. The shape of this kernel, in both the spatial and frequency domains, can be approximated by an iso-tropic two-dimensional (2D) Gaussian function [Rollano-Hijarrubia *et al.* 2006b]. According to the Siemens nomenclature, which will be used throughout this work, lower numerical kernel values (e.g. B20f, B25f) refer to narrower, *i.e.* smoother, filter functions in the frequency domain, which leads to stronger attenuation of the image high frequencies, thereby smoothing image edges. Larger kernel values (e.g. B70f, B80f) refer to wider, *i.e.* sharper, filter functions, which allow higher contribution of the image high frequencies, thereby reducing image blur [Rollano-Hijarrubia *et al.* 2006b]. Hence, different reconstruction kernels lead to varying intensity characteristics that affect the volume score, which was experimentally shown in several studies [Birnbaum *et al.* 2007, Cademartiri *et al.* 2007, Rollano-Hijarrubia *et al.* 2006b].

2.2.2 Tissue Density

The attenuation coefficient measured by a CT system depends on the tissue and its density. Hence, calcified plaques with a high density of hydroxyapatite are reflected by higher intensity values than less calcified plaques. As the reconstruction kernel causes a blurring of the intensity values, the partial volume effect is more pronounced in higher calcified plaques, which leads to an overestimation of the *volume score* as shown by Hong *et al.* [2003].

2.2.3 Tube Voltage

Lower tube voltages result in higher attenuation coefficients for hydroxyapatite [Berger and Hubbell 1987] and therefore increase the blurring, which in turn causes an overestimation of the plaque volume as more voxel intensities will reach the threshold value. Thomas *et al.* [2006] showed the impact of two different tube voltages on the intensity values of a calcium insert. As the *volume score* is defined through a fixed $130\ \mathrm{HU}$ threshold, different HU values have a direct influence on its outcome.

2.2.4 Spatial Resolution

The extension of a plaque depends on two factors. First, the size of the selected field of view, generally chosen to cover the whole heart, determines the in-plane resolution of a CT acquisition and thus the voxel's x and y extension. Second, in the z-direction, the voxel's size is defined by the selected slice thickness. Traditionally, a slice thickness of $3\ \mathrm{mm}$ is chosen to reduce the amount of radiation during calcium scoring. State-of-the-art CT systems, however, allow the acquisition of thinner slices without any additional X-ray exposure. The partial volume effect is affected by the resolution of a voxel such that its impact should be lowered with thinner slices. This was shown by Mühlenbruch *et al.* [2007] on a phantom study where the *volume score* could be improved when reducing the slice thickness from $3\ \mathrm{mm}$ to $1\ \mathrm{mm}$.

2.3 ACCURATUM

Based on the limitations of the calcium scores, we developed and introduced a score providing a better calcium volume measure with regard to accuracy, variability between examinations, dependency on plaque density, and acquisition parameters in comparison with the aforementioned *volume score*. A volume measure has been chosen as it provides – compared to the Agatston and mass score – additional morphological information about a plaque that might be of clinical interest.

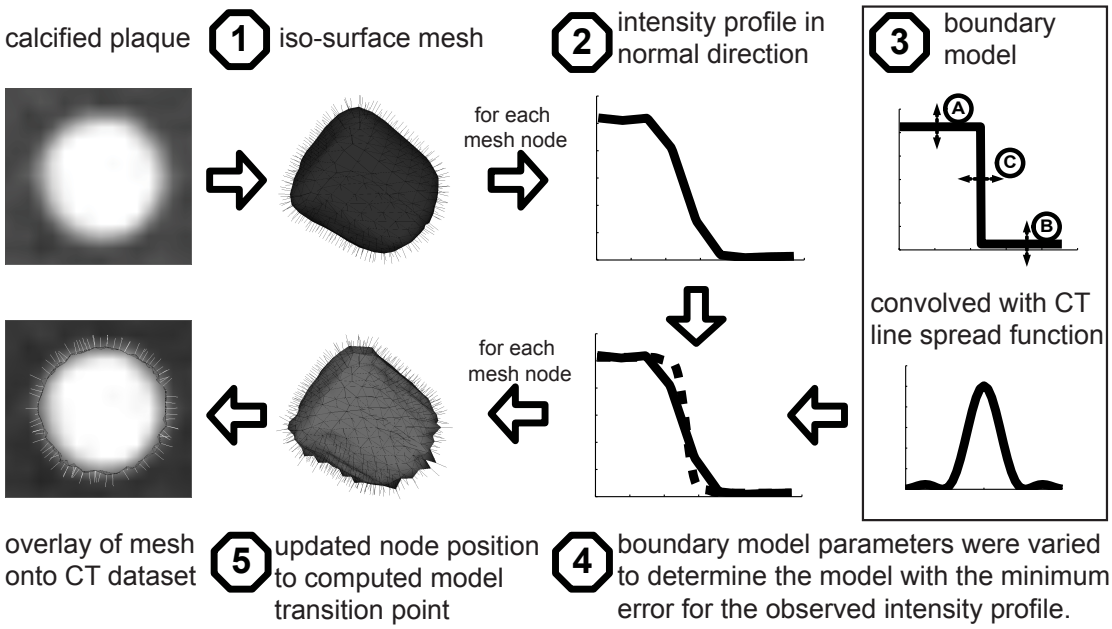

***Figure 2.1**: ACCURATUM uses a mesh-based representation for a calcified plaque to determine the position for each mesh node that most likely represents the boundary between plaque and surrounding tissue.*

The proposed volume measure and its underlying algorithm (Fig 2.1, steps 1-5) presented herein is subsequently referred to as ACCURATUM (A Calcium sCoring volUme measuRe – Accurate Through Using Meshes). To overcome the voxel as a discrete unit for volume measurements, each plaque is converted into an iso-surface mesh (Fig 2.1, step 1) such that its nodes n, representing the boundary between plaque and surrounding tissue, can be arbitrarily positioned in space, independently of the underlying voxel grid. As the position of this boundary is affected by the scanning characteristics of a CT system, the intensity profile along the surface normal of each node n_i (Fig. 2.2) is evaluated to determine the real position of the boundary.

In a first approximation, a CT system can be described as a linear shift invariant system such that its degenerative effect (such as the blurring of edges) can be regarded as the result $out(x, y, z)$ of a convolution of the input image $in(x, y, z)$ with a system-specific transfer function $t(x, y, z)$:

$$out(x, y, z) = \int\int\int i(x, y, z)t(x - u, y - v, z - w)\, dudvdw. \tag{2.5}$$

Hence, it would be desirable to reverse this process by applying the inverse transfer function on the CT image (deconvolution). However, this deconvolution is mathematically unstable. So instead of deconvolving, ACCURATUM convolves ideal boundaries be-

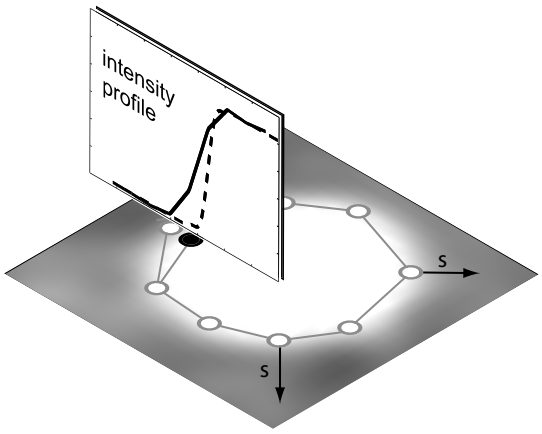

Figure 2.2: *The intensity profile is computed for each node along its surface normal direction s. The position of the node is updated to the boundary point (filled circle) obtained by fitting a boundary model (dotted line) to the measured intensity values (solid line) in the intensity profile.*

tween two materials A and B with the transfer function (step 3) and compares them with the extracted intensity profile (step 4). The ideal boundary with the minimum squared error to the intensity profile is taken, and the corresponding node n_i is repositioned to the location of the ideal boundary (step 5). In more detail, the five steps of ACCURATUM are explained in Algorithm 1 on page 32.

2.4 Experimental Setup

A commercially available cardiac CT phantom (QRM, Möhrendorf, Germany, www.qrm.de) mimicking the X-ray attenuation of real body tissues was taken for a comprehensive evaluation of both the state-of-the-art calcium volume score and our proposed method. This phantom contained well-defined calcifications and therefore allowed a detailed analysis with varying CT parameters and positions on the CT table. As ACCURATUM has parameters to be optimized, a common approach from the machine learning community is chosen in splitting up the data into *training* data sets - solely used for the parameter optimization – and into *evaluation* data sets on which the calcium volume score and ACCURATUM are evaluated.

2.4.1 Phantom

The phantom, described in detail in [Hong *et al.* 2002, Hong *et al.* 2003, McCollough *et al.* 2007, Mühlenbruch *et al.* 2005, Ulzheimer and Kalender 2003], consists of an

Algorithm 1 ACCURATUM

1. An iso-mesh representation of the calcified plaque using a marching cube algorithm [Lorensen and Cline 1987] is computed. The mesh is initialized with an iso-value defined by the mean intensity of the plaque according to the 130 HU threshold criterion of the Agatston score. If the mean intensity is below a threshold t_m and the 75%-quantile intensity is below a threshold t_q, ACCURATUM is not applied and the calcium scoring volume is taken.
2. The intensity profile of each node n_i along its surface normal direction in the xyz-coordinate system is extracted.
3. A set of ideal boundaries is convolved with the transfer function $t(x, y, z)$. According to Prevrhal *et al.* [1999], the spatial resolution of a CT system can be characterized by its 2D point spread function (PSF). As we assumed in correspondence with other studies [Prevrhal *et al.* 1999, Rollano-Hijarrubia *et al.* 2006b], a symmetric PSF, an iso-tropic line spread function (LSF) has been used to describe $t(x, y, z)$. The ideal boundaries are varied in the intensities for both materials A and B as well as in the position C of the boundary. Based on previous research results [Boone 2001], a $[\sin(x)/x]^2$ function was chosen for the approximation of the LSF instead of using a Gaussian LSF as done by Rollano-Hijarrubia *et al.* [2006b].
4. The sum of absolute differences (SAD) is calculated between each node's intensity profile and the set of convolved ideal boundaries. The ideal boundary with the minimum SAD is chosen.
5. Each node n_i is repositioned to the location of its ideal boundary. After processing all nodes, the volume of the final mesh is computed.

anthropomorphic body and a calibration insert containing three sets of calcified cylinders (Fig 2.3). The longitudinal axis of each cylinder is parallel to the phantom's longitudinal axis. The plaque equivalents are made of hydroxyapatite with the characteristics shown in Table 2.1. Unless otherwise stated, the phantom was aligned on the scanner table with its longitudinal axis parallel to the scanner's z-axis.

2.4.2 CT Parameters

All CT examinations were performed on a dual-source CT system (Somatom Definition, Siemens Medical Solutions, Forchheim, Germany) with a detector collimation of $2 \times 32 \times 0.6$ mm and a slice acquisition of $2 \times 64 \times 0.6$ mm by means of a z-flying focal spot [Flohr *et al.* 2006]. A reconstruction increment equal to the slice thickness was chosen for all CT data acquisitions. Following a standard calcium scoring protocol, a pitch of 0.2 and a tube current-time product of 80 mAs was selected. A typical field of view of

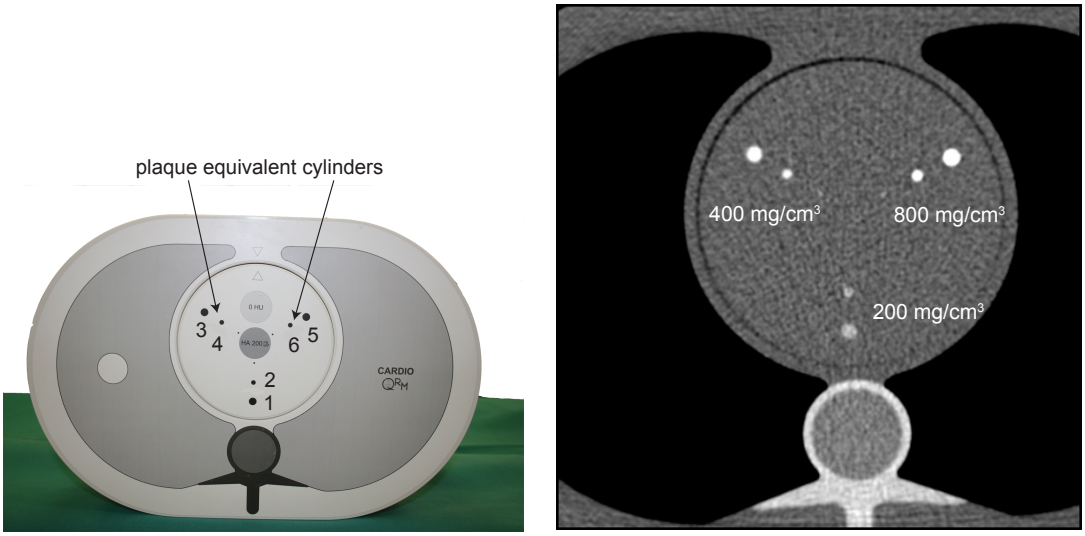

(a) Antropomorphic phantom. *(b)* CT slice showing plaque equivalents.

***Figure 2.3**: Antropomorphic phantom with three sets of calcified cylinders.*

***Table 2.1**: Density, length, diameter, volume and mass for each of the nine plaque equivalents made of hydroxyapatite (HA) that were contained in the cardiac CT phantom.*

label	density [$\mathrm{mg/cm^3}$]	length [mm]	diameter [mm]	volume [$\mathrm{mm^3}$]	mass [mg]
1	200	5.0	5.0	98.2	19.6
2	200	3.0	3.0	21.2	4.2
-	200	1.0	1.0	0.8	0.2
3	400	5.0	5.0	98.2	39.3
4	400	3.0	3.0	21.2	8.5
-	400	1.0	1.0	0.8	0.3
5	800	5.0	5.0	98.2	78.5
6	800	3.0	3.0	21.2	17.0
-	800	1.0	1.0	0.8	0.6

$170\ \mathrm{mm}$ lead to an in-plane pixel size of $0.332\ \mathrm{mm}$. The CT system was calibrated with room-temperature air immediately before the phantom measurements.

2.4.3 Training Data Sets

A first series of data sets (referred to as set A_t) was acquired by scanning the phantom with four different tube voltages (*i.e.*, $80\ \mathrm{kV}$, $100\ \mathrm{kV}$, $120\ \mathrm{kV}$, and $140\ \mathrm{kV}$) without changing its position on the CT table between the examinations. Each acquisition was reconstructed with an effective slice thickness of $3\ \mathrm{mm}$ using four different reconstruction kernels (B30f, B35f, B46f, B50f), resulting in a total of 16 data sets. This series was used to assess the accuracy of the volume measurement and its dependency on scanning parameters.

A second series of data sets was acquired to assess the variability of the measurements between examinations. The phantom was examined 10 times with constant parameters (*i.e.*, $120\ \mathrm{kV}$, B35f) at arbitrarily chosen positions along the z-axis of the CT table. The images were reconstructed with an effective slice thickness of $3\ \mathrm{mm}$ (denoted as set B_t) and $1\ \mathrm{mm}$ (denoted as set C_t).

2.4.4 Evaluation Data Sets

All CT examinations for the training data sets were repeated on the same day. These resulting *evaluation* data sets (A_e, B_e, C_e) were used for the evaluation of the developed algorithm. Additional evaluation data sets were acquired by varying the orientation of the phantom on the CT table with constant CT parameters (*i.e.*, $120\ \mathrm{kV}$, B35f). For one fixed position, the phantom was rotated around the y-axis of the CT system in 10° steps starting from 0° (*i.e.*, the phantom's longitudinal axis was parallel to the CT table's z-axis) to 90°. The resulting 10 examinations were reconstructed again with an effective slice thickness of $3\ \mathrm{mm}$ (denoted as set D_e) and $1\ \mathrm{mm}$ (denoted as set E_e).

2.4.5 Statistical Analysis

Quantitative variables were expressed as mean ($\pm$ standard deviation) and categorical variables as percentages. The *volume score* and ACCURATUM were compared regarding the accuracy of the measurements. Accuracy was defined as the ratio between measured volume and the ground-truth volume. An accuracy > 1 represented an overestimation, whereas an accuracy < 1 indicated an underestimation of the plaque volume. Variability was defined as the standard deviation of a measurement. Variability in scores for a single plaque between examinations was defined as the standard deviation of its accuracy. The variability in scores of a group of plaques was defined as the mean of the variabilities

from the individual plaques. Set A_e was taken to evaluate the dependency of both volume measures on the tube voltage and the reconstruction kernel. The variability of both volume measures was determined using data set B_e - E_e. Analysis of variance (ANOVA) was used on set A_e - E_e to statistically compare the accuracy of ACCURATUM with the *volume score*. A multivariate analysis of variance (MANOVA) was used on set A_e to evaluate the dependency of both volume measures on the plaque density, reconstruction kernel, and tube voltage. On set B_e - E_e, a paired Student's t-test was used to compare the mean accuracy and the variabilities of the different plaques between examination.

2.5 Results

Similar to other phantom studies [Hong *et al.* 2003, Hong *et al.* 2002, Mühlenbruch *et al.* 2005], the plaque equivalent cylinders with a diameter of $1\ \mathrm{mm}$ were not clearly discernible in most of the data sets. Only the highest calcified plaques in the 1-mm reconstruction could be consistently analyzed.

2.5.1 Training Data Sets

For all 3-mm training data sets (sets A_t and B_t), the parameters for ACCURATUM were heuristically tuned and set to $t_m = 200\ \mathrm{HU}$ and $t_q = 300\ \mathrm{HU}$, whereas for all 1-mm data sets (set C_t), the parameters were selected correspondingly as $t_m = 220\ \mathrm{HU}$ and $t_q = 300\ \mathrm{HU}$. These values were then used for the measurements in the evaluation data sets. It has been observed that an individual parameter set for each slice thickness allows a more precise optimization, although one set of global parameters would be desirable. This step is justified because, in general, only a small number of possible slice thicknesses occur for which ACCURATUM has to be calibrated.

2.5.2 Evaluation Data Sets

In the following, both volume measures, ACCURATUM and the *volume score*, are evaluated with regard to their dependency on the CT parameters, namely tube voltage and reconstruction kernel, and for their variability between examinations.

Scan parameters. Set A_e was used to investigate the dependency of the volume measures on the CT parameters. Averaging over all plaques of this set showed a significant decrease ($p = 0.001$) in the accuracy for the *volume score* with decreasing tube voltages ($80\ \mathrm{kV}$: 3.060 ± 2.674, $140\ \mathrm{kV}$: 1.839 ± 0.888). The tube voltage, however, had no impact ($p = 0.27$) on the accuracy of ACCURATUM ($80\ \mathrm{kV}$: 1.407 ± 1.223, $140\ \mathrm{kV}$:

1.168 ± 0.315). A significant decrease ($p < 0.001$) in the accuracy could be observed for the *volume score* when changing from a soft (B30f) to a sharp (B50f) reconstruction kernel. ACCURATUM proved to be more robust ($p = 0.19$) against the different reconstruction kernels. The *volume score* significantly depended on the plaque density ($p < 0.0001$) whereas ACCURATUM showed no significant dependency on plaque density (p=0.84).

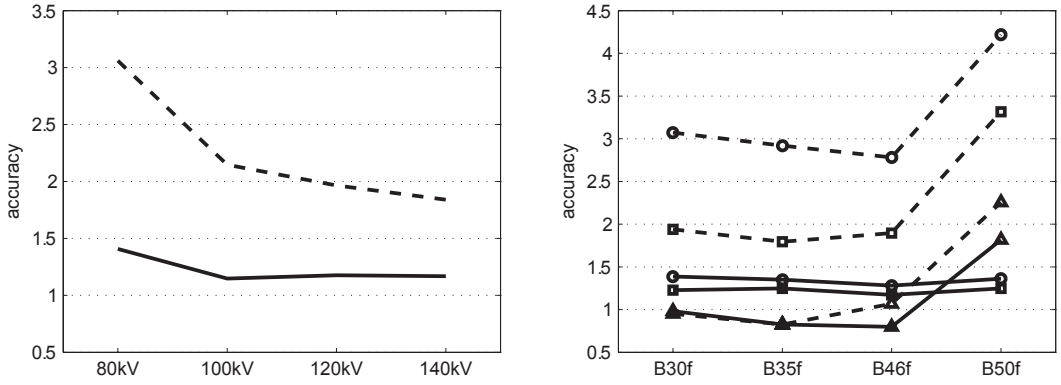

(a) Tube voltage. *(b)* Reconstruction kernel.

***Figure 2.4**: For each tube voltage (a) and reconstruction kernel (b), the mean accuracy for the* volume score *(dashed line) and ACCURATUM (solid line) was computed. The* volume score *showed a significant decrease ($p < 0.001$) in accuracy particularly at lower tube voltages, whereas varying tube voltages had no impact ($p = 0.55$) on ACCURATUM. In comparison to the* volume score*, ACCURATUM proved to be more robust ($p = 0.18$) against varying reconstruction kernels. For better illustration, the plaques are grouped by their hydroxyapatite (HA) density: ($\triangle$) for $200\ \mathrm{mgHA/cm^3}$, ($\square$) for $400\ \mathrm{mgHA/cm^3}$, and ($\circ$) for $800\ \mathrm{mgHA/cm^3}$.*

Variability between examinations. The variability was evaluated with constant scan parameters by translating the phantom along the z-axis of the CT system (set B_e and C_e) and by rotating it around the y-axis of the CT table (set D_e and E_e) for a fixed position.

Variability between examinations – translation. For the 3-mm data sets (set B_e), ACCURATUM (1.330 ± 0.544) was significantly ($p < 0.0001$) more accurate than the *volume score* (1.862 ± 0.925) in terms of the mean accuracy over all plaques. Over the 10 scans for the plaques in set B_e, ACCURATUM had a variability of ± 0.261, whereas the *volume score* had a variability of ± 0.121, with significant differences between the methods ($p = 0.036$).

For the 1-mm data sets (set C_e), ACCURATUM (1.082 ± 0.121) was also significantly ($p < 0.0001$) more accurate than the *volume score* (1.651 ± 0.558) for the mean accuracy over

all plaques. ACCURATUM (± 0.051) had a variability similar ($p = 0.192$) to the *volume score* (± 0.081).

Variability between examinations – rotation. Similar results were obtained while rotating the phantom. For the 3-mm data sets (set D_e), ACCURATUM (1.361 ± 0.571) was significantly ($p < 0.0001$) more accurate than the *volume score* (1.847 ± 0.973) over all plaques. Over the 10 scans for the plaques in set D_e, ACCURATUM had a variability of ± 0.179, whereas the *volume score* had a variability of ± 0.080, with non-significant differences between the methods ($p = 0.143$).

For the 1-mm data sets (set E_e), ACCURATUM (1.095 ± 0.138) was also significantly ($p < 0.0001$) more accurate than the *volume score* (1.651 ± 0.557) for the mean accuracy over all plaques. ACCURATUM (± 0.051) had a variability similar ($p = 0.157$) to the *volume score* (± 0.061).

Slice thickness. A reduction in the effective slice thickness from 3 mm (set B_e, D_e) to 1 mm (set C_e, E_e) led to a significant improvement in the accuracy ($p < 0.0001$) and variability ($p < 0.0001$) for both volume scores.

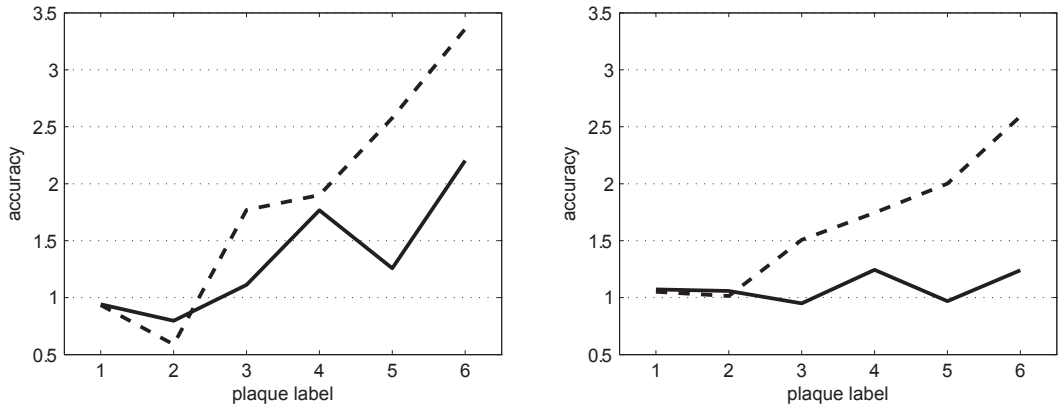

(a) 3 mm. *(b)* 1 mm.

Figure 2.5*: For each plaque, the mean accuracy was computed. ACCURATUM (solid line) was less dependent on the plaque density for 3-mm slices (a) than the* volume score *(dashed line). Better results for both methods could be achieved by using a slice thickness of* 1 mm *(b).*

The dependency of both measures on the plaque density (set B_e - set E_e) is shown in Fig. 2.5. For the 3-mm data sets, medium and highly calcified plaques (plaques 3-6) were heavily overestimated by the *volume score* whereas ACCURATUM was less dependent on the plaque density. For an effective slice thickness of 1 mm, the proposed method was even more robust ($p = 0.32$) towards differing plaque densities.

2.6 Discussion and Conclusion

In this chapter, we have presented calcium scores that are used as a general risk assessment for cardiovascular diseases. It has been shown that the clinically used *volume score* has high variabilities in its application, especially through its dependency on the reconstruction kernel, the tube voltage, the variability between examinations and the slice thickness. In accordance with the literature, these impacts could be reproduced and confirmed by our phantom study.

In order to overcome these limiting factors, ACCURATUM, a new method for measuring calcified plaque volume, has been introduced. ACCURATUM overcame the limitations of the *volume score* by being more accurate and less dependent on the scanner parametrization measures, such as the tube voltage. Therefore, ACCURATUM is theoretically suitable for the low-dose $80\ \mathrm{kV}$ protocol proposed by Thomas *et al.* [2006]. In contrast to the calcium scoring algorithm by these authors, which required an adaptation of the threshold, ACCURATUM can be applied without any algorithm and parameter changes.

ACCURATUM was also robust against variations in the reconstruction kernel and did not show the typical decrease in the accuracy with the use of sharper reconstruction kernels as observed by Cademartiri *et al.* [2007]. The evaluation using the standard scanning protocol showed an enormous overestimation for the volumes of highly calcified plaques with the *volume score*, whereas ACCURATUM was less dependent on the plaque density.

The use of an effective slice thickness of $1\ \mathrm{mm}$ led to a significant improvement in accuracy and variability for both ACCURATUM and for the *volume score*. This effect has already been reported for the *volume score* [Mühlenbruch *et al.* 2007]. As for state-of-the-art CT systems, 1-mm slices can be reconstructed from the same raw data as 3-mm slices, no additional X-ray exposure is caused. Thus, the use of 1-mm slices for measurements of plaque volumes is recommended.

Especially for 1-mm slices, ACCURATUM was very robust to plaques with different densities which allowed a reliable measurement of their volume. Generally, a low variability and therefore a high robustness is more important for a score than its absolute accuracy. Measures with low variability but a constant offset to their ground truth can be compensated with a calibration factor whereas highly variable scores are hard to compare. ACCURATUM has two parameters. For their determination, a set of training data has been used. As only phantom scans from a single CT system were available, no conclusion can be drawn whether the obtained parameters are directly transferable to other CT systems or if the proposed algorithm has to be calibrated once on each CT system. The proposed method is initialized by a single click into a calcified plaque. Its volume is then automatically computed within $1 - 2\ \mathrm{s}$ on average (C++, Pentium 4, 3 GHz, 2 GB RAM). A plaque may be surrounded by different tissues as the optimal boundary transition between plaque and its surroundings is computed for each mesh node separately.

We also applied ACCURATUM to a highly calcified 1-mm plaque that was only visible in the 1-mm reconstructions. ACCURATUM, however, did not perform (4.530 ± 1.557) better than the *volume score* (4.003 ± 1.155) as the convolution approach requires a minimum object size such that opposite boundaries do not influence each other. Extracting only the mesh (step 1 of ACCURATUM) and taking the resulting volume led to an accuracy of 1.501 ± 0.373. So future work should concentrate on defining criteria to automatically determine when the convolution approach is likely to fail and therefore only the mesh extraction should be applied.

3

Extraction of Anatomical Structures

Anatomical structures such as the heart, the aorta or the coronary arteries are used in the diagnosis process of coronary heart diseases to measure for example the ejection fraction, geometrical extensions or the amount of atherosclerosis, respectively. For this purpose, those anatomical structures have to be localized in the data sets and in some cases they even have to be delineated – in medical imaging known as segmenting. The segmentation task – when performed manually – is time-consuming. Therefore, a wide range of (semi-)automatic algorithms have been proposed to speed up the process.

The aim of this work was to define and develop algorithms for anatomical feature extraction. In particular, algorithms for the detection of the ascending aorta and the tracking, segmentation, and labeling of the coronary arteries will be developed, as these structures will later on be used for the assessment of atherosclerosis.

This chapter will first introduce an automatic detection of the ascending aorta. Afterwards, a semi-automatic tracking and subsequent segmentation of the coronary arteries will be presented. Finally, an automatic labeling of the coronary artery tree will be proposed.

3.1 Ascending Aorta Detection

The ascending aorta is an important anatomical landmark because it is the starting point for both physicians and computer aided diagnosis (CAD) tools for the assessment of coronary heart diseases. Physicians first navigate to the ascending aorta to detect the outlets of the coronary arteries. Then, they follow the course of the coronary arteries to their distal ends. CAD tools used in clinical workstations mimic the same approach, *i.e.* they also need the location of the ascending aorta as part of their assessment. This can be done either by user interaction or by automatic extraction. As the ascending aorta has a large cross-sectional area, it is also used to extract statistical information about the contrast agent distribution. In some algorithms, these values are used as an initial estimation for adaptive thresholds for coronary artery segmentation.

3.1.1 Related Work

Three different algorithmic approaches for the automatic detection of the aorta have been proposed so far: (1) Hough transform based approaches, (2) approaches using morphological operators, and (3) ray cast approaches. Within all approaches, anatomical knowledge about the aorta is incorporated, namely its approximately circular shape in axial CT slices.

(1) The Hough transform, originally introduced for straight lines [Hough 1962] and later extended for circular structures [Kimme *et al.* 1975] is a feature extraction technique widely used in image analysis. With this technique, imperfect instances of objects can be detected. This is done through a parametrization of an object by its features, like the slope and interception for lines or the radius and center-point for circles. For object detection, a voting in the so-called Hough space – the space spanned by the parameters – is performed. Each point in the original image space exceeding a certain threshold value is regarded as candidate belonging to an object. In general, a unique allocation of this point to an object is not possible. In the case for circles, for example, a single point may lie on the circumference of various circles with different radii or different center-points. Therefore, each possible parameter combination leading to this point in the image space is voted in the Hough space. In theory, this is no problem, but for practical implementations, the parameter range must be limited and discretized for computational reasons. After traversing the whole image space, the point with the maximum number of votes in the Hough space is finally taken as the object. If more than one object is expected in the image space, the results in the Hough space can be further processed by non-maximum-suppression or clustering techniques to extract multiple objects.

Kovacs *et al.* [2006] used the Hough transform in CTCA data sets to detect both the ascending and descending aorta to enable the automatic analysis of aortic dissections. Fritz *et al.* [2008] combined the Hough transform and a cylindrical model matching approach to automatically locate the ascending aorta within CTCA data sets. For non-contrast CT images, Kurkure *et al.* [2008a] proposed a method for aorta localization using the Hough space as a medialness feature space. Dynamic programming is applied on that space to find the points corresponding to the center of the aorta in subsequent axial slices.

(2) Mathematical morphology is a theory for the analysis of spacial structures which was initiated by Matheron and Serra [1982]. It is a set-theoretic method of image analysis providing a quantitative description of geometrical structures. For its application, a structuring element, *i.e.* a shape, has to be defined which is then used to probe or interact with an image, with the purpose of drawing conclusions on how this shape fits or misses the shapes in the image. Depending on the definition of the structuring element and the selected set operation, morphology can provide boundaries of objects, their skeletons, or their convex hulls. It is also useful for many pre- and post-processing techniques, especially in edge thinning and pruning. For the automatic detection of the ascending aorta in CTCA images, Bouraoui *et al.* [2008] used a morphological grayscale hit-or-miss trans-

form. Anatomical knowledge about the ascending aorta was used for the definition of the morphological structuring element.

(3) An iterative ray casting method was proposed by Lorenz *et al.* [2005] to detect a broad range of anatomical objects, like the descending aorta in CTCA data sets [Lorenz *et al.* 2004a]. Following this approach, various one-dimensional search rays are propagated through the image data and the intensities are sampled and analyzed along each search ray. The results of such an analysis – defined through anatomical constraints like extension and intensity values – are used to set up a subsequent search in order to probe the image data in other directions to either confirm or discard the results of the previous search. Details about ray casting can be found in the next section as this approach is the basis for our proposed algorithm for the automatic detection of the ascending aorta.

3.1.2 Methods

Although the Hough Transform is a standard approach that is widely used, it has some disadvantages like limited computational efficiency and its sensitivity to noise and to deviations of the model shape. Therefore, we choose the ray casting approach presented for the descending aorta [Lorenz *et al.* 2004a] as the basis and adapted it for the automatic detection of the ascending aorta.

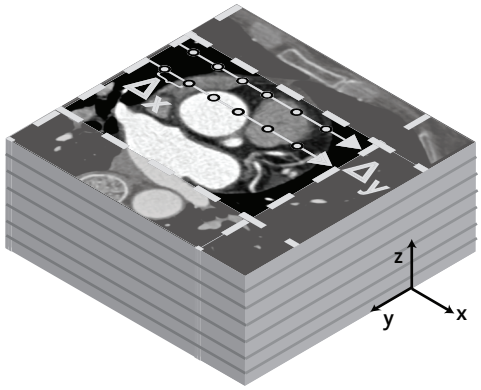

***Figure 3.1**: Within a fixed volume of interest in a data set, a search ray traverses the voxels to search for candidate points of the ascending aorta.*

A typical axial cardiac CT slice set contains – besides the ascending aorta – several other elliptical structures. Therefore, to exclude some possible false candidates in advance, it is desirable to limit the search for the ascending aorta to a certain volume of interest (VOI). However, to avoid user interaction, the VOI should either be fixed for all data sets or it should be computed automatically based on the given data set. We followed the approach by Lorenz *et al.* [2004a] and defined a fixed VOI defined relative to the extension of the data set.

Given this VOI, a search ray passes its voxels in the positive x-direction (left to right), line by line (in the positive y-direction), for each axial slice (Fig. 3.1). For voxels above a predefined intensity threshold, several geometric criteria that a candidate point for the ascending aorta must fulfill are evaluated. In contrast to the descending aorta, the VOI around the ascending aorta contains more elliptical structures (e.g. right atrium, right ventricle) that fulfill the criteria used by Lorenz *et al.* [2004a]. Therefore, additional constraints were introduced to validate circularity – as the ascending aorta is the most circular structure within the VOI. The complete detection algorithm that extracts a list $\mathcal{L}$ of candidate points for the ascending aorta is described in Algorithm 2.

Algorithm 2 Ascending Aorta Detection

1. Trace search ray in x-direction while gray values stay below a given primary threshold th_p (Fig. 3.2(a)).
2. If primary threshold is met, continue with search ray and look for an intensity transition that falls below a secondary threshold th_s (Fig. 3.2(a)).
3. If transition is reached, search backwards for transition to above th_p (Fig. 3.2(a)).
4. If the distance d_x of the found structure is within d_{min} and d_{max}, compute center p_x between both transition points and search from this center with the procedure as described above for the extension d_y in y-direction. Compute center point p_y in y-direction and search for extension $d_{+\pi/4}$ and $d_{-\pi/4}$ in direction of the two angle bisectors in the xy-plane (Fig. 3.2(b)).
5. Compute ratio $a = |d_y/d_x - 1|$.
6. If $d_{min} < d_i < d_{max}\ \forall d_i, d_i \in \{d_x, d_y, d_{+\pi/4}, d_{-\pi/4}\}$ and ratio a is below threshold th_a, add p_y to the candidate list $\mathcal{L}$.
7. Set search ray to the next line or slice, respectively, and continue with step 1 until whole VOI is processed.

After the extraction of candidate points, neighborhood clusters are computed out of the list $\mathcal{L}$ (Fig. 3.3(a)). An initial cluster is defined with the first candidate point of $\mathcal{L}$. For each remaining point p_l of $\mathcal{L}$, it is checked if a cluster already contains an element that is less than a given euclidian distance d_{clust} away from p_l. If yes, the candidate point p_l is added to this cluster. Otherwise, a new cluster is initiated. The cluster containing the most elements is taken as the representant of the ascending aorta (Fig. 3.3(b)).

In addition to Lorenz *et al.* [2004a] we introduce the ratio a and the distances $d_{+\pi/4}$ and $d_{-\pi/4}$ along the direction of the two angle bisectors as extra constraints for the candidates. To speed up the detection process, the search ray is not propagated voxel by voxel, but is incremented by Δ_x, Δ_y, and Δ_z, in x-, y-, and z-direction, respectively. A priori anatomical knowledge about the expected position of the ascending aorta is used to define the VOI.

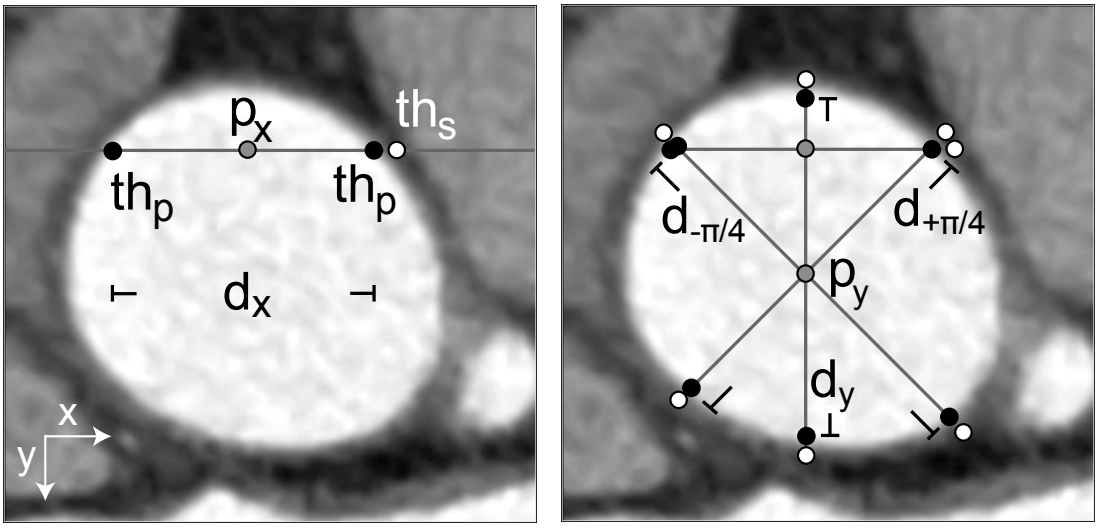

(a) Extension in x-direction. *(b)* Candidate point p_y.

***Figure 3.2**: Detection of the ascending aorta. Within a predefined volume of interest (VOI), search rays are propagated following a two-level threshold approach to compute the extension in x-direction (a) and afterwards in y-direction as well as in direction of the two angle bisectors (b). If geometric constraints are fulfilled, the point p_y is added to the list of ascending aorta candidates.*

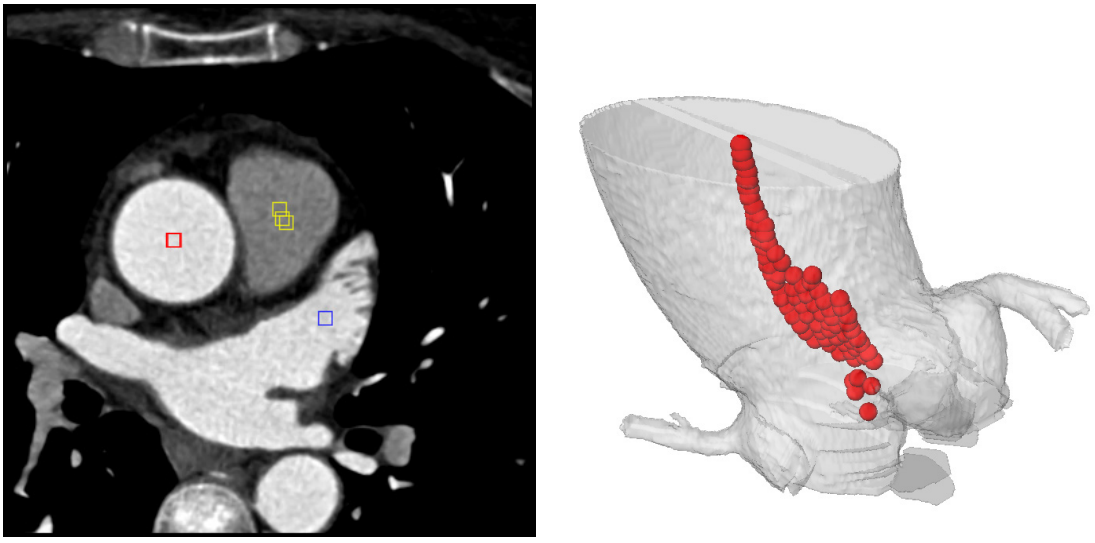

(a) Neighborhood clusters. *(b)* Cluster in the ascending aorta.

***Figure 3.3**: Neighborhood clusters are computed out of the list of candidate points (a) and the cluster with most elements is finally taken to represent the ascending aorta (b).*

We used 100 CTCA data sets (standard cardiac protocol, Siemens Definition) to fix a set of parameters (see Table 3.1) minimizing the number of false detections.

***Table 3.1**: Based on 100 data sets, a set of parameters is determined and fixed for an evaluation on a larger number of data sets. The volume of interest (VOI) is given as a percentage of the total data set extension in the corresponding direction, whereby the z-direction is defined in the cranial direction.*

parameter	value	unit
Δ_x	1.0	mm
Δ_y	5.0	mm
Δ_z	1.0	mm
th_p	180	HU
th_s	100	HU
d_{min}	20	mm
d_{max}	70	mm
d_{clust} (iso-tropic)	5.0	mm
th_a	0.25	-
VOI_x	0-0.75	-
VOI_y	0.25-0.70	-
VOI_z	0.5-1.0	-

3.1.3 Experimental Setup and Results

We evaluated the proposed ascending aorta detection algorithm on 297 CTCA data sets from different CT scanners (Siemens Definition, Siemens Sensation 64, Siemens Sensation Cardiac 64, Siemens Sensation 16). Data sets used for parameter optimization were not included in the evaluation. The in-plane resolution ranged from $0.236 - 0.512$ mm, the slice spacing varied between $0.3 - 0.8$ mm and the slice thickness varied between $0.6 - 1.0$ mm. Each slice contained 512×512 voxels and the number of slices varied between 150 and 591.

A point within the ascending aorta was correctly detected in 288 (97.0%) data sets. For nine data sets, the aorta could not be detected. Instead, a point within the right ventricle (eight times) or the descending aorta (once) was chosen by the algorithm. In these cases, the second largest cluster represented the ascending aorta. The mean detection time for the ascending aorta was 0.30 s and ranged from $0.13 - 0.77$ s on a Pentium 4 with 3 GHz and 2 GB RAM.

3.2 Coronary Artery Tracking

For the assessment of atherosclerosis in coronary arteries, it is essential to locate the coronary arteries themselves in a data set and follow their course, starting from the outlet in the ascending aorta till the distal ends of the various branches of the coronary artery tree. This process is referred to as vessel tracking – or more precisely in our case – coronary artery tracking. The goal of the tracking is to extract a path, *i.e.* a series of points, describing the course of the coronary arteries. The only restriction existing for the path is that it runs somewhere within the vessel lumen. For centerline extraction, however, the path is constrained to run in the geometrical center of the vessel lumen. Hence, to define the center, the vessel lumen has to be known. Therefore, centerline extraction is closely related to vessel segmentation where the vessel lumen is delineated from the surrounding tissue.

In general, there is no problem for a human expert to manually track coronary arteries within a data set. The reader can intuitively overcome discontinuities in the vessel path like stenoses (Fig. 3.4(a)) or a changing intensity distribution of the injected contrast agent. Further, the reader easily distinguishes between the targeted vessels and structures touching the vessel like the left ventricle having similar intensity characteristics as the coronary arteries (Fig. 3.4(b)) or crossing vessels (Fig. 3.4(c)). However, these discontinuities present significant challenges for vessel tracking algorithms.

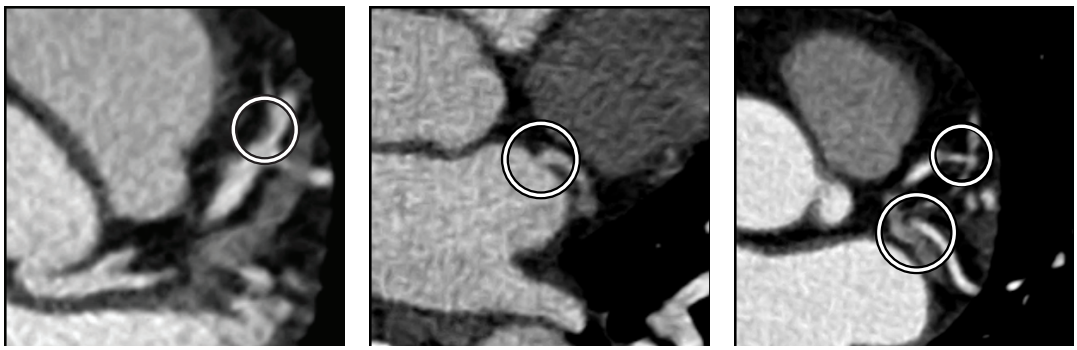

(a) Stenosis *(b)* Vessel close to left atrium *(c)* Crossing vessels

***Figure 3.4**: Although a reader can intuitively overcome discontinuities in the vessel path caused by stenoses (a) and although the reader can distinguish between the targeted vessel and structures touching the vessel like the left ventricle (b) or crossing vessels (c), those anomalies are a challenging task for vessel tracking algorithms.*

3.2.1 Related Work

Although various vessel tracking algorithms have been proposed over the past years, the task of tracking is still challenging and not yet solved in a convenient manner which reflects the high number of publications dealing with this topic. Felkel *et al.* [2001] reviewed existing vessel tracking algorithms for angiographic CT data sets in 2001. Since then, many other vessel tracking algorithms have been proposed [van Andel *et al.* 2004, Frangi *et al.* 2000, Friman *et al.* 2008a, Goel *et al.* 2008, Li and Yezzi 2007, Maddah *et al.* 2002, Poon *et al.* 2007]. These vessel tracking algorithms were proposed for vascular structures in general and may be applied – with some adaptations – for the specific purpose of coronary artery tracking.

Besides these general vessel tracking approaches, specialized algorithms for the tracking of coronary arteries in CT data sets have been proposed. In general, a grouping of these algorithms into their basic approaches is difficult because they comprise a mixture of different feature extraction techniques. Therefore, we will follow the classification of the Rotterdam Coronary Artery Algorithm Evaluation Framework (`http://coronary.bigr.nl`) and group the algorithms by their degree of needed user interaction. Automatic methods track the coronary arteries without any user interaction. Approaches with minimal user interaction require up to one manually placed seed point per coronary artery, whereas interactive tracking approaches have no limit on the degree of user interaction.

Automatic tracking. Zambal *et al.* [2008] used a 3D model of the heart to detect its approximate position. Based on this information, candidates for coronary artery seeds were calculated. Afterwards cylindrical sampling patterns were fitted to track the coronary arteries. Tek *et al.* [2008] first detected the aorta which was then used as an initial mask for ostia detection. Afterwards, the ostia locations were detected via a vessel centerline extraction method which tracked the center axis of the coronaries starting from the aorta surface. The full centerline tree of the coronary arteries was finally computed via a multiscale medialness-based vessel tree extraction algorithm [Gülsün and Tek 2008] which started a tracking process from the ostia locations until all the branches were reached. Kitslaar *et al.* [2008] first detected the aorta and the entire heart region. Afterwards, candidate coronary artery components were detected in the heart region after a masking of the cardiac blood pools. Based on their location and geometrical properties the structures representing the right and left arteries were selected from a candidate list. Finally, starting from the aorta, connections between theses structures were made resulting in a final tracking of the whole coronary artery tree. Wang and Smedby [Wang and Smedby 2008] proposed an automatic algorithm based on competing fuzzy connectedness theory [Wang and Smedby 2007] for the tracking of the coronary arteries. For its initialization, the ascending aorta was detected in a pre-processing step to extract seed points for the coronary arteries.

Minimal user interaction. Krissian *et al.* [2008] estimated for each voxel the probability of belonging to a coronary vessel and afterwards applied a vesselness measure on the resulting probability map to obtain a cost for each voxel. The vessel starting point was then obtained automatically, while the end point had to be provided by the user. Finally, the path with the minimal cost between both points was regarded as the tracked coronary vessel. Dikici *et al.* [2008] first isolated the aorta and computed its surface. Then, they applied a two-stage Hough-like election scheme to the image volume to detect points which exhibit axial symmetry. From the axial symmetry image a graph was constructed. Finally, this graph was searched for the optimal path from the user supplied distal end points to any point on the surface of the aorta. Merges *et al.* [2006] tracked the coronary arteries by a simulated wave propagation method. This approach allowed the extraction of anatomical spatial relations that were used to bridge tracking gaps caused by stenoses or image artifacts. This method had to be initialized by a click into the ascending aorta. Carrillo *et al.* [2007] recursively tracked the branches of the coronary artery tree and simultaneously detected bifurcations by analyzing the binary connected components on the surface of a sphere that moves along the vessels. The segmentation within the sphere was performed using a clustering algorithm based on both geometric and intensity information.

Interactive tracking. Lesage *et al.* [2008] proposed a Bayesian, stochastic tracking algorithm for the tracking of coronary arteries. Based on techniques from particle filtering, this algorithm relied on a constrained, medial-based geometric model and on an original sampling scheme for the selection of tracking hypotheses. Metz *et al.* [2007] applied region growing to track the coronary arteries in a semi-automatic manner and to automatically extract bifurcation information. Friman *et al.* [2008b] used a multiple hypothesis tracking methodology which was complemented with a standard minimal path search for the interactive tracking of coronary arteries. Toumoulin *et al.* [2003] tracked the coronary arteries with a geometrical moment-based method and used a level set approach for a refinement of the results. Szymczak [Szymczak 2008] tracked the coronary arteries by first determining core points that tended to concentrate along the centerlines of vessels. Then, with given seeds by the user, a weighted core graph was built by connecting nearby core points until both user placed seed points were connected. Bauer and Bischof [2008] applied an edge based tube detection on the Gradient Vector Flow and an analysis of the resulting vector field. After identification of tubular structures, their centerlines were extracted and grouped into complete tree structures. Hoyos *et al.* [2008] used region growing with an interactively defined intensity range from manually placed seed points to track the coronary arteries. Castro *et al.* [2008] tracked the coronary arteries with morphological grayscale local reconstruction operators.

3.2.2 Methods

For the tracking of coronary arteries in CTCA data sets, we address several prerequisites to the algorithm. First of all, it must be able to deal with atherosclerosis which is reflected by intensity changes within the coronary arteries caused by stenoses or different types of plaques. Further, it should be able to handle motion artifacts. Although the latest CT system generation provides good temporal resolution, motion artifacts still cannot be excluded which result in spatial offsets of the coronary arteries between slices in a CT data set such that an automatic tracking stops in general, and has to be manually re-initialized. Finally, the coronary artery tracking algorithm should be fast and robust.

Besides the tracking of the coronary arteries, we further want to extract the coronary artery tree, *i.e.* the hierarchical branching information between the tracked vessels. This information allows – in a next step – a labeling of the extracted branches according to the AHA scheme and therefore simplifies the automatic annotation of detected lesions within the tracked coronary tree.

To deal with all the aforementioned requirements, we propose a semi-automatic coronary artery tracking based on the live-wire approach. This approach allows user-interaction to overcome motion artifacts or to bridge stenoses and it is further flexible in its design such that it can be easily extended with additional cost functions.

The live-wire algorithm is based on Dijkstra's algorithm [Dijkstra 1959], a graph search algorithm that – given a source vertex in the graph – finds the path with lowest costs – defined as the shortest path – between the source vertex and every other vertex. Dijkstra's algorithm works by keeping for each vertex v, the cost $dist(v)$ of the shortest path found so far between the start vertex $source$ and v. The algorithm is initialized with the distance 0 at the start vertex and a set Q containing all vertices of the graph. In each step, one vertex u is expanded, *i.e.* it is removed from Q. This vertex u is chosen to be the vertex in the set Q with the least $dist(u)$ value. When u is expanded, the algorithm calculates if u can improve the shortest path of any of its neighboring vertices v. In detail, it is evaluated if the shortest path between $source$ and v can be improved by first following the shortest path to u and then traversing the edge connecting u and v. If this new path is better, the algorithm updates the shortest cost path to the neighbor with the new smaller value. When the algorithm terminates, it has computed for each vertex v its distance $dist(v)$ to the start point as well as its predecessor vertex $previous[v]$ in the shortest path. Algorithm 3 on page 51 shows Dijkstra's algorithm in pseudo code.

Dijkstra's algorithm has been adapted to image processing by Barrett and Mortensen [Barrett and Mortensen 1997, Barrett and Mortensen 1996, Mortensen and Barrett 1995] who used this algorithm for their live-wire method to interactively extract object boundaries. As costs, they used a Laplacian zero-crossing feature, a gradient magnitude feature and a gradient direction feature. Live-wire algorithms are applied in medical image processing for the extraction of anatomical features, in particular for the extrac-

Algorithm 3 Dijkstra algorithm

for all vertices v in Graph **do**
  $dist[v] \Leftarrow \infty$
  $previous[v] \Leftarrow NULL$
end for
$dist[source] \Leftarrow 0$ {distance from source to source}
$Q \Leftarrow$ the set of all vertices in Graph
while $Q \neq \emptyset$ **do**
  $u \Leftarrow$ node in Q with smallest dist[]
  remove u from Q
  for all neighbors v of u **do**
    $alt \Leftarrow dist[u] + d(u, v)$ {d(u,v) distance between two nodes}
    if $alt < dist[v]$ **then**
      $dist[v] \Leftarrow alt$
      $previous[v] \Leftarrow u$
    end if
  end for
end while

tion of object boundaries [Falcao *et al.* 1998, Falcao *et al.* 1999, Falcao *et al.* 2000, O'Donnell *et al.* 2001] or for the tracking of vascular objects [van Andel *et al.* 2004, Poon *et al.* 2007]. In order to be able to apply a graph based algorithm on CT data, voxels are regarded as vertices and edges – connecting the nodes – are defined according to given neighborhood relationships in the data set – in our case a 26-neighborhood connectivity.

Cost functions

In the live-wire algorithm proposed by Barrett and Mortensen [1997] the distance $d(u, v)$ between two vertices u and v is composed of three different costs, namely a gradient magnitude cost, a Laplacian zero-crossing cost and a gradient direction cost. Since then, other features have been suggested for live-wire like a length cost or a vesselness cost [Poon *et al.* 2007].

For our purpose, an intensity and a gradient cost revealed to be sufficient to provide a good optimum between needed user interaction, robustness and the performance of the algorithm. In general, cost functions are defined to penalize voxels not belonging to the targeted anatomy. Hence, costs should be low for voxels lying within the contrast-enhanced coronary arteries and high for voxels lying elsewhere.

For the intensity cost, we achieve this with a four-step cost function (Fig. 3.5(a)) based on an intensity cost function proposed by Kanitsar [2001]. The four steps have shown to perform well with the various different observed intensity distributions within coronary

arteries. In general, the distribution of the contrast agent is not homogenous such that the intensities vary along the course of the coronary arteries. Lower intensity values, for example, can be observed in the side branches of the coronary artery tree.

The aim of the gradient feature is to assign a higher cost to voxels located in the boundaries of the vessel, based on the assumption that in the direction of the central axis of the vessel the intensity of the voxels is more uniform than towards the direction of its boundary. Therefore, we selected a linear gradient cost function as shown in Figure 3.5(b).

A detailed description of the cost functions as well as the selected thresholds and parameters of the proposed live-wire algorithm for the purpose of vessel tracking can be found in [Quirante Ruiz 2007].

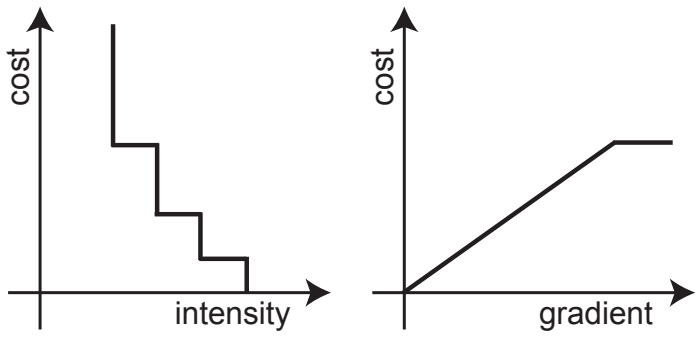

(a) Intensity cost function. *(b)* Gradient cost function.

***Figure 3.5**: The proposed coronary artery tracking algorithm is based on a live-wire approach for which two different cost functions are defined.*

Seed point placement

Two sorts of seed points are distinguished for our vessel tracking, namely start seed points and end seed points. The former ones are starting points for the live-wire algorithm whereas the latter ones represent termination points for the path search. For each start seed point, a separate path search is initialized.

Start seed points have to be manually placed in the distal segments of the coronary artery tree. Further, an end seed point has to be placed at the orifice for each the left and right coronary branch. A common end point for both branches in the ascending aorta would be feasible but would simultaneously increase the running time of the live-wire algorithm as too many points within the ascending aorta will be proceeded during the search for the termination point.

The live-wire algorithm normally terminates for a start seed point when Dijkstra's path search reaches one of the end seed points. Due to motion artifacts or stenoses, it might

happen that a path between a start seed point and an end seed point cannot be found within a reasonable time. Therefore, an additional termination criterion has been introduced, namely the maximum number of allowed iterations for a path search. If no path can be found, the user can manually insert paths into the coronary tree to bridge critical areas like stenoses or motion artifacts (Fig. 3.6). A manually drawn path consists of a start seed point at its proximal beginning and an end seed point at its most distal extension. Between these two seed points, an arbitrary number of supporting points forming the path can be inserted. So, the path search terminates at the distal end of the manually inserted path and is afterwards re-initialized at its proximal beginning.

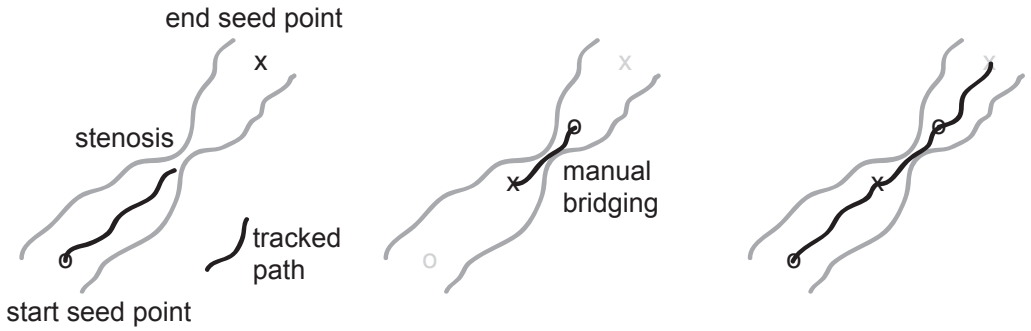

(a) Problem stenosis. *(b)* Manual bridging. *(c)* Result.

***Figure 3.6**: Problematic regions in coronary artery tracking such as stenoses (a) can be bridged by manually inserting a path (b) with an additional start and end seed point such that the complete artery can be finally tracked (c).*

Coronary Tree extraction

Besides the tracking of the coronary arteries, a further step is to automatically extract branching information of the coronary artery tree. For this purpose, the path starting at the currently processed (start) seed point may terminate either in one of the end seed points or in an existing tracked path generated by previously processed seed points. If a path terminates in another path, the termination point is regarded as a branching point. The extracted branches and their hierarchical information are stored in a special data structure (Fig. 3.7) which will subsequently be used for coronary artery segmentation (Section 3.3) or for labeling the coronary artery tree (Section 3.4). Its basic concept is therefore briefly described. For each branch, the corresponding tracked vessel path is stored. Furthermore, a branch is linked either to its parent branch from where it originates, or it is linked to a root node, when it directly outlets from the ascending aorta. Each branch can have an arbitrary number of children, which are also branches. Speaking from children branches of branch i, we refer to its direct children, *i.e.* branches whose parent is branch i. With the term sub-branches of branch i, we refer to all branches which have – directly or indirectly

via other parents – branch i as parent. For the example in Figure 3.7, sub-branches from branch i are branches j through m whereas children from branch i are only branch j and branch k.

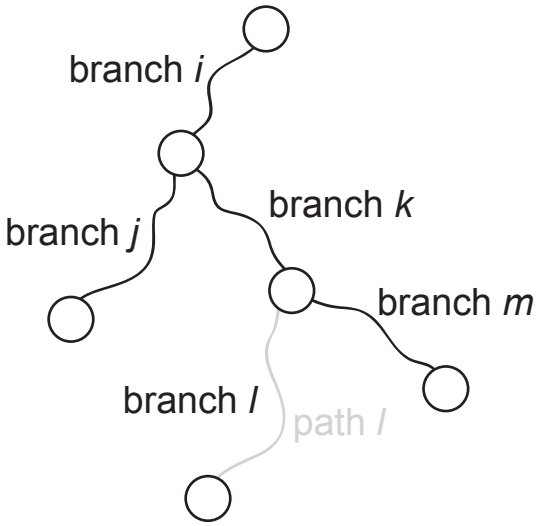

***Figure 3.7**: Data structure used to store the hierarchical branching information of the coronary artery tree.*

3.2.3 Experimental Setup and Results

We successfully applied the described coronary artery tracking method on over 250 CTCA data sets. A detailed performance evaluation was not feasible because no manual tracking of the coronary arteries was available as ground-truth. Figure 3.8 exemplarily shows the tracked coronary artery trees together with the placed seed points for two CTCA data sets.

3.3 Vessel Lumen Segmentation

Besides knowing a path through the coronary arteries, it is also important to segment their whole lumen from the surrounding tissue. This information is vital for the assessment of atherosclerosis. First of all, the lumen can be used as a mask to limit the plaque detection within a CT data set to a certain region. Furthermore, the morphology of the lumen itself can be analyzed. In general, plaques cause a change of the vessel wall, either an outward expansion referred to as *positive remodeling* [Glagov *et al.* 1987, McPherson *et al.* 1991] or a vessel lumen shrinkage, also called *negative remodeling* [Mintz *et al.* 1997, Nishioka *et al.* 1996, Pasterkamp *et al.* 1995].

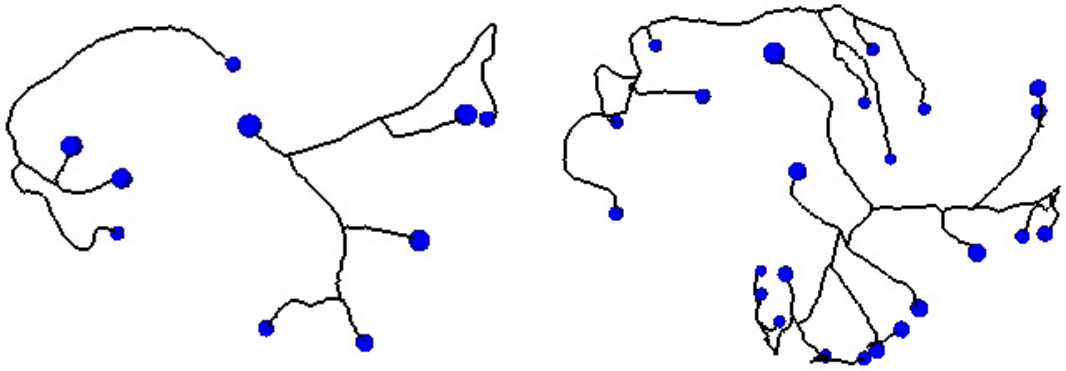

(a) Example 1 *(b)* Example 2

***Figure 3.8**: Exemplary results for tracked coronary arteries with the proposed algorithm. Manually placed seed points are illustrated as spheres.*

The challenges for coronary artery segmentation are comparable to those for the tracking of coronary arteries (Fig. 3.4). Stenoses or motion artifacts may lead to a premature termination of the segmentation process whereas crossing of adjacent structures with similar intensity characteristics may lead to a leakage of the segmentation process into these undesired regions. Therefore, constraints about the tubular anatomical shape of the coronary arteries are often included in the segmentation process.

3.3.1 Related Work

Various segmentation algorithms for vascular structures have been proposed so far. A review of existing approaches was given in 2000 by Pham *et al.* [2000], in 2003 by Bühler *et al.* [2003], and by Kirbas and Quek [2004] in 2004. Since then, many other segmentation algorithms for vascular structures have been reported [Boskamp *et al.* 2004, Bruijns 2001, Florin *et al.* 2006, Friman *et al.* 2008a, Holtzman-Gazit *et al.* 2006, Law and Chung 2007, Li and Yezzi 2007, Peters *et al.* 2008, Socher *et al.* 2008, Wörz and Rohr 2007]. These algorithms are not particularly targeted for the segmentation of coronary arteries but are proposed as vessel segmentation approaches in general. Therefore, there might be a need for some adaptations for these approaches when applied for coronary artery segmentation in cardiac CT images.

Besides the aforementioned vessel segmentation approaches, specialized algorithms for the segmentation of coronary arteries in CT data sets have been proposed. As already

discussed, vessel tracking and vessel segmentation are closely linked to each other such that in most cases, results obtained by tracking algorithms also contain information about the vessel's boundary. This is the case for all approaches presented in Section 3.2.1 for the tracking of coronary arteries. Hence, these approaches can also be regarded as vessel segmentation algorithms as they implicitly or explicitly compute the vessel boundary although their primary target is the tracking of the coronary arteries. In the following, only approaches with a special focus on coronary artery segmentation will be reviewed. Certainly, these approaches might also be applied for vessel tracking by post-processing the resulting segmentation mask with a skeletonization algorithm to obtain a path through the coronary arteries.

Bock *et al.* [2008] used a progressive region growing approach for the segmentation of the coronary arteries. The region growing was combined with a growth front monitoring technique to correct local leakage by retrospective detection and removal of leakage artifacts. While progressively reducing the region growing threshold for the whole image, the growing process was locally analyzed using criteria based on the assumption of tubular, gradually narrowing vessels. Bouraoui *et al.* [2008] segmented the coronary arteries based on mathematical morphology techniques guided by anatomical knowledge. In detail, a morphological hit-and-miss transform was applied to enhance the coronary arteries. A region growing, initialized at automatically detected seed points in the orifices of the coronary arteries, was then run on the morphologically processed image. Van Velsen *et al.* [2007] developed VAMPIRE (Vascular Analysis using Multiscale Paths Inferred from Ridges and Edges) for the segmentation of coronary arteries. VAMPIRE was based on the detection of vessel-like structures by analyzing first-order and second-order image derivatives combined with a minimal cost path algorithm. The image derivatives were obtained using Canny edge detection and an improved ridge filter for detecting elongated structures. Wesarg and Firle [2004] applied their corkscrew algorithm, a skeleton-based approach, for the segmentation of coronary arteries. This semi-automatic extraction techniques required the definition of a start and an end seed point within the vessel. A first estimate of a path through the vessel was then used to compute the boundary, orthogonal to the direction of the course of the coronary arteries. Yang *et al.* [2007] proposed a hybrid approach for the automatic segmentation of coronary arteries using multi-scale vessel filtering and a Bayesian probabilistic approach in a level set image segmentation framework. The initial surface of the coronaries was obtained from the multiscale vessel filter response, and the surface then evolved to capture the exact boundary of the coronaries according to an improved evolution model of implicit surfaces.

3.3.2 Methods

For the segmentation of the coronary arteries, we decided to use a graph-cut approach, because graph-cuts have shown to be robust and only few parameters are needed for their adaption to specific problems.

From the vessel tracking algorithm (Section 3.2), we obtain a path through the coronary arteries as well as branching information, *i.e.* the path of the coronary artery tree is composed of several branches, each representing either a vessel or a part of it. We apply the graph-cut segmentation for each branch individually. For this, we first reformat and straighten the branch along its path into a stack of axial 2D slices. The first slice in the stack represents the most proximal part of the branch. Segmentation with graph-cuts is performed slice-wise in the axial slices, starting from the first to the last slice of the stack. After the segmentation is performed, the result is reformatted back into the original 3D space of the CT data set. The proposed segmentation process will subsequently be discussed in more detail.

Graph-cut

Graph-cuts belong to the graph-based approaches which interpret the given image as a directed or undirected graph $G(V, E)$. Voxels are converted to vertices of V and edges (u, v) contained in E are defined between neighboring voxels u, v according to the given neighborhood relationships in the image. This transform offers the possibility to apply well-established algorithms from graph theory for the extraction of anatomical features.

For graph-cuts, a flow network is defined by assigning weights, or capacities, $c(u, v)$ to the graph edges. Such a flow network usually contains additional nodes that are called sources and sinks, or terminals. Let s be a source that produces flow and t a sink that consumes flow. A flow in G is a real valued function f with the following properties [Cormen *et al.* 2001]:

1. The amount of flow along an edge must not exceed its capacity.
2. The flow from a vertex u to a vertex v is the negative flow in reverse direction.
3. The amount of flow into a node equals the amount of flow out of it.

The dual to the problem of finding the maximum flow in G is to find the cut of G with minimal capacity. The minimum cut of G is a partition of V into two subsets S and $T = V - S$ such that $s \in S$ and $t \in T$ while minimizing the capacity of the cut edges $(u \in S, v \in T)$. Several polynomial time algorithms exist to solve the problem of finding the minimum cut of a graph [Kolmogorov and Zabin 2004, Cormen *et al.* 2001]. Graph-cuts have been adapted for anatomical segmentation problems [Boykov and Jolly 2001, Boykov *et al.* 2001] and since then have been commonly used for the segmentation of anatomies [Ali *et al.* 2007, Boykov and Funka-Lea 2006, Fürnstahl *et al.* 2008].

In order to apply graph-cuts for segmentation tasks, the segmentation step is formulated in terms of energy minimization by describing it as a voxel-labeling problem: the input is a set of voxels and a set of labels. The goal is to find a labeling f (*i.e.*, a mapping from the voxels to the labels) which minimizes some energy function $E(f)$. A standard form of such an energy function [Kolmogorov and Zabin 2004] is

$$E(f) = \sum_{v \in P} D_v(l_v) + \sum_{v,w \in N : l_v \neq l_w} V_{v,w}(l_v, l_w), \tag{3.1}$$

where N is the set of pairs of adjacent voxel. $D_v(l_v)$ is the data cost function that measures the costs for assigning voxel v to label l_v. $V_{v,w}(l_v, l_w)$ measures the costs for assigning voxel v to label l_v and neighbor w to l_w (smoothness costs).

For solving this labeling problem, we used the graph-cut algorithm as proposed by Kolmogorov and Zabih [2004] and implemented by Boykov *et al.* [2001, 2004]. In order to minimize E, they create a specialized graph such that the minimum cut on the graph also – either globally or locally – minimizes $E(f)$.

Costs

For our segmentation task, one of two possible labels has to be assigned to each voxel, namely *obj* when the voxel belongs to the object or *bkg* when it is part of the background.

Data cost. The data term $D_v(l_v)$ evaluates the penalty for assigning a particular voxel v to a certain label l_v. To determine the cost $D_v(obj)$ for labeling a voxel v as *object*, we compute the difference between the mean intensity value $\overline{I}_{obs}$ measured in a $7 \times 7 \times 7$ neighborhood around a point automatically detected in the ascending aorta (Section 3.1) and the intensity value I_v of v. Hence, the data term will be negative for all voxels with intensity values above $\overline{I}_{obs}$ and therefore favors their labeling as *object*. In return, we define the cost $D_v(bkg)$ for the label *background* as the negative value of $D_v(obj)$.

The mean intensity value in the ascending aorta can be regarded as a good approximation for the expected mean in the coronary arteries. Stolzmann *et al.* [2008b] have shown no significant difference between the mean intensity in the ascending aorta and the mean intensity in the proximal parts of RCA and LM, respectively. As more distal branches might have lower intensity values than the proximal portion of the coronary arteries, we multiplied $\overline{I}_{obs}$ with a tolerance factor α which was empirically set to $\alpha = 0.17$. So far, the data costs can be described as

$$D_v(obj) = \left[(1-\alpha)\overline{I}_{obs} - I_v\right] \tag{3.2}$$

$$D_v(bkg) = -D_v(obj). \tag{3.3}$$

Similar to Slabaugh and Unal [2005], we further introduce a shape prior into the data term. Hence, circular structures are favored as vessels in their cross sections are assumed to be circular. For this, the data cost is scaled by the squared ratio between the distance d

of the voxel to the vessel center $\vec{c}$ at the current processed slice and the expected vessel radius r given as a parameter.

This results in an updated expression for the data cost terms

$$D_v(obj) = \left[(1-\alpha)\overline{I}_{obs} - I_v\right]\left(\frac{d}{r}\right)^2 \tag{3.4}$$

$$D_v(bkg) = -D_v(obj) \tag{3.5}$$

Finally, negative costs are set to zero as negative cost values caused some instabilities in the used graph-cut algorithm:

$$D_v(obj) = max(D_v(obj), 0) \tag{3.6}$$

$$D_v(bkg) = max(D_v(bkg), 0). \tag{3.7}$$

Smoothness cost. The smoothness term $V_{v,w}(l_v, l_w)$ evaluates the penalty for assigning neighboring voxels to different labels. In 3D for example, the labeling of a voxel's 26 neighborhood is regarded for the computation of the smoothness term. Using the smoothness term, boundary discontinuities or holes in the segmentation should be avoided. For example, if all of its neighbors are labeled as object voxels, there is a high probability that the regarded voxel also belongs to the object such that a labeling as background should be penalized. However, at the border of objects, adjacent voxels often have very different labels. Therefore, it is important that the selected smoothness cost does not overpenalize such labelings.

For our segmentation, we selected the following smoothness cost which provided a good trade-off between smoothness within the object and reasonable boundaries between object and background.

$$V_{v,w} = \begin{cases} 0 & v = w \\ 10 & v \neq w \end{cases}. \tag{3.8}$$

Implementation details

In order to apply the shape prior, the vessel's center point $\vec{c}_n$ at the currently processed slice n has to be known. However, the chosen vessel tracking method only delivers a path through the vessel and not its centerline. Therefore, we include segmentation results from previous slices to obtain an estimate of $\vec{c}_n$ for the currently processed slice.

For the first slice, the center $\vec{c}_0$ of the vessel is defined as the point obtained by the tracking algorithm in this slice. For subsequent slices, the center of the vessel for slice n is defined as

$$\vec{c}_n = \frac{1}{2}\vec{c}_{n-1} + \frac{1}{2}\vec{c}_{seg} \tag{3.9}$$

where $\vec{c}_{n-1}$ is the center estimate used in the previous slice and $\vec{c}_{seg}$ is the barycenter of the segmented voxels from slice $n-1$.

To adapt for local intensity changes in the branch that might occur through stenoses or other discontinuities, we allow the algorithm to locally adapt $\overline{I}_{obs}$ if otherwise no voxels could be segmented. If this is the case for a current slice, we temporally set $\overline{I}_{obs}$ to the mean intensity of segmented voxels measured in a neighborhood of slices around the current regarded slice. If empty slices occur in a segmentation, the whole segmentation process is re-initialized for a smaller value of the expected radius r. Based on reported anatomical studies for the coronary arteries [Dodge *et al.* 1988, Dodge *et al.* 1992] we initially set $r = 5$ mm. If no segmentation result can be obtained for a slice, r is lowered to 4 mm for a next try and if again no segmentation can be achieved, it is finally lowered to 3 mm.

Besides the shape prior used in the data term, we further apply a hard constraint shape prior, *i.e.* all voxels with a distance $d > r$ away from the center of the vessel at the current regarded slice are regarded as background voxels, independent from their intensity.

Pruning

We observed that the segmentation sometimes includes small side branches or other small structures that do not belong to the regarded branch itself. In order to remove those small structures, we added a pruning post-processing step to the segmentation. The pruning consists of a slice-wise connectivity check on the segmented voxels with the prior that segmented voxels must be connected either to segmented voxels within the current slice (4-neighborhood) or to segmented voxels of the preceding slice. The idea is to apply this connectivity check twice. In the first run, it is started from the first slice of the stack and is applied slice-by-slice until the last slice is reached. Afterwards, the resulting connected and segmented voxels are taken as input and the procedure is repeated, this time, however, from the last to the first slice. Doing so, all small structures will be discarded as they are supposed to be connected from only one direction to the segmentation result (Fig. 3.9).

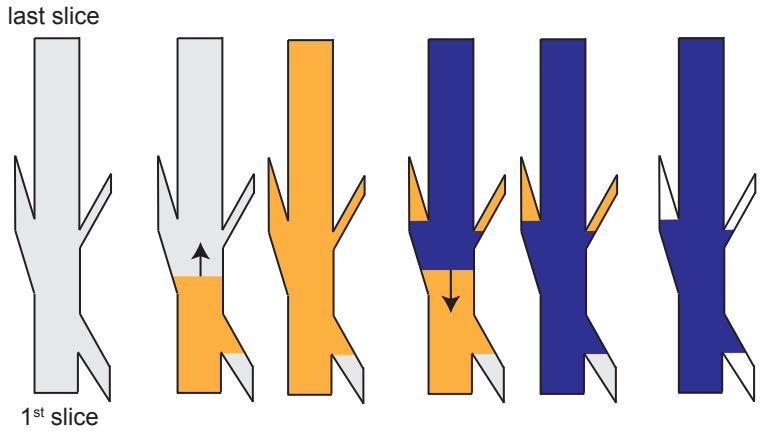

(a) Segmentation. *(b)* Forward run. *(c)* Backward run. *(d)* Result.

***Figure 3.9**: The segmentation result (a) is pruned by applying twice a slice-wise connectivity check. In a forward run (b), it is applied from the first to the last slice in the stack whereas for the backward run (c), it is applied in reverse direction on the results from the preceding step. After both runs, the pruned segmentation (d) is obtained.*

3.3.3 Experimental Setup and Results

We successfully applied the described vessel segmentation method on over 250 CTCA data sets. We evaluated the results by visual inspection and obtained a good agreement when comparing the segmentation results to the given CTCA data sets. Unfortunately, a detailed performance evaluation was not feasible because no manual segmentation of the coronary arteries was available as ground-truth. Figure 3.11 exemplarily shows the segmented coronary artery trees for two CTCA data sets.

3.4 Coronary Artery Tree Labeling

Vessel labeling is the process of assigning an anatomical notation to tracked vessels according to some standardized model. For coronary artery tree labeling, the 16-segment model of the American Heart Association (Section 1.1.3) is commonly used as reference model. The labeling of the coronary arteries according to a standardized model is essential for the reporting of coronary diseases. Without such a labeling, the location of plaques, stenoses or other anomalies cannot be precisely documented. The challenges for automatic algorithms for the labeling of the coronary artery tree are manifold. First, they have to be flexible enough to cover anatomical variations like different dominance patterns (Section 1.1.2) or the anatomical availability of segments as not each segment might

(a) Example 1 *(b)* Example 2

***Figure 3.10**: Exemplary results of the proposed coronary artery segmentation algorithm.*

be present in a patient [Cademartiri *et al.* 2008]. Second, coronary tracking algorithms are not always able to track the whole coronary tree such that parts might be missing. Finally, coronary tracking algorithms can additionally introduce noise to the coronary tree in the form of false branches.

3.4.1 Related Work

Automatic labeling algorithms are not limited to the coronary arteries but were also proposed for other tree-like structures as a geometric tree matching for the labeling of lung structures [Pisupati *et al.* 1996], a machine learning approach for the labeling of bronchial branches [Ota *et al.* 2008] or a model based approach for cerebral vasculature labeling [Hall *et al.* 1997].

For the automatic labeling of coronary arteries, most algorithms have been proposed for classical 2D coronary angiography (CA) images. Similarities in the approaches can be observed namely the definition of an anatomical *model graph* on which the tracked coronary arteries, the *data graph*, are mapped for the labeling by using graph matching techniques. Dumay *et al.* [1994] created a 2D model graph and matched it against the data graph on the basis of a global minimal dissimilarity of features and relationships. Smets *et al.* [1990] proposed a constraint satisfaction approach for the labeling of the left coronary artery.

Other approaches define a 3D model graph and select in a first step a 2D projection of it that best fits to the acquired CA image. This 2D projection is then mapped against

the data graph. Haris *et al.* [1999] used for this purpose a weighted maximal clique on the association graph corresponding to the model graph and data graph. Ezquerra *et al.* [1998] applied a branch-and-bound algorithm – a top-down approach, starting from the root node – for the mapping between model graph and data graph. Chalopin *et al.* [1998, 2001] also proposed a hierarchical approach by first mapping the main artery followed by its sub-branches between the model and data graph using graph matching techniques.

When bi-plane CA is performed, *i.e.* when two images in different image planes are required from the targeted anatomy, additional information arises that can be used for labeling or for a 3D reconstruction of the coronary arteries. Garreau *et al.* [1991] used this information in a knowledge-based approach for the simultaneous 3D reconstruction and labeling of the coronary arteries.

Only a few approaches have been reported so far for the labeling of coronary arteries based on CT data sets.

Lorenz *et al.* [2004b] used a model approach for the automatic labeling of LAD, CX and RCA in CT data sets by automatically mapping tracked coronary centerlines to a manually established model. This mapping was performed in three steps, each adding successively additional degrees of freedom (DOF) to the transformation of the 3D point coordinates of the tracked centerline. In the first step, only translation and rotation was allowed whereas in the second step, an overall scaling was added. Finally, the third step allowed translation, rotation, scaling, and shear. In each step, the parameters were simultaneously optimized in a down-hill simplex optimization procedure. This model approach was successfully tested on 33 CTCA data sets.

Fritz *et al.* [2008] automatically labeled the three main branches (LAD, CX, RCA) in CTCA data sets based on the knowledge of the pose of the aorta and the left ventricle. They used a hierarchical approach and first divided the coronary tree into its left and right branch before the left branch is further sub-divided into the LAD and CX. For each division, a main branching node was searched, *i.e.* a node which cut the tree better into two equally sized sub trees than every other node. Anatomical knowledge was then used to assign the correct label to each branch. The labeling was successfully tested on 10 CTCA data sets.

3.4.2 Methods

In contrast to the aforementioned labeling algorithms for CTCA data that labeled only the coronary artery tree at the vessel level (RCA, LM, LAD, and CX), we propose an automatic labeling of the coronary arteries that additionally labels the RCA into its four possible segments.

Our approach can be regarded as a knowledge-based hierarchical approach. By analyzing coronary artery trees in a small number of CT data sets, we derive anatomical knowledge

like specific branching characteristics and their locations and express this knowledge in the form of algorithmic rules. Although Dodge *et al.* [1988, 1992] have developed a model for the coronary artery tree based on bi-plane CA acquisitions that also included the expected positions of the segments of the coronary tree, we could not benefit from it as the expected positions did not match the observed positions in our available CT data sets.

With the hierarchical approach, we first divide the coronary artery tree into its left and right branch and then successively refine the labeling for each branch separately by labeling more specific vessels or segments following the course of the coronary arteries from their proximal start till their distal end.

Left or right branch of coronary artery tree

For the available CTCA data sets which were acquired following a standard cardiac CT protocol, we observed that – starting from the ostia in the ascending aorta – the right branch of the coronary artery tree develops into negative x-axis direction whereas the left branch develops into positive x-axis direction. We therefore used this obvious finding as a main criterion for the differentiation between left and right branch of the coronary artery tree by regarding the direction of the extracted branches from the coronary artery tracking step.

Thus, for each branch i whose parent is the root element, the barycenter $\vec{b}_i$ of the tracked path (including all its sub-branches) is calculated as well as the direction $\vec{d}_i$ which is defined as $\vec{d}_i = \vec{b}_i - \vec{r}_i$ where $\vec{r}_i$ represents the most proximal path point of branch i. The x-axis component of $\vec{d}_i$ will be denoted as $x_{\vec{d}_i}$ in the following.

Depending on the number of available branches, different criterions are applied for the labeling. If only one branch is present, the labeling decision is made on $x_{\vec{d}_i}$. If it is positive, the branch will be assigned as *left* and otherwise as *right*. When two branches i and j are present, the labeling is only applied if one branch directs into the positive x-axis ($x_{\vec{d}_i} > 0$), whereas the other branch points into the direction of the negative x-axis ($x_{\vec{d}_j} < 0$). If more than two branches are present, which might be the case in the presence of bypasses, the length $l = \|\vec{d}_i\|$ is added as a criterion. If multiple branches have either a negative or positive $x_{\vec{d}_i}$, the one with maximum l is taken as right or left branch, respectively.

After the labeling of the left and/or right branch of the coronary tree, each branch is further processed independently.

Right branch

An important landmark in the right branch is the point where the first marginal branch originates from the RCA. Knowing this point, both segment 1 and 2 as well as the beginning of segment 3 are defined (Section 1.1.3). The first marginal branch has the observed property that, from the branching point, it goes anterior (*i.e.*, in negative y-direction) and its course is close to the surface of the heart. We further observed, while measuring the difference between the z-coordinates of the branching point and the point at the orifice of the right branch, that this difference was always within a certain range. A sub-branch i of the right branch is therefore regarded as candidate for the first marginal branch if

– it's y-direction is negative. The direction is computed by taking the difference between the last and first path point of branch i.
– the difference between the z-coordinates of the point at the orifice of the RCA and the first path point of branch i is smaller than $30\ \mathrm{mm}$.

For each candidate, a score $s = n_{branch} d_{min_{heart}}$ is computed where n_{branch} is the number of its sub-branches and $d_{min_{heart}}$ is the minimum distance of its path to the boundary of the heart. To determine the minimum distance to the heart, a ray is casted for each point of the path in negative x-direction until it reaches the boundary of the heart, defined as a measured intensity value below $-400\ \mathrm{HU}$. The length of the casted ray is then interpreted as the distance to the right heart boundary. With the score s, vessels close to the heart surface with few sub-branches should be favored as the first marginal branch is a small side branch. Therefore, the candidates with the lowest and second lowest scores are determined. If the second smallest measured score is at least 1.5 times larger than the smallest score, the candidate with the smallest score can be clearly defined as the first marginal branch. Otherwise, if two similar candidates are present, the candidate with the smallest path length to the root node of the right branch is taken under the constraint that this path length must be at least $20\ \mathrm{mm}$ to avoid false labelings through other small proximal side branches of the RCA.

After the extraction of the first marginal branch and its branching point, the branches belonging to segment 1 and segment 2 as well as the beginning of segment 3 can be appropriately labeled according to the AHA scheme.

The next important landmark for the labeling of the right branch is the origin of segment 4, the posterior descending artery. If present, the posterior descending artery originates when the course of the RCA is approximately parallel to the xy-plane in the CT data set. After the branching, the posterior descending artery runs towards the apex of the heart (Fig. 3.11(b)).

If the first marginal branch could be detected in the preceding step, we limit the search for segment 4 to sub-branches of segment 3. Otherwise, we search all sub-branches of the right branch. According to the anatomical observations, we define the following three criteria for a branch candidate i

– Branch i must branch towards the apex of the heart in an axial slice, *i.e.* it must originate towards the left when regarding the direction of its parent branch. We therefore compute the normalized cross-product between the direction of branch i at its proximal start and the direction of its parent at its distal end (Fig. 3.11(c)). A minimum z-coordinate value for the cross-product of 0.25 is required.
– The normalized direction of the parent branch at its distal end has to point in positive x-direction with an x-component value of at least 0.30.
– The difference between the z-coordinate of the point at the orifice of the RCA and the first path point of branch i must be larger than 30 mm.

If more than one candidate fits to these criteria, the most proximal one is taken and labeled as segment 4.

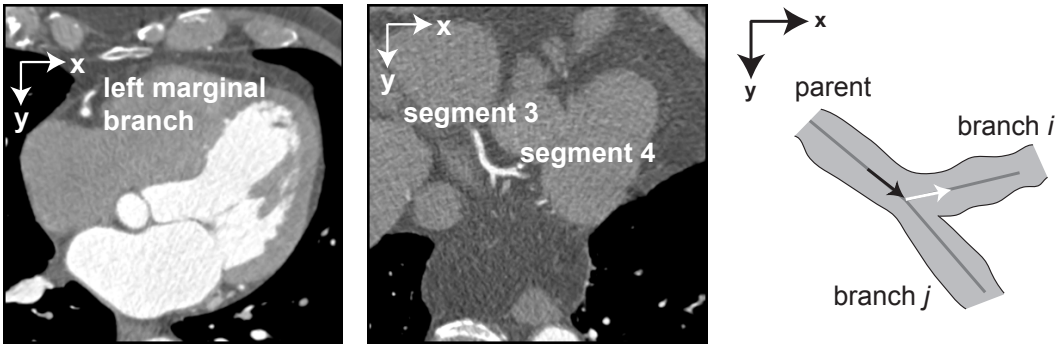

(a) First marginal branch. *(b)* Segment 4 *(c)* Branching direction

***Figure 3.11**: Landmarks needed for the labeling of the right branch, namely the origin of the first marginal branch (a) and the origin of segment 4 (b). The cross-product between the direction of the parent branch at its distal end (black arrow) and the direction of a branch candidate at its proximal beginning (white arrow) is computed to determine the branching direction (c).*

Left branch

The left branch with its origin in the ascending aorta is labeled as the LM artery. The first important landmark in the left branch of the coronary artery tree is the bifurcation of the LM artery into the LAD and CX. In some patients, segment 16 also originates from this branching. For the detection of this landmark, we assume – like [Chalopin *et al.* 2001] – that the LM does not contain any side branches between its root and the origins of LAD and CX. Hence, we have to label the children of the left branch either as LAD or CX and have to deal with the possible presence of segment 16.

The name left anterior descending artery (LAD) already includes information about its geometrical course. It first runs anterior (*i.e.*, in negative y-direction) before it descends

along the surface towards the apex of the heart. On the contrary, the CX runs posterior (*i.e.*, in positive y-direction). This anatomical knowledge is used for the labeling of LAD and CX. In a first step, we compute the barycenter $\vec{b}_{left}$ for the tracked path of the left branch (including all its sub-branches) and compare $\vec{b}_{left}$ with the barycenters of the paths (including sub-branches) from the left branch's children.

The child branch i with the most posterior barycenter $\vec{b}_i$ is labeled as the beginning of the CX, if $\vec{b}_i$ is simultaneously more posterior than $\vec{b}_{left}$. Accordingly, the child branch j with the most anterior barycenter $\vec{b}_j$ – under the constraint that $\vec{b}_j$ is more anterior than $\vec{b}_{left}$ – is labeled as the beginning of LAD. If the left branch has three children, the branch neither labeled as CX nor labeled as LAD is assigned the label segment 16.

Although a further subdivision of the CX and LAD into their segments would be desired, we could not observe clear anatomical branching characteristics that could be transferred into algorithmic rules.

3.4.3 Experimental Setup and Results

We used 10 CTCA data sets for tuning the parameters of the proposed coronary artery labeling algorithm. The performance of the algorithm was then evaluated on 40 additional CTCA data sets. For the evaluation, we first determined if the needed landmarks were anatomically available in the data sets. In a subsequent step, we evaluated if these landmarks have been tracked by the coronary artery tracking algorithm (Section 3.2). Finally, the number of cases where a landmark was available throughout the 40 data sets – *i.e.* it was anatomically present and tracked – was regarded as the achievable optimum (100.0%) for the proposed algorithm.

Throughout all the data sets, the left and right branch were correctly identified (100.0%). In the right branch, the first marginal branch was not observed in three and was not tracked in two data sets, respectively. Out of the possible 35 cases, the labeling algorithm successfully detected the first marginal branch in 34 (97.1%) data sets and could accordingly label segment 1 and segment 2 as well as the beginning of segment 3. Only one false positive labeling (2.9%) was observed for the identification of the first marginal branch.

The next landmark, the bifurcation where segment 4 originates, was anatomically missing in 11 and could not be tracked in two data sets, respectively. Out of the possible 27 cases where this landmark could have been detected, the proposed algorithm correctly labeled it in 17 (63.0%) cases whereas in three (11.1%) data sets no label was assigned and in seven (25.9%) data sets the wrong bifurcation was labeled.

In 38 out of the 40 cases (95.0%), the left branch could be correctly split up into the LM, LAD, and CX artery, respectively.

3.5 Discussion and Conclusion

In this chapter, we have discussed algorithms for the (semi-)automatic extraction of anatomical structures in data sets. Further, we have proposed specific algorithms for the automatic detection of the ascending aorta, the tracking and segmentation of the coronary arteries as well as the automatic labeling of the coronary artery tree. These proposed approaches will be used in the next chapter for the extraction of anatomical structures needed for an assessment of atherosclerosis.

First, we presented a fast and robust algorithm for the automatic detection of the ascending aorta in CTCA data sets by using a two-level threshold ray propagation approach. The method has been successfully evaluated on 297 data sets from different CT devices. A detection rate of 97.0% confirmed the robustness of the presented method. Only 9 false positives were counted where the largest candidate cluster – assumed to be the ascending aorta – did not represent the ascending aorta. In these cases, the second largest cluster would have been the correct choice. Hence, future work should concentrate on the definition of additional features for the two largest clusters to further improve the detection rate. We see two possible application areas for the proposed automatic ascending aorta detection. First of all, the method can be used to automate coronary artery tracking and segmentation algorithms that still need an initialization through a seed point within the ascending aorta like the approaches presented by Bock *et al.* [2008], Hennemuth *et al.* [2005], and Merges *et al.* [2006]. Further, the algorithm can be used to automatically extract intensity information from the ascending aorta which is a good estimate for the intensity characteristics in the proximal parts of the coronary arteries [Stolzmann *et al.* 2008b].

The proposed approaches for coronary artery tracking and segmentation performed well. However, at this point, it must be stated that the focus of this thesis is not the development and research of coronary artery tracking or segmentation algorithms, respectively. Therefore, a detailed evaluation of these proposed methods against ground-truth data is missing and their correctness was only assessed by visual assessment. Further, the proposed methods still show potential for optimization and further improvements.

The automatic labeling of the coronary arteries was evaluated on 40 CTCA data sets where an excellent performance on the vessel level could be achieved – similar to the results from Lorenz *et al.* [2004b] and Fritz *et al.* [2008]. By using a knowledge-based hierarchical approach, we were further able to label the RCA according to its four segments. The first three segments could be assigned in a robust way whereas segment 4 could not be reliably labeled. A reason for this might be the small number of 10 training data sets from which the anatomical knowledge was extracted. Hence, some anatomical variations that predominantly occur in the distal parts of the coronary artery tree could not be covered. Although desired, a segment-wise labeling of the CX and LAD was not possible as no meaningful anatomical criterions could be derived from the training data.

Nevertheless, the proposed algorithm is a further step towards a fully automatic labeling of the coronary artery tree. Several applications might benefit from a labeled coronary artery tree. First of all, a labeling allows the automatic creation of reports about detected locations of atherosclerosis. Further, segment or vessel specific knowledge – like spatial distribution patterns of plaques – can be incorporated into the process for the assessment of atherosclerosis.

4

Automatic Detection of Calcified Coronary Plaques

Besides calcium scoring, which is done on non-enhanced images for a first risk assessment of coronary diseases, the plaques are also assessed in contrast-enhanced images to diagnose stenoses or other anomalies. To date, no commercial software package exists to perform automated plaque segmentation and plaque diagnosing [Cademartiri *et al.* 2006]. Although semi-automatic software tools have been developed to support the detection of coronary plaques, the process is still time-consuming, error-prone and shows inter- and intra-observer variabilities [Hoffmann *et al.* 2008].

The aim of this work was to develop a framework for the automatic detection of calcified coronary plaques. This is achieved by incorporating both the contrast-enhanced and non-enhanced examinations such that more information for each plaque is available – for its detection and potential subsequent assessment.

After a motivation of the proposed approach and a review of existing methods for plaque detection, the framework for the automatic detection of calcified coronary plaques will be presented. Finally, the chapter closes with an evaluation and discussion of the proposed framework for automatic detection of calcified coronary plaques.

4.1 Introduction

In general, both a native (*i.e.*, non-enhanced) and angio (*i.e.*, contrast-enhanced) examination are performed for the assessment of coronary artery diseases [Schwarz *et al.* 2008]. The native examination is used in calcium scoring for a first risk assessment. The angio examination, however, nicely visualizes the vessel lumen and as such allows to assess the degree of a stenosis.

Previously reported approaches for calcified coronary plaque detection, presented in the subsequent section, only use one of the two available examinations for their assessment

of plaques, although an additional examination would be available without any extra radiation exposure for the patient.

The key idea of the framework presented herein is to use both the angio and the native examination for an automatic detection of calcified coronary plaques. For this, plaque candidates are extracted from both examinations. The candidates are then used to co-register the two data sets. Hence, more information is available for each plaque to suppress false positives and to enhance the detection rate.

4.1.1 Related Work

For the detection of coronary plaques, it is helpful to delineate the coronary arteries, *i.e.* determining the centerline or a segmentation of the vessel lumen as presented in the preceding chapter. With the various branches of the coronary artery tree tracked and segmented, it is possible to analyze each branch for the presence of plaques.

Toumoulin *et al.* [2003] used a level set approach to detect both the inner and outer wall of a vessel in CT data sets and were therefore able to identify calcified plaques. Rinck *et al.* [2006] also computed the inner and outer vessel wall to assess atherosclerotic plaques in coronary arteries using shape-based segmentation. Their algorithm, however, had to be manually initialized with a seed point before and after each plaque. A *Plaque Map* for CT images that uses color-based isometric lines and a bird's eye view to support the plaque detection was introduced by Komatsu *et al.* [2005]. This method is only a visual aid for the manual detection of plaques. A model-based approach to semi-automatically measure the degree of stenosis in carotid arteries was developed by Frangi *et al.* [2000] for MR images. Adame *et al.* [2004] combined model-based segmentation and fuzzy clustering to detect the vessel wall, lumen and lipid core boundaries in MR images. Also for MR images, Sun *et al.* [2008a] used a Fuzzy C-Means based clustering algorithm to characterize plaque constituents. Wesarg *et al.* [2006] presented preliminary results on 10 patients for the automatic detection of calcified plaques by combining diameter information from the segmented vessel with an intensity value analysis within the coronary arteries. Teßmann *et al.* [2008] recently proposed a framework for reliable automatic detection of stenotic lesions in CTCA data by using a learning-based detection approach. By applying a specialized feature extraction method based on a sampling pattern that approximates the vessel shape, a classifier could be trained with the AdaBoost algorithm [Freund and Schapire 1995], that finally detected 45 out of 57 (78.9%) calcifications.

With two exceptions, all aforementioned methods require substantial user intervention. Only the approaches from Wesarg and Teßmann detected calcified plaques automatically when the tracked coronary tree was given as input.

All aforementioned approaches aimed for the plaque detection in angio data sets. Besides these works, some fully automatic detection algorithms for the detection of calcified

coronary plaques in native examinations have been proposed for the purpose of calcium scoring.

Ukai *et al.* [1995] first proposed a method for coronary calcification detection in native CT examinations using diagnostic rules. Later on, they improved their method by applying a neural network based classification method to discriminate between coronary calcifications and artifacts [Ukai *et al.* 1998]. Išgum *et al.* proposed a k-NN classifier for the automatic detection of calcified plaques in native CT examinations. Originally, the method was developed for the aorta in abdominal CT examinations [Išgum *et al.* 2003] before it was adapted for calcified plaque detection in coronary arteries [Išgum *et al.* 2004, Išgum *et al.* 2005, Išgum *et al.* 2007]. For coronary plaques, an automatic heart and aorta segmentation was applied before specific features were computed and used to automatically detect coronary calcifications using a two-stage classification system with a k-NN classifier and a feature selection scheme. With this approach, Išgum *et al.* could detect 73.8% of the calcified plaques at an expense of an average of 0.1 false positives per data set. Brunner *et al.* [2008] use unsupervised classification to discriminate arterial calcified plaques from non-arterial lesions. The proposed method first mines the characteristics of calcified lesions using an optimization criterion and then identifies a subset of lesion features which is optimal for classification. Second, a two stage clustering is deployed to discriminate between arterial and non-arterial lesions. Experimental results indicated an average accuracy of approximately 80% on 205 non-enhanced EBCT data sets. By using a supervised hierarchical classification, Kurkure *et al.* [2008b] achieved an accuracy of 98.0 % on the same data sets used by Brunner *et al.* [2008]. At each level of the hierarchy, their approach learns an ensemble of classifiers where each classifier is a cost-sensitive learner trained on a distinct asymmetrically sampled data subset.

4.2 Methods

This section presents our framework for the automatic detection of coronary calcified plaques. Plaques are detected in an angio data set while incorporating knowledge from the corresponding native data set. As in general both the angio and native CT examinations are acquired for the assessment of atherosclerosis [Schwarz *et al.* 2008], no additional scan is required for the application of the proposed method. The basic concept, illustrated in Figure 4.1, can be summarized as follows. In the pre-processing steps (A)+(B) the aorta is detected, its intensity statistics are calculated and used to segment the coronary tree using the algorithms presented in the preceding chapter. The third step (C) extracts putative plaque candidates using an intensity-based threshold. This may result in many false positives (FP) due to noise, inhomogeneous contrast agent distribution and CT artifacts. In step (D) the plaques in the angio data set are rigidly registered to the native plaques. The last two steps (E)+(F) use a rule based approach to maximize the number of detected plaques while minimizing FP by introducing a distance and intensity check,

respectively. Throughout the processing pipeline, four sets are used to represent the actual state of the detection process: (1) $\mathcal{A}$ contains the unverified angio plaque candidates, (2) $\mathcal{N}_{130}$ the unverified native plaque candidates, (3) $\mathcal{N}_{200} \subset \mathcal{N}_{130}$ is a subset of $\mathcal{N}_{130}$ and contains the highly calcified but still unverified plaques only and (4) the initially empty set $\mathcal{V}$ contains the verified plaques.

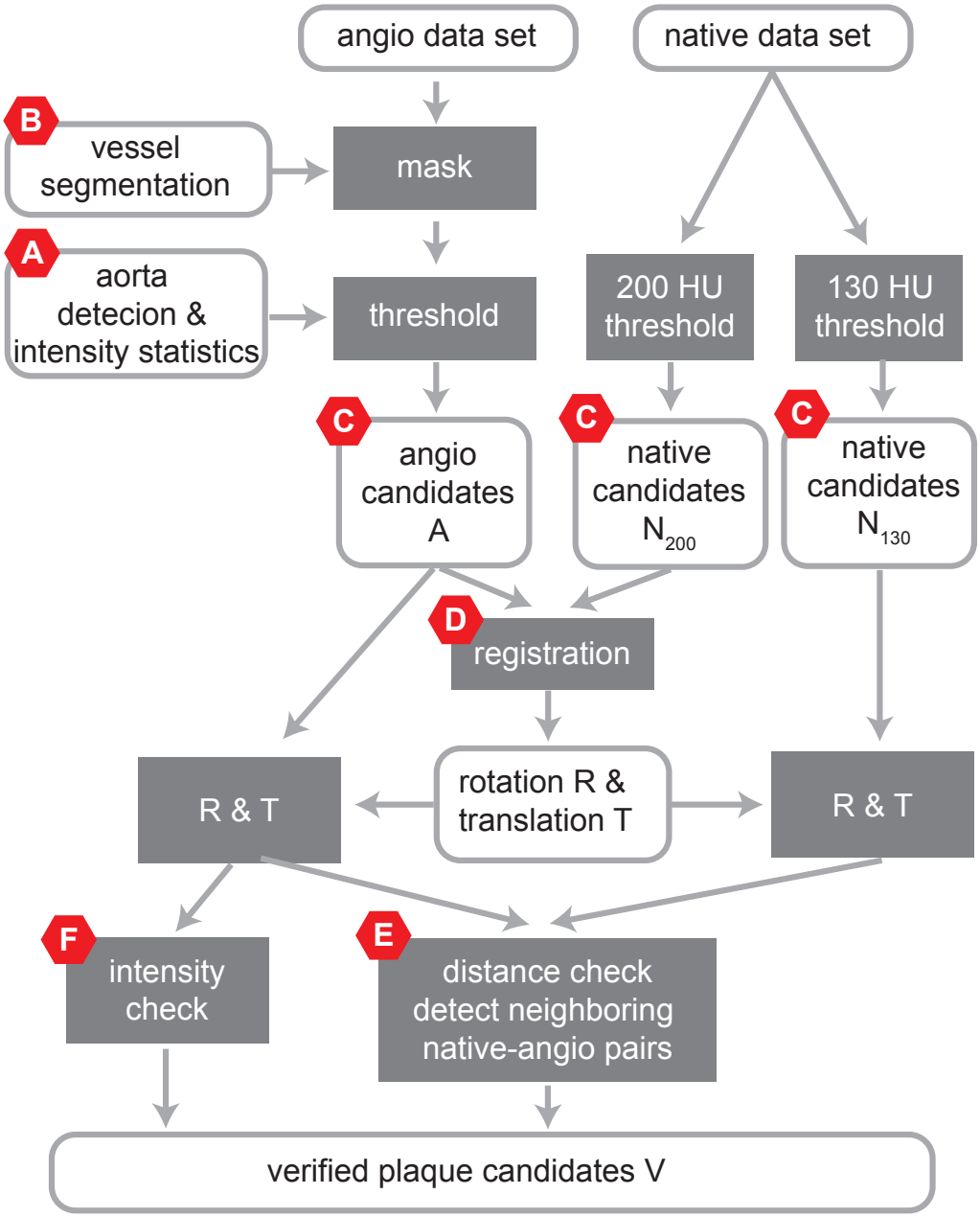

***Figure 4.1**: Workflow of the plaque detection framework.*

(A) Aorta detection.

A point $\vec{p}_{\text{aorta}}$ in the ascending aorta is automatically detected in the angio data set (Section 3.1) and the voxels in a $7 \times 7 \times 7$ neighborhood around $\vec{p}_{\text{aorta}}$ are used to compute the mean Hounsfield intensity μ and standard deviation σ of the contrast enhanced blood. These parameters are then later used to automatically select the threshold for the plaque candidate extraction in the angio data set. The measured μ in the ascending aorta can be regarded as a good approximation for the expected mean intensity in the coronary arteries, as Stolzmann *et al.* [2008b] have shown no significant difference between the mean intensity in the ascending aorta and the mean intensity in the proximal parts of RCA and LM, respectively.

(B) Coronary artery tree.

The coronary artery tree is tracked by the live-wire approach with its intensity and gradient features as presented in Section 3.2. Afterwards, the vessel lumen is segmented by applying a graph-cut with a shape-prior as proposed in Section 3.3. The resulting coronary artery segmentation will then be used as a mask for the candidate extraction step.

(C) Candidate extraction.

Plaque candidates are extracted using an intensity threshold from both the angio and the native data set.

Angio data set. The coronary artery segmentation of the previous step is used as a mask to restrict the plaque candidates to only those within the coronary arteries. The subsequent marching cube algorithm [Lorensen and Cline 1987] then generates meshes of all putative plaques. The iso-surface value $(\mu + 5\sigma)$ is adaptively chosen according to the contrast agent density observed in the aorta (step (A)). Each connected mesh is regarded as an angio plaque candidate a_i which is stored in list $\mathcal{A}$. Each candidate a_i is additionally assigned an intensity score s depending on its 90%-quantile intensity I of its voxels and defined by

$$s = \begin{cases} 0 & : \quad I < \mu + 2\sigma \\ \log_{10}\left(9\frac{I-(\mu+2\sigma)}{500\text{ HU}-(\mu+2\sigma)} + 1\right) & : \quad \mu + 2\sigma \leq I < 500\text{ HU} \\ 1 & : \quad I > 500\text{ HU} \end{cases}$$

The 90%-quantile for the intensity I was chosen to avoid outliers stemming from CT artifacts. The intensity score is defined for values $I \geq \mu + 2\sigma$ to potentially include extremely weak calcified plaques. However, those are currently not extracted and processed in the proposed framework.

Native data set. A radiation absorption intensity threshold of $th_i = 130$ HU – the standard threshold for calcium scoring (see Chapter 2) – is applied to the native data set. To remove most of the bones, connected components larger than 5000 mm^3 are discarded. The resulting binary image is used as a mask for the native data set and the meshes of all plaques with an iso-surface value of 130 HU are then extracted using again the marching cube algorithm. Each connected mesh is regarded as a native plaque candidate n_i and is stored in the list $\mathcal{N}_{130}$. The same procedure is repeated but with $th_i = 200$ HU, to generate a set of higher calcified native candidates called $\mathcal{N}_{200}$.

(D) Plaque registration.

Although the native and angio data sets are acquired consecutively, they are generally not well registered due to the beating heart, breathing and minor patient movement. It is therefore the aim of the rigid plaque registration to determine the rotation $\vec{R}$ and translation $\vec{T}$ between both data sets. This registration allows to take over the coronary segmentation results from the angio to the native data set such that the native candidates can also be limited to the segmented vessel regions. Furthermore, it enables us to compare plaque features from both data sets with each other. To avoid misregistrations, only the very high calcified native plaques of $\mathcal{N}_{200}$ as well as the angio plaques with a score $s > 0.95$ and a volume $v > 5$ voxels are considered for registration. Due to the different scan resolutions the shape between corresponding angio and native candidates may differ, only the barycenters of their meshes are used during the two stage registration process. These barycenters are stored in the list $\mathcal{R}_{\mathrm{N}}$ for the native and $\mathcal{R}_{\mathrm{A}}$ for the angio candidates, respectively. Misregistrations might occur if a large plaque in the low resolution native data set in fact consists of multiple smaller plaques in the angio data set. To resolve this ambiguity, additional points are added to $\mathcal{R}_{\mathrm{N}}$ by sampling all native plaques with an extension greater than 4 mm. Starting from the barycenter, additional points are placed with a step width of $\Delta = 2$ mm in both directions along the plaque's main axis as long as they are situated within the plaque (Fig. 4.2a).

In the first stage of the rigid registration, an optimal translation $\vec{t}^*$ is searched. The rotation is disregarded in this phase as according to our experience it has only a minor impact on the final registration. The optimal translation $\vec{t}^*$ is obtained by first choosing an arbitrary point from $\mathcal{R}_{\mathrm{A}}$ as a reference a_{ref}. Then, for each point $p_n \in \mathcal{R}_{\mathrm{N}}$, the translation $\vec{t} = \vec{p}_n - \vec{a}_{\mathrm{ref}}$ is computed (Fig. 4.2b) and applied to $\mathcal{R}_{\mathrm{A}}$ resulting in $\mathcal{R}_{\mathrm{A}'}$ (Fig. 4.2c). Correspondences between angio and native candidates are established by mapping each transformed $p_{a'_i} \in \mathcal{R}_{\mathrm{A}'}$ to the point $p_{n_i} \in \mathcal{R}_{\mathrm{N}}$ with the smallest euclidean distance (Fig. 4.2c). Afterwards, the energy $E_{p_n} = E_1 + E_2 + E_3$ is computed. The first energy term $E_1 = \|\vec{t}\|$ accounts for the length of $\vec{t}$ which should be minimal as only a small heart motion between the angio and native data set is expected. The second term $E_2 = \sum_i \|\vec{p}_{a'_i} - \vec{p}_{n_i}\|$ considers the remaining distance between the angio and native barycenters of corresponding candidate pairs. The third energy term E_3 compares how

similar the spatial distribution of the angio candidates is with the spatial distribution of the mapped native candidates. For this, the distance $e_{a_{ij}} = \|\vec{p}_{a_i} - \vec{p}_{a_j}\|$ of any possible combination of two different points $p_{a_i}, p_{a_j} \in \mathcal{R}_\mathrm{A}$, $i \neq j$ is compared with the distance $e_{n_{ij}} = \|\vec{p}_{n_i} - \vec{p}_{n_j}\|$ of the corresponding mapped native candidates. The energy E_3 is then defined as $E_3 = \frac{1}{n} \sum |e_{a_{ij}} - e_{n_{ij}}|$ where n is the total number of possible combinations.

In the second stage, the known mapping of angio-native pairs with the minimum energy E_{p_n} is taken to compute the final registration parameters $\vec{R}$ and $\vec{T}$, using the algorithm from Horn [1987] which requires at least three point pairs. For fewer pairs, $\vec{R}$ is assumed to be the unity matrix. $\vec{T}$ is set to $\frac{1}{2}\left((\vec{p}_{a_1} - \vec{p}_{n_1}) + (\vec{p}_{a_2} - \vec{p}_{n_2})\right)$ for two, to $\vec{p}_{a_1} - \vec{p}_{n_1}$ for one, and to the null vector if no plaque pair is present. The rotation $\vec{R}$ and translation $\vec{T}$ are then applied to all native candidates from $\mathcal{N}_{130}$. Those falling outside of the vessel boundaries after the registration are discarded. All matched angio-native candidate pairs are added to $\mathcal{V}$ and removed from $\mathcal{A}$ and $\mathcal{N}_{130}$, respectively.

(E) Distance rule.

Several distance checks are applied to confirm the verified candidates resulting from the registration process and to search for additional pairs that were not considered by the registration process due to their low intensity. Outliers in the registration can occur if a plaque is visible in the angio data set but not in the native acquisition. Then, the corresponding plaque is mapped to a wrong – in general more distant – candidate. Therefore, all previously verified angio-native candidate pairs in $\mathcal{V}$ are re-evaluated. If the distance between the angio and native plaque is larger than 0.5 mm, the candidate pair is removed from $\mathcal{V}$ and put back to $\mathcal{A}$ or $\mathcal{N}_{130}$, respectively. Additional angio-native candidate pairs are detected by iterating through $\mathcal{A}$ and checking for each angio candidate a_i if there is a native plaque n_i within a distance of 0.5 mm. If yes, this pair is added to $\mathcal{V}$ and removed from $\mathcal{A}$ and $\mathcal{N}_{130}$.

(F) Intensity score rule.

This rule considers the fact that large angio plaque candidates with high intensity values are very likely to be plaques even though a corresponding native candidate is missing. An angio candidate is added to $\mathcal{V}$ and removed from $\mathcal{A}$ if its volume is larger than 1 mm^3 and $s \geq 0.75$.

4.3 Experimental Setup and Results

The proposed framework was evaluated on 127 patients (81 males, 46 females, mean age 63.8±12.0, range 35-88). To guarantee robustness, only the first 20 patients were

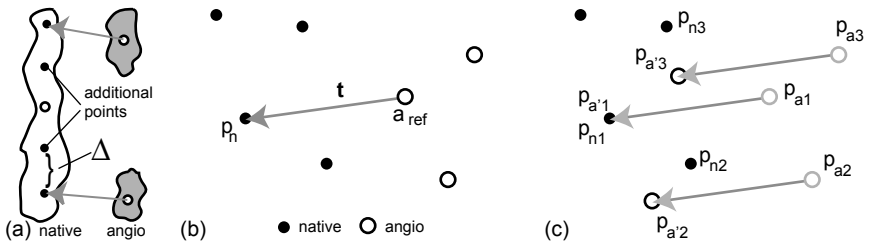

***Figure 4.2**: Plaque registration. Additional points are added for large native plaque candidates (a). Reference point a_{ref} and translation vector $\vec{t}$ (b). Translation and mapping of angio candidates $p_{a'_i}$ to closest native candidates p_{n_i} (c).*

used for development and parameter selection. Both angio and native examinations were acquired on a Dual-Source CT scanner (Somatom Definition, Siemens Medical Solutions, Forchheim, Germany) with standard protocols (as discussed in Table 1.2). The in-plane resolution ranged from $0.25 - 0.73$ mm (512×512 voxels). The slice thickness/slice spacing was $0.75 - 1$ mm/$0.4 - 1$ mm for the angio and 3 mm/$1.5 - 3$ mm for the native data sets. The number of slices varied between 115 and 392 for the angio and between 26 and 101 for the native acquisitions, respectively.

The ground truth was obtained by manual plaque segmentation by an experienced radiologist. The type of plaque (calcified or mixed), the degree of stenosis and the proximal and distal end position of each plaque were determined. A plaque with a stenosis greater than 50% was regarded as obstructive which was observed for 54 plaques (41 calcified, 13 mixed). In total 649 calcified and 102 mixed plaques were labeled in the 127 patients. Figure 4.3(a) shows the allocation of these plaques over the patients. Besides the 33 cases with no plaques, most patients had between one and eight plaques.

The verified plaque candidates from $\mathcal{V}$ were compared with the ground truth data to determine the number of true (TP) and false positives (FP). The number of detected labeled plaques as well as the positive predictive value $PPV = TP/(FP + TP)$ after each processing step are summarized in Table 4.1. The framework detected 86.3% of the calcified and 80.4% of the mixed plaques which leads to a total detection rate of 85.5% with a PPV of 87.8%. In total 109 (89 calcified, 20 mixed) plaques were missed. The mean extension $\bar{d}_e$ of the missed calcified and mixed plaques was 1.3 mm and 4.9 mm, respectively. One small obstructive calcified ($\mathrm{d_e} = 1.2$ mm) and one obstructive mixed plaque ($\mathrm{d_e} = 3.4$ mm) were not detected, resulting in a detection rate of 96% for the hazardous obstructive plaques. The extent of mixed plaques includes both the lipid and calcified part. Therefore, those missed plaques appear larger although only the small calcified part could not be detected. Figure 4.4 shows the plaque candidates at selected stages of the proposed framework for a patient.

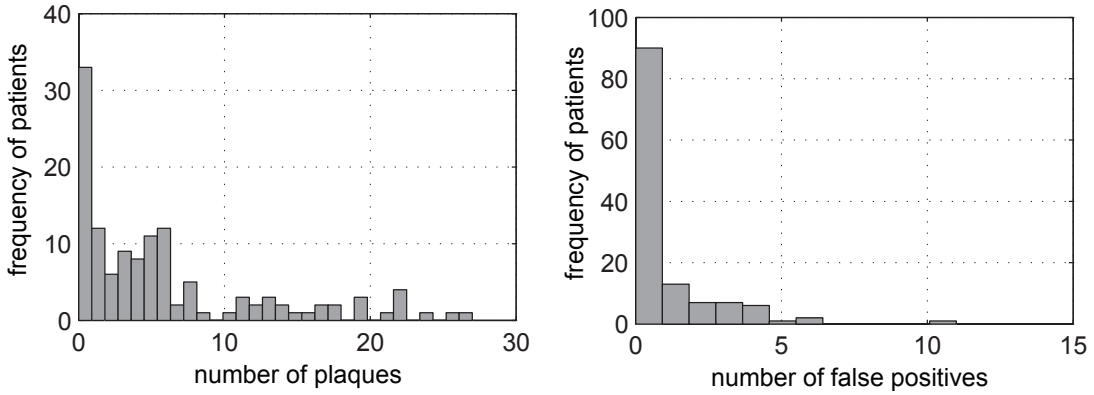

(a) Plaque distribution. *(b)* False positive distribution.

***Figure 4.3**: Histogram showing the distribution of the number of plaques per patient (a) and the distribution of false positives (b).*

4.4 Discussion and Conclusion

We presented a framework for the automatic detection of calcified coronary plaques. Through the proposed novel integration of both the native and the angio data sets into the detection process, we were able to achieve a good detection rate of 85.5%. Although our detection rate was better than the rate of 78.9 % achieved by Teßmann *et al.* [2008] for the detection of calcified coronary plaques in angio data sets, we must state, that our approach had a higher average number of 0.79 FP per patient. We assume that the detection rate from Teßmann *et al.* [2008] would therefore improve if a comparable number of FP would be allowed. On only 10 patients, Wesarg *et al.* [2006] achieved a detection rate of 98% for coronary calcifications. However, due to the very small number of patients and missing information if these data sets were also used for the development of the algorithm, the achieved detection ratio thus has to be considered as a preliminary result, that still has to be verified on a larger data set.

The existing automatic algorithms [Brunner *et al.* 2008, Išgum *et al.* 2007, Kurkure *et al.* 2008b, Ukai *et al.* 1995] that solely detect calcified coronary plaques in native images have a detection rate between 73.8% and 98.0%. However, a direct comparison of our results to these methods would not be feasible because they only detect the calcified coronary plaques in native examinations for the purpose of calcium scoring, whereas our presented framework identifies the plaques in both the native and angio data set by establishing correspondences among them. Through this it is possible to provide detailed information, *i.e.* both the calcium score and the degree of stenosis for each plaque individually.

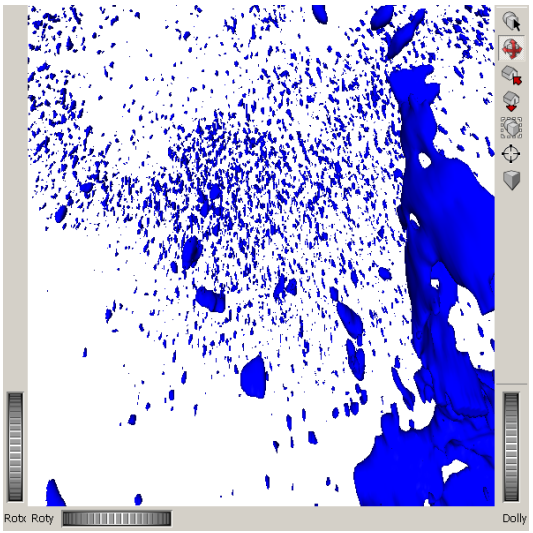

(a) Native candidates.

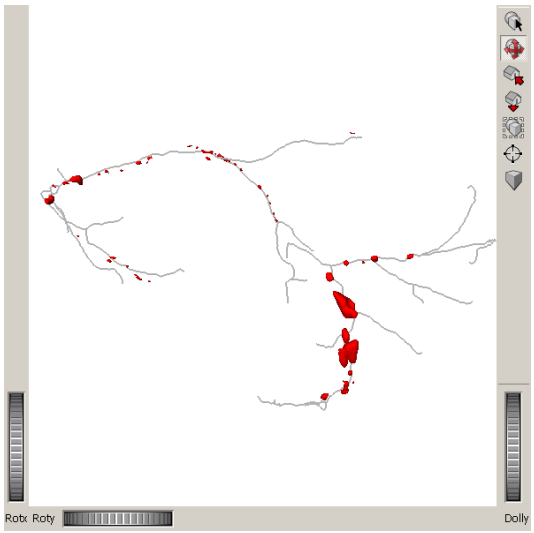

(b) Angio candidates with tracked coronary artery tree.

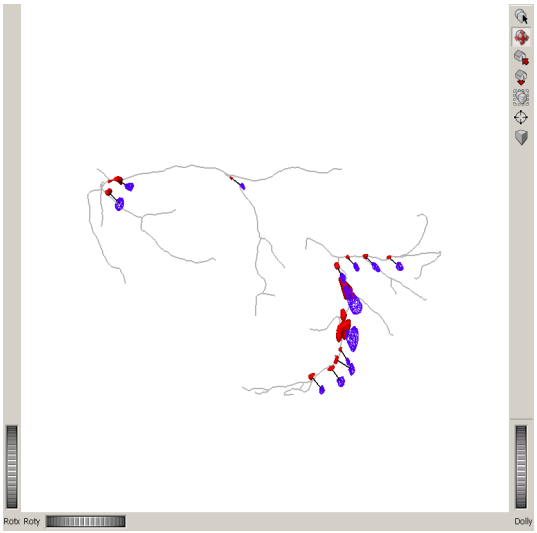

(c) Registered plaques.

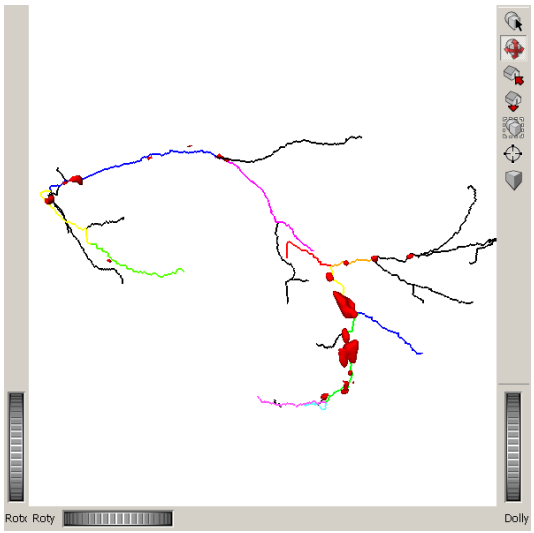

(d) Detected coronary plaques (registered native plaques are omitted for clarity) with automatically labeled coroanry artery tree.

***Figure 4.4**: For the proposed automatic detection of calcified coronary plaques, plaque candidates are extracted both from the native (a) and angio (b) examination. After the registration of highly calcified plaque candidates (c), information from both examinations can be used to detect coronary plaques in the angio examination (d).*

***Table 4.1**: Number (percentage) of detected calcified and mixed plaques as well as the number of true (TP) and false (FP) positives, and the positive predictive value (PPV) for the candidates of the detection framework after each processing step. Some larger plaques are represented by multiple smaller candidates such that the number of TP and detected plaques is not identical.*

		expert	candidate extraction	plaque registration	distance rule	intensity score rule
plaques	calcified	649	594 (91.5%)	436 (67.2%)	497 (76.6%)	560 (86.3%)
	mixed	102	85 (83.3%)	66 (64.7%)	75 (73.5%)	82 (80.4%)
candidates	TP	751	760	544	644	723
	FP	0	699	50	59	100
	PPV	100.0%	52.1%	91.6%	91.6%	87.8%

An analysis of the FP has shown that they accumulate only in a small number of 37 patients (Fig 4.3(b)) where they mostly arose due to an inhomogeneous contrast agent distribution within the distal part of the right coronary artery. The missed plaques were generally small and with two exceptions non-obstructive. In general, those small plaques did not have a major impact on the diagnoses as a physician mainly looks for stenotic or large plaques.

Although, many plaques could be detected by applying an intensity-based threshold, this would result in a high number of FP. Therefore, we added additional steps to verify the extracted plaque candidates. The registration step alone significantly reduced the number of FP. This is obvious as for this step, only highly calcified plaques were considered and the weakly calcified ones were only included in a later stage of the framework. This also explains the decreased detection rate of the registration step as compared to the previous step. Additional criterions for the evaluation of the remaining weaker calcified plaque candidates could considerably improve the detection rate, nevertheless eventually at the expense of an increased FP rate.

The good performance of the proposed approach can be mainly attributed to the fusion of the native and angio data set. This allowed us to carry over the segmented vessels into the native data set and therefore to reduce the FP rate. Moreover, weakly calcified plaques, hardly discriminable from the contrast agent in the angio data set, could be detected. The approach still offers a wide range of possible improvements that can be easily integrated due to its modular design. For example, it might be thinkable to replace the intensity-based plaque detection method by using the classification approach proposed by Teßmann *et al.* [2008]. Towards a computer aided diagnostic tool for the assessment of

atherosclerosis, lipid plaque components also have to be detected and assessed, *i.e.* detected calcified plaques must be classified as purely calcified (hard) plaques or as mixed plaques surrounded by lipid parts. Further, purely lipid (soft) plaques have to be detected by a suitable approach. Therefore, the subsequent chapter is devoted to the assessment of lipid constituents in coronary arteries.

5

Assessment of Lipid Plaque Constituents

Although computed tomography examinations are well suited for the automatic detection of calcified plaques, the same cannot be said for the assessment of lipid plaque constituents. A moderate contrast between lipid and surrounding tissues normally hinders even proper manual assessment. One reason for this poor contrast is that with commonly used single source computed tomography systems different materials can show very similar attenuation at any selected radiation energy. The recently introduced dual energy CT system, however, simultaneously measures attenuations at two energies and therefore shows promise to improve the differentiation of tissues to some extent.

The aim of this work was therefore to evaluate this dual energy CT technology with respect to its performance in improving the contrast between the tissues targeted for an assessment of lipid plaque constituents in particular and for an assessment of atherosclerosis in general, namely a vessel lumen filled with contrast agent, tissue, lipid, and calcium.

This chapter first discusses problems for the identification of lipid plaque constituents in CT data sets and furthermore introduces the dual energy technique with potential approaches for the processing of its data. Afterwards, a suitable approach will be selected, described and evaluated on clinical dual energy data sets for its feasibility to improve the assessment of lipid plaques. A final discussion of the results and of potential steps towards an automatic assessment of lipid plaque constituents concludes this chapter.

5.1 Introduction

CT acquisitions are well suited for the detection of calcified plaques [Achenbach *et al.* 2004, Leber *et al.* 2004, Leber *et al.* 2006, Motoyama *et al.* 2007b] which is expressed by both a good *sensitivity* and *specificity*. However, the same cannot be said for the detection of fibrous and lipid plaques.

The sensitivity expresses the proportion of true positives that are correctly identified as such whereas the specificity expresses the proportion of correctly identified true negatives [Altman and Bland 1994]. The two existing studies using a 16-slice CT system reported a sensitivity of 78% [Achenbach *et al.* 2004, Leber *et al.* 2004] to detect fibrous plaques, and a sensitivity of 53% [Achenbach *et al.* 2004] and 78% [Leber *et al.* 2004] to detect lipid plaques. For comparison, the sensitivity for calcified plaques was >90% in both studies. A better temporal and spatial resolution of recent 64-slice CT systems led to an improvement of the sensitivity to 100% and 94% for fibrous and 79% and 83% for lipid plaques, respectively [Motoyama *et al.* 2007b, Leber *et al.* 2006]. However, it must be noted that all aforementioned studies used IVUS as ground truth reference which itself has a limited sensitivity of 50-70% [Leber *et al.* 2006] for lipid pool detection. Hence, it has to be assumed that the true accuracy of 64-slice CT to detect lipid constituents is significantly lower than observed and reported in the studies.

Although several algorithms for the assessment of lipid tissues in MRI [Adame *et al.* 2004, Anderson *et al.* 2007, Auer *et al.* 2006, Kerwin *et al.* 2001, Sun *et al.* 2008c] and IVUS [Katouzian *et al.* 2008, Nair *et al.* 2001, Nair *et al.* 2004, Pujol *et al.* 2004] image data have been proposed, only two algorithmic approaches have been reported for CT images. Renard and Yang [2008] used geometrical measures on the coronary artery to indicate plaque locations. In a first step, they extracted the centerline as well as the vessel lumen and vessel wall. Thereafter, they assessed soft plaques by examining the difference between the effective cross-section area of the wall and the lumen. However, no clear criterion has been given to conclude the presence of a soft plaque out of the measured difference which, in some cases, showed a very similar characteristic both in healthy vessel areas and in diseased ones. Teßmann *et al.* [2008] applied a learning-based approach for the detection of stenotic lesions in coronary CT data. With this method, they achieved a good detection rate of 90.9% for stenotic soft plaques. Given the centerline of the coronary artery, various features are automatically extracted in a pre-defined surrounding of the centerline. Based on learned samples, a classifier then makes the decision for the presence of a stenotic soft plaque. Although this approach by Teßmann *et al.* [2008] looks promising, it has to be verified if it is also suitable for the detection of non-stenotic soft plaques.

One reason for the bad performance of CT for the detection of lipid tissues in the coronary arteries might be the limited differentiability of the targeted tissue from its surrounding in the image data. Although the measured X-ray attenuation coefficient depends both on the material and its density, it is represented by only one intensity value. Therefore, different materials might show very similar attenuation with possible overlapping intensity ranges. So far, no clear intensity threshold for separating lipid tissue from other tissues in CT data could be reported (see Table 1.3). This fact hampers an appropriate manual but also an automatic assessment of lipid plaque constituents. Hence, it would be desirable to enhance the contrast between the different tissues involved in a pre-processing step to make the subsequent assessment of lipid tissues more feasible.

As already mentioned, a drawback of the commonly used single source computed tomography systems is that different materials might show very similar attenuation at any selected radiation energy. This shortcoming can be overcome by measuring the attenuation of a tissue at two different energy levels – a so called dual energy (DE) acquisition.

Although conventional single source CT systems can be used for dual energy acquisitions by scanning a patient twice in a row, this has not been established in clinical routine as the beating heart induces motion artifacts which would have to be compensated by proper registration algorithms. In 2005, the first commercial dual energy CT (DECT) system was introduced that allowed the simultaneous acquisition of attenuation values at two different energy levels [Flohr *et al.* 2006]. The novelty of this system is that two X-ray sources with an angular offset of $\pi/2$ are mounted within the gantry.

In this study, we researched this dual energy technology and leveraged its properties in an algorithm that simultaneously enhances the contrast between vessel lumen (filled with contrast agent), soft tissue, adipose tissue and calcium – the tissues needed for a proper assessment of atherosclerosis, and particularly lipid constituents, in coronary arteries.

5.1.1 Related Work

Dual energy X-ray acquisitions have been discussed and evaluated on basic phantoms since the late 1970s [Chiro *et al.* 1979, Genant and Boyd 1977, Lehmann *et al.* 1981, Marziani *et al.* 2002, Millner *et al.* 1979, Taibi *et al.* 2003]. However, the limitation of CT hardware and software technology hampered expansion to further clinical applications [Kelcz *et al.* 1979]. This lasted until 2005 when the first commercial dual energy CT system (DECT) was introduced [Flohr *et al.* 2006, Petersilka *et al.* 2008]. This system allows the simultaneous acquisition of two CT images at different energy levels. In order to benefit from the different attenuation characteristics at different energy levels, two most opposing energy levels, which are still justified in terms of noise and exposure, are selected for a dual energy acquisition. For the aforementioned DECT system, a tube voltage of $140\ \mathrm{kV}$ is normally selected for the high energy image whereas for the low energy image, a tube voltage of $80\ \mathrm{kV}$ or $100\ \mathrm{kV}$ – depending on the application – is selected [Graser *et al.* 2009].

Through a dual energy acquisition, two different intensity values can be assigned to a voxel, namely the one measured at the low energy level and one at the high energy level. Different approaches exist that make benefit of this additional information provided for each voxel as compared to conventional single source CT. Most apply directly on the *original intensity space* that is spanned by the intensities of the low and high energy image, respectively. Others, however, decompose the low and high energy image into other descriptors like characteristic tissues or into the density and atomic number.

Original intensity space

When remaining in the original intensity space, each voxel is represented by a point in the 2D space spanned by the intensity values of the low and high energy image, respectively. Through this additional dimension, materials can be better differentiated as each tissue has a specific attenuation characteristic at the selected energy levels and thus appears at specific locations within the intensity space. Boll *et al.* [2006] therefore proposed a subtraction of the high and low energy image for a better characterization of tissues. Stolzmann *et al.* [2008c] defined a 2D threshold – a line in the intensity space – to differentiate uric acid stones.

Besides the separation of tissues through 2D thresholds or clustering approaches, a so-called three material decomposition can be applied in the original intensity space [Johnson *et al.* 2007]. For this, three idealized materials (e.g. soft tissue, bone, iodine) are defined in the intensity space [Petersilka *et al.* 2008]. Hence, two ideal vectors originating from a common start point (e.g. at soft tissue) and ending at two different points (e.g. one vector from soft tissue to iodine, one vector from soft tissue to bone) can be defined. Based on these two vectors, a new coordinate system can be derived. With this new coordinate system, a given voxel can now be described by the proportions of each of the three idealized materials. Furthermore, a material separation and a subsequent segmentation can be performed for every voxel [Petersilka *et al.* 2008].

The usage of the aforementioned two approaches brought about material analysis capabilities with several potential clinical applications [Johnson *et al.* 2007, Graser *et al.* 2009], such as bone removal [Watanabe *et al.* 2009], iodine content computation [Johnson *et al.* 2007], virtual non-contrast imaging [Graser *et al.* 2009], lung ventilation [Goo *et al.* 2008], classification of kidney stones and gallstones [Graser *et al.* 2008, Primak *et al.* 2007, Scheffel *et al.* 2007, Stolzmann *et al.* 2008c], evaluation of lung perfusion defects, or evaluation of perfusion defects in the myocardium [Ruzsics *et al.* 2008].

The dual energy CT technique dramatically increases the amount of data collected and therefore impacts the clinical workflow [Holmes III *et al.* 2008]. One way to simplify image review is to fuse the low and high energy image into a unique blended data set with desirable properties. Johnson *et al.* [2007] constructed a so-called *virtual* 120 kV *image* by mixing linearly the 80 kV (30% weighting) and the 140 kV (70% weighting) image, respectively. Behrendt *et al.* [2009] further evaluated this approach by varying the weighting factor. For evaluation, they measured the signal to noise ratio (SNR) as well as the intensity changes for different weighting factors and concluded best results with a weighting factor of 0.5 for the enhancement of the ascending aorta and paraaortal fat. Eusemann *et al.* [2008] developed and evaluated several non-linear blending functions including a binary blending function, a slope blending function, a gaussian function, and a modified sigmoid function. The latter one showed a promising performance on preliminary results such that Holmes *et al.* [2008] further evaluated this function both in a liver phantom and patient study. They concluded that this non-linear blending of dual

energy data can provide an improvement in the contrast-to-noise over linear blending and is accompanied by a visual preference for non-linear blended images by the reader.

Basis decomposition

In general, depending on the type of information which is retrieved, three different classes of basis decompositions can be distinguished [Walter *et al.* 2004]. In the first class, the high and low energy image are converted into two components representing the effective atomic number and density of the tissues. In the second class, the attenuation due to Compton scattering and due to electron density are chosen, whereas in the last class, the physical densities of two known components are selected as a basis.

Heisemann *et al.* [2003, 2006] followed the first basis decomposition approach by computing the effective atomic number and tissue density out of the acquired dual energy images. For body fluids in an ex-vivo setting, they could show an improved material differentiation with this method. However, our own results on clinical DECT data and phantoms have shown that this approach is very sensitive to noise – reflected by the fact that Heismann *et al.* [2003, 2006] chose a high tube current for their scans.

Lehmann *et al.* [1981] used a non-linear transformation on the high and low energy images to generate energy-independent images which are based on two selected basis materials. Thereafter, characteristic linear combinations of these two basis images are used to create a single so-called *cancelation* image. Depending on a single parameter, Lehmann's algorithm canceled the contrast between two materials to enhance a third one, or it enhanced the contrast between materials – both demonstrated on experimental settings with a stationary X-ray source. Marziani *et al.* [2002] applied Lehmann's cancelation algorithm in mammography with quasi-monochromatic X-rays. On a phantom, they could show the feasibility of minimizing or canceling the contrast between glandular and fat tissues while maximizing the low signal arising from pathologic tissues. Also for mammography, Chen *et al.* [2005] presented a dual-basis-material decomposition for cone-beam CT imaging. On a digital phantom, they showed the feasibility for image contrast enhancement with the proposed technique. Walter *et al.* [2004] proposed a basis decomposition of the raw sinogram data from flat-panel detectors into two chosen basis materials. On phantoms and simulations, they concluded that reconstructed density maps of the chosen basis functions could improve the differentiation of materials. This was true even in cases where different neighboring materials had the same linear attenuation value. Senguapta *et al.* [2005] applied the same approach on electron-beam CT to differentiate regions containing calcium and iodine in phantom images.

None of the aforementioned studies for dual energy basis decompositions have been applied on commercial DECT systems with clinical settings so far but were only evaluated on phantoms with non-clinical examination protocols. As the algorithm by Lehmann *et*

al. [1981] looks promising and flexible in being able to either enhance or cancel the contrast between materials, we followed this approach and investigated its suitability to improve the assessment of atherosclerosis on clinical DECT data sets.

5.2 Methods

The principle of the tissue cancelation algorithm by Lehmann *et al.* [1981] is summarized in Figure 5.1 and described below in detail. First, the original low and high energy images are non-linearly decomposed into two basis material images to map the density distribution ρ_A and ρ_B of two arbitrarily chosen basis materials A and B. Thereafter, the two bases are combined in a cancelation step to a single projection or cancelation image to enhance or cancel the contrast between targeted tissues.

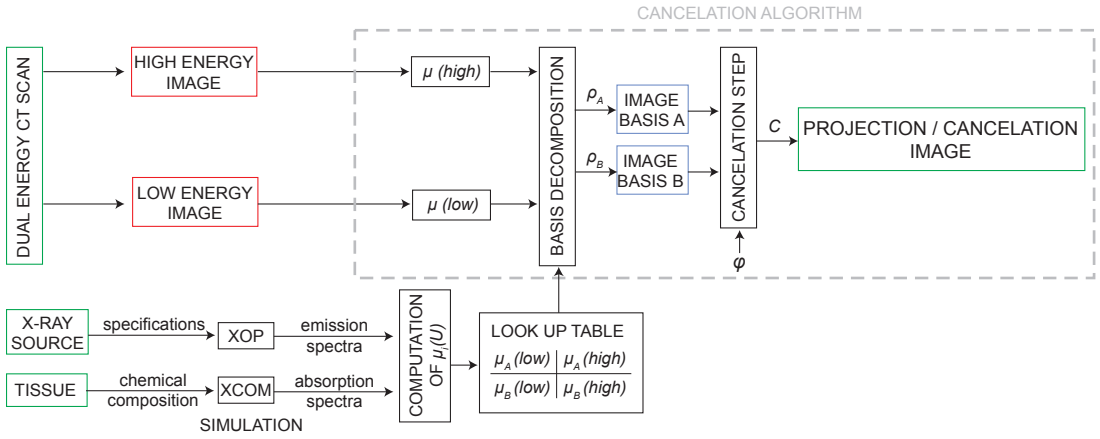

***Figure 5.1**: Workflow of the tissue cancelation algorithm proposed by Lehmann* et al. *[1981].*

5.2.1 Basis Material Decomposition

Assuming energies above the K-edge – which is the case for the diagnostic range of CT acquisitions – the attenuation coefficient $\mu_\Gamma(E)$ of any material Γ can be approximated by a combination of photoelectric absorption and Compton scattering [Lehmann *et al.* 1981]

$$\mu_\Gamma(E) = \alpha\mu_\rho(E) + \beta\mu_C(E) \tag{5.1}$$

with E the photon energy, $\mu_\rho(E)$ the attenuation due to photoelectric effect, $\mu_C(E)$ the attenuation due to Compton scattering, and α,β the tissue depending weights.

With dual energy acquisitions, the attenuation for each voxel is measured twice, namely at a high (E_h) and a low energy level (E_l), respectively, which yields in a set of two equations with two unknowns

$$\begin{aligned} \mu(E_l) &= \alpha\mu_\rho(E_l) + \beta\mu_C(E_l) \\ \mu(E_h) &= \alpha\mu_\rho(E_h) + \beta\mu_C(E_h). \end{aligned} \tag{5.2}$$

This set of equations can now be solved for the two tissue specific constants α and β

$$\begin{aligned} \alpha &= \frac{\mu_C(E_h)\mu(E_l) - \mu_C(E_l)\mu(E_h)}{\mu_\rho(E_l)\mu_C(E_h) - \mu_\rho(E_h)\mu_C(E_l)} \\ \beta &= \frac{\mu_\rho(E_l)\mu(E_l) - \mu_\rho(E_h)\mu(E_h)}{\mu_\rho(E_l)\mu_C(E_h) - \mu_\rho(E_h)\mu_C(E_l)}. \end{aligned} \tag{5.3}$$

Lehmann *et al.* [1981] have further shown that the attenuation coefficient of any material Γ can be expressed as a linear combination of the attenuation coefficients of two suitably chosen basis materials A and B (A $\neq$ B)

$$\mu_\Gamma(E) = \alpha\mu_\rho(E) + \beta\mu_C(E) = \rho_A\mu_A(E) + \rho_B\mu_B(E). \tag{5.4}$$

Solving for the material densities ρ_A and ρ_B of the two chosen basis materials A and B yields in

$$\begin{aligned} \rho_A &= \frac{\mu_A(E_h)\mu(E_l) - \mu_A(E_l)\mu(E_h)}{\mu_B(E_l)\mu_A(E_h) - \mu_B(E_h)\mu_A(E_l)} \\ \rho_B &= \frac{\mu_B(E_l)\mu(E_l) - \mu_B(E_h)\mu(E_h)}{\mu_B(E_l)\mu_A(E_h) - \mu_B(E_h)\mu_A(E_l)}. \end{aligned} \tag{5.5}$$

In this set of equations, the attenuation coefficients of the two bases μ_A and μ_B at the selected energy levels must be known. These coefficients can either be obtained by scanning the selected basis materials or by simulations as applied and described in the following.

5.2.2 Basis Material Attenuation Coefficients

The attenuation coefficient of a tissue depends on its chemical composition [Heismann *et al.* 2003], which therefore has to be known for the basis materials. Table 5.1 lists the

***Table 5.1**: Chemical composition (percentages) of selected body tissues as reported in literature [International Commission on Radiation Units and Measurements 1989, Jones et al. 2003]*

element	H	C	N	O	Na	Mg	Si	P	S	Cl	K	Ca	Fe
atomic number	1	6	7	8	11	12	14	15	16	17	19	20	26
adipose	11.4	59.8	0.7	27.8	0.1	-	0.1	-	-	0.1	-	-	-
blood	10.2	11.0	3.3	74.5	0.1	-	-	0.1	0.2	0.3	0.2	-	0.1
heart	10.3	12.1	3.2	73.4	0.1	-	-	0.1	0.2	0.3	0.2	-	0.1
muscle	10.2	14.3	3.4	71.0	0.1	-	-	0.2	0.3	0.1	0.4	-	-
soft tissue	7.2	59.2	2.2	21.8	-	9.3	0.2	-	-	0.1	-	-	-
skeleton													
- cartilage	9.6	9.9	2.2	74.4	0.5	-	-	2.2	0.9	0.3	-	-	-
- cortical bone	3.4	15.5	4.2	43.5	0.1	0.2	-	10.3	0.3	-	-	22.5	-
- spongiosa	8.5	40.4	2.8	36.7	0.1	0.1	-	3.4	0.2	0.2	0.1	7.4	0.1
- yellow marrow	11.5	64.4	0.7	23.1	0.1	-	-	-	0.1	0.1	-	-	-

chemical composition of typical body tissues as reported in literature. With this composition, the attenuation coefficient $\mu(E)$ which is dependent of the incident photon energy E can be obtained with XCOM, a photon cross sections database [Berger and Hubbell 1987].

However, an X-ray tube as used in CT systems is not mono-energetic but emits photons within a certain range of energies. Hence, the attenuation of a tissue is composed of the various attenuations at the different energies. For this reason, the energy spectrum of an X-ray tube at the different possible tube voltages is needed. As these spectra are not published by the manufactures, we have used XOP [del Rio and Dejus 1998] to compute the photon energy distribution $N_U(E)$ of a Tungsten X-ray tube at tube voltage U, which is – according to discussions with manufactures – a good approximation. Figure 5.2 shows the resulting spectra for the four possible tube voltages of the available DECT system.

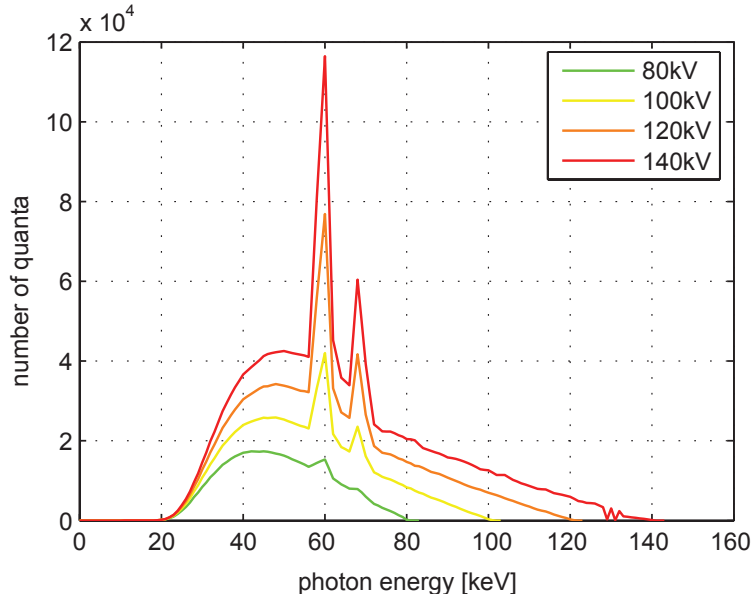

***Figure 5.2**: Photon energy distribution of a Tungsten X-ray tube at tube voltages of* 80 kV, 100 kV, 120 kV, *and* 140 kV.

The attenuation coefficient $\mu_i(U)$ of the basis material i at the tube voltage U is finally calculated by

$$\mu_i(U) = \frac{\int_0^\infty N_U(E)\mu_i(E)dE}{\int_0^\infty N_U(E)dE} \tag{5.6}$$

where $N_U(E)$ is the photon energy distribution at tube voltage U and $\mu_i(E)$ is the attenuation for material i at the photon energy E.

5.2.3 Cancelation Step

Based on the decomposition, a basis material plane or *basis plane* spanned by ρ_A and ρ_B can be defined. In this plane, each material Γ is represented by a vector $\vec{r}_{P_\Gamma}$. Lehmann *et al.* [1981] have shown that the position P_Γ of a material Γ in the basis plane only depends on characteristics constants of both material Γ and the basis materials A and B.

When the vector $\vec{r}_{P_\Gamma}$ is now projected onto a unit vector directed outwards from the basis plane origin at angle φ, and the length of this projection C is displayed for every voxel, the resulting image is called a basis projection image or *cancelation image*

$$C = \rho_A sin(\varphi) + \rho_B cos(\varphi) \tag{5.7}$$

with φ, the cancelation angle as a parameter. Depending on the selection of φ, contrasts between materials in the projection image can be enhanced or canceled. Figure 5.3 exemplarily shows a cancelation of the contrasts between two materials Ψ and Φ as – with the selected cancelation angle φ – they are projected onto the same point $P'_C = P'_\Psi = P'_\Phi$. Simultaneously, the contrast towards a third material Γ – *i.e.* the distance between P'_C and P'_Γ – remains.

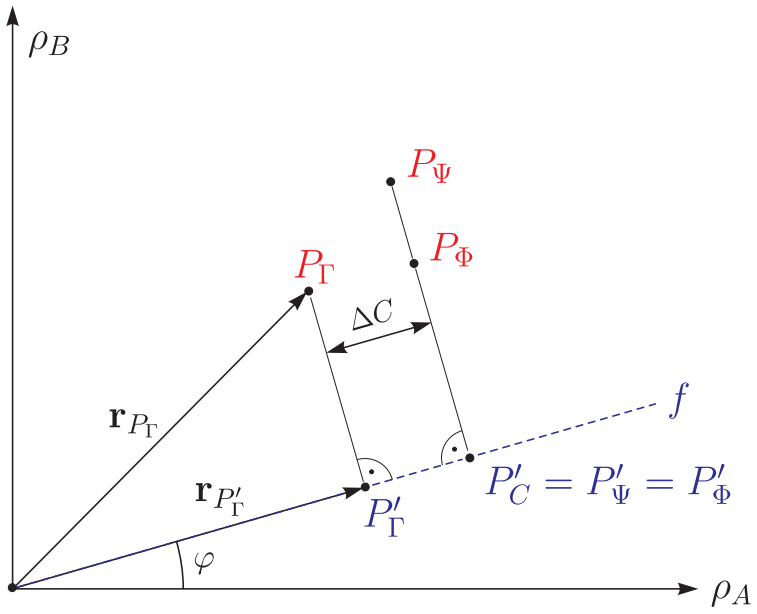

***Figure 5.3**: Basis plane spanned by ρ_A and ρ_B. In the basis plane, the tissue cancelation algorithm proposed by Lehmann* et al. *[1981] can be interpreted as the projection of the point from a measured tissue onto a vector directed from the origin with the angle φ. Depending on the selected cancelation angle φ, contrasts between tissues can be enhanced or canceled.*

The concept of tissue cancelation allows a broad range of applications while being able to cancel or to enhance the contrast between tissues. For the following study, we have applied this method on clinical DE data sets to evaluate its suitability to support the assessment of atherosclerosis, namely to enhance the contrast among tissues involved in such an assessment.

5.3 Experimental Setup and Results

The presented method for contrast enhancement is evaluated on five abdominal contrast-enhanced delayed phase DE scans showing both lipid and calcified plaques in the descending aorta. Abdominal DE examinations are chosen because no cardiac DE examinations were available at the time of the experiments. The data sets were acquired on a Siemens Definition CT scanner (Siemens Medical Solutions, Forchheim, Germany). The study was approved by the local ethics committee. The examination protocol as described in [Stolzmann *et al.* 2008a] was used. The tube voltage for the high energy image was $140\ \mathrm{kV}$ with a tube current-time product of $95\ \mathrm{mAs}$, and the tube voltage for the low energy image was $80\ \mathrm{kV}$ with a tube current-time product of $400\ \mathrm{mAs}$. The in-plane resolution and slice spacing ranged between $0.68 - 0.87\ \mathrm{mm}$ with a slice thickness of $2\ \mathrm{mm}$.

For the assessment of atherosclerosis, a good contrast between vessel lumen, soft tissue, adipose, and calcium is desired. Therefore, we manually select a region R_i within a data set for each material i ($i = 1..4$), *i.e.* a region for the lumen and tissue (both $7 \times 7 \times 9$ voxels), for adipose ($5 \times 5 \times 1$ voxels), and for calcium ($3 \times 3 \times 1$ voxels). The mean intensity $\bar{I}_i$ and standard deviation σ_i are computed within each R_i for every data set. The cancelation angle φ is varied between $-\pi$ and $+\pi$ with a step of 0.01. For each selected φ, the contrast enhancement factor (CEF) between material i and j is computed as

$$\mathrm{CEF}_{ij} = \frac{|\bar{I}_{c_i} - \bar{I}_{c_j}|}{\bar{I}_{c_i} + \bar{I}_{c_j}} \Big/ \frac{|\bar{I}_{h_i} - \bar{I}_{h_j}|}{\bar{I}_{h_i} + \bar{I}_{h_j}}\ , \tag{5.8}$$

where CEF represents the enhancement ratio of the contrast in the cancelation image (index c) and the original high energy image (index h). Hence, a CEF > 1 should be achieved. Further, the signal to noise ratio $\mathrm{SNR}_i = \bar{I}_i/\sigma_i$ is measured for each material i in the low and high energy, and cancelation image, respectively. The cancelation angle is only dependent on the materials to be enhanced [Lehmann *et al.* 1981] such that we expected different optimal cancelation angles for the various targeted tissues which, however, should be universally applicable for all patient images. We evaluated this by measuring the CEF and SNR subject to the cancelation angle φ. Further, we determined the optimal angles maximizing the contrast between two targeted tissues.

Among all considered basis material pair combinations between iodine, calcium, water (H_2O), polymethyl methacrylate ($C_5O_2H_8$), adipose, and blood, the pair calcium-

adipose showed the best results in terms of magnitude and robustness for the intended contrast enhancement such that this basis pair is used for this study.

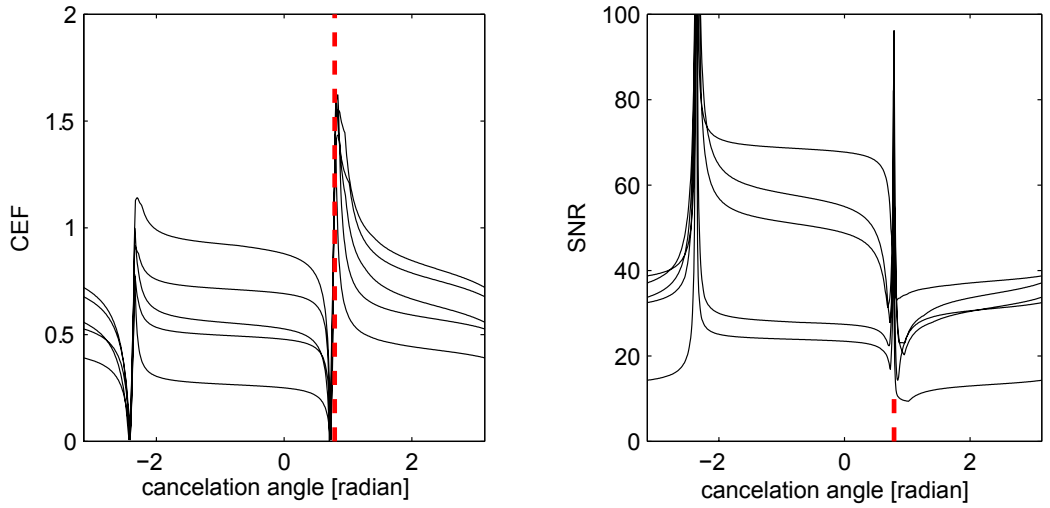

(a) Contrast enhancement factor (CEF) *(b)* Signal to noise ratio (SNR).

***Figure 5.4**: Contrast enhancement factor (a) and signal to noise ratio (b) in dependence on the cancelation angle φ for all data sets as well as the selected φ^* (dashed line) that simultaneously enhanced the contrast among all targeted tissues.*

Figure 5.4 exemplarily shows the CEF between adipose and calcium as well as the SNR for adipose in dependence of φ for all data sets. Our initial expectation regarding patient independent characteristics could be justified. The mean $\overline{\text{CEF}}$ and mean $\overline{\text{SNR}}$ over all data sets are computed and for each possible tissue combination, we determined an optimal cancelation angle φ_{max} that maximized $\overline{\text{CEF}}$ (Table 5.2).

***Table 5.2**: For each possible material combination of lumen, tissue, adipose, and calcium, we determined the cancelation angle φ_{max} that maximized the mean contrast enhancement factor ($\overline{CEF}$) measured between the cancelation image and the $140\ \text{kV}$ acquisition over all data sets.*

	$\overline{\text{CEF}}\ (\varphi_{max})$ lumen	$\overline{\text{CEF}}\ (\varphi_{max})$ tissue	$\overline{\text{CEF}}\ (\varphi_{max})$ adipose	$\overline{\text{CEF}}\ (\varphi_{max})$ calcium
lumen	-	1.58 (0.81)	2.82 (0.84)	1.30 (0.81)
tissue	1.58 (0.81)	-	1.16 (0.80)	1.38 (0.81)
adipose	2.82 (0.84)	1.16 (0.80)	-	1.48 (0.81)
calcium	1.30 (0.81)	1.38 (0.81)	1.48 (0.81)	-

As all φ_{max} are very similar, we decided to determine one single optimal angle φ^*. Based on one data set, we chose the optimal angle $\varphi^* = 0.79$ that maximized the CEF among all

tissue combinations and simultaneously showed a good SNR for each material. A higher CEF would be possible with a slightly larger φ but resulting in a worse SNR. The optimal angle φ^* is then fixed and applied on all data sets. The contrast between all targeted tissues could be simultaneously enhanced between 8% and 67% (Table 5.3). Except for calcium, the SNR in the cancelation image was also higher than the SNR measured in the 80 kV and 140 kV data sets, respectively.

***Table 5.3**: We measured the mean (±std) contrast enhancement factor ($\overline{CEF}$) for the cancelation image ($\varphi = 0.79$) against the high energy 140 kV acquisition for each possible material combination. Further, the mean (±std) signal to noise ratio ($\overline{SNR}$) in the cancelation, the 80 kV and the 140 kV images was measured.*

	lumen	tissue	adipose	calcium
$\overline{\text{SNR}}$ cancelation	61.6 (±28.2)	39.6 (±17.8)	60.9 (±23.5)	11.3 (±1.6)
$\overline{\text{SNR}}$ 140kV	51.4 (±11.7)	37.8 (±10.9)	56.7 (±15.5)	14.7 (±6.3)
$\overline{\text{SNR}}$ 80kV	42.9 (±22.2)	27.3 (±14.2)	40.4 (±18.3)	9.5 (±0.7)
$\overline{\text{CEF}}$ lumen	-	1.27 (±0.06)	1.67 (±0.34)	1.16 (±0.03)
$\overline{\text{CEF}}$ tissue	1.27 (±0.06)	-	1.08 (±0.08)	1.19 (±0.03)
$\overline{\text{CEF}}$ adipose	1.67 (±0.34)	1.08 (±0.08)	-	1.23 (±0.04)
$\overline{\text{CEF}}$ calcium	1.16 (±0.03)	1.19 (±0.03)	1.23 (±0.04)	-

Before DE examinations became feasible, a standard tube voltage of 120 kV was usually chosen for single energy scans as this tube voltage results in a good trade-off between noise and contrast in an image [Holmes III *et al.* 2008]. For this reason, the commercial reconstruction software of Siemens also creates a virtual 120 kV – or *mixed* – data set by mixing linearly the intensity information of each voxel $v(x, y, z)$ from the 80 kV and 140 kV data set, respectively, according to [Johnson *et al.* 2007]

$$v_{mixed}(x, y, z) = 0.3 \cdot v_{80\,\text{kV}}(x, y, z) + 0.7 \cdot v_{140\,\text{kV}}(x, y, z). \tag{5.9}$$

We therefore also compared the CEF and SNR arising from the cancelation image with the measured values in the mixed image. Figure 5.5 exemplarily depicts a CT slice showing all four regarded tissues in the 80 kV, 140 kV, mixed, and cancelation image, respectively.

When comparing the contrast enhancement for all possible tissue combinations (Fig. 5.6), the cancelation image still shows an average CEF of 1.08 (±0.05) towards the mixed image. However, the advantage of having an improved SNR in the cancelation image dissolves when taking the mixed image as a reference (Fig. 5.7). No significant differences in the SNRs for the four tissues could be observed (paired Student's t-test, p=$\{$0.99, 0.26, 0.40, 0.15$\}$ for $\{$lumen, tissue, adipose, calcium$\}$) .

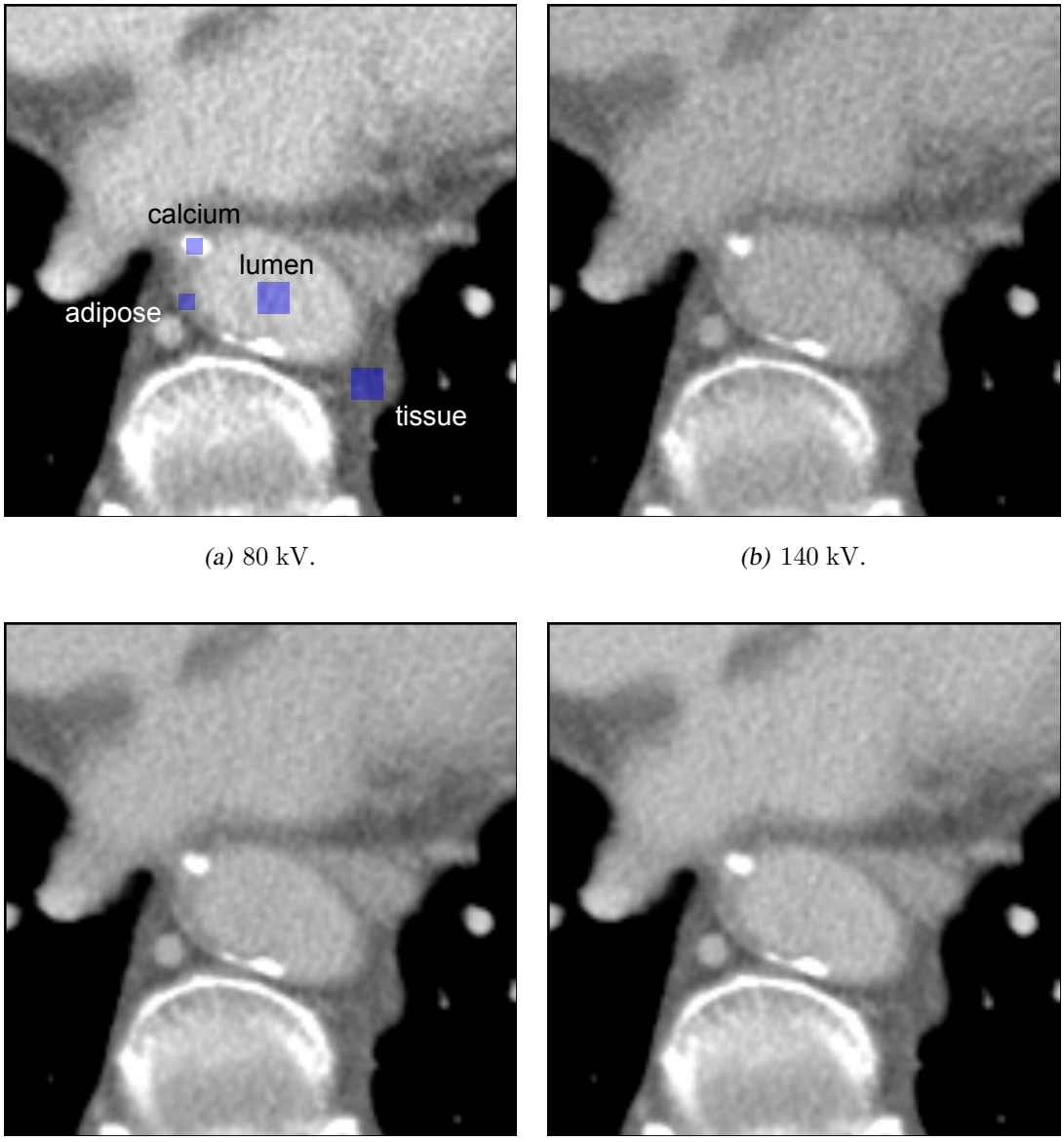

(a) 80 kV. *(b)* 140 kV.

(c) Mixed (30% 80 kV, 70% 140 kV). *(d)* Cancelation image.

***Figure 5.5**: CT slice showing the contrasts among the four regarded tissue types (adipose, calcium, lumen, tissue) in one axial slice in both the* 80 kV *(a),* 140 kV *(b), mixed (c) and cancelation image (d), respectively.*

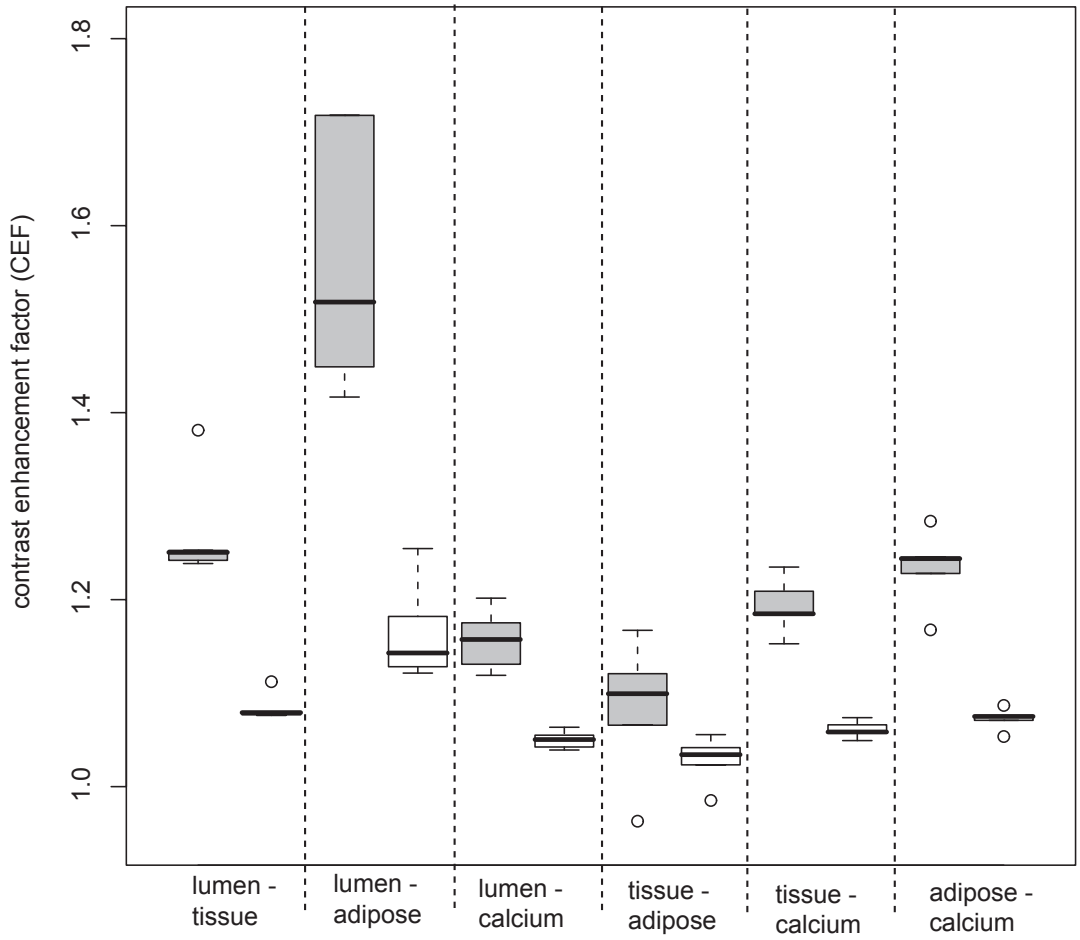

***Figure 5.6**: Measured contrast enhancement (CEF) for various tissue combinations between the proposed method and the* $140\ \mathrm{kV}$ *(gray) or mixture image (white), respectively.*

5.4 Discussion and Conclusion

In this work, the performance of a tissue cancelation algorithm for contrast enhancement was evaluated for the first time on real DECT patient data. We could show that there is one fixed, patient-independent optimal angle for the assessment of atherosclerosis by measuring the contrast enhancement between targeted tissues. In choosing this angle, we achieved a contrast enhancement among all targeted tissues when comparing the results to the $140\ \mathrm{kV}$ image and to the mixed image that is currently applied in commercial software. In the first case, even the SNR could be improved in the cancelation image whereas in the latter one, a similar SNR as compared to the mixed image was measured. We therefore regard the proposed procedure as a potential pre-processing step for the

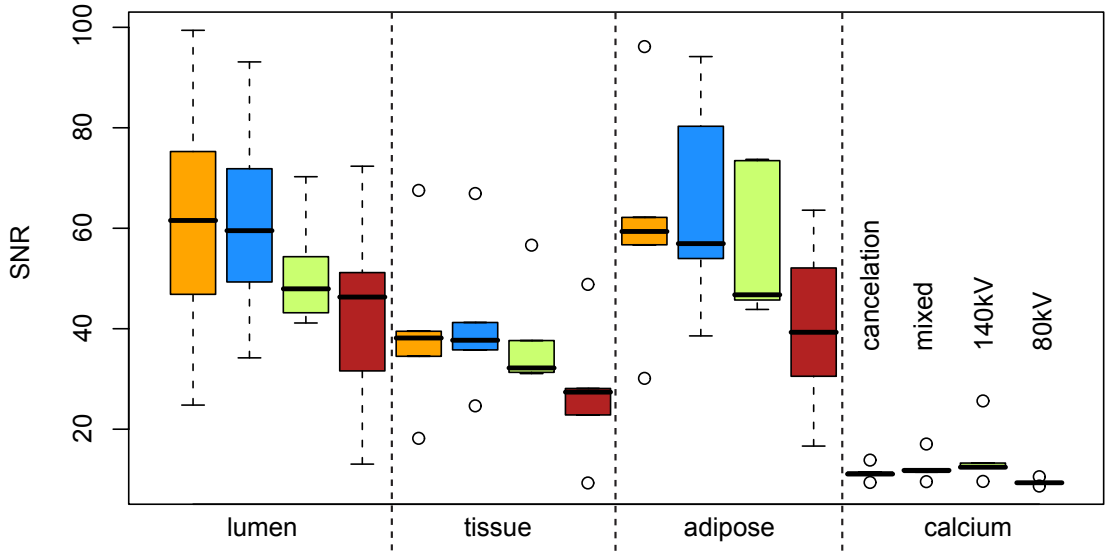

***Figure 5.7**: Measured range for the signal to noise ratio (SNR) for the four different tissue types in the cancelation, mixture, 140 kV, and 80 kV image, respectively.*

assessment of atherosclerosis. Both the studies by Eusemann *et al.* [2008], Behrendt *et al.* [2009], and our study show the benefit of DE acquisitions for contrast enhancement in CT images. Unfortunately, as all these studies targeted different organs and tissues, a direct performance comparison is not justified at this point.

Contrast enhancement between tissues increases the robustness of both manual and automatic object segmentation as the range for a decision threshold is enlarged. However, even with this contrast enhancement, the assessment of lipid plaque constituents in coronary arteries still remains challenging due to several reasons. First of all, the examination in the dual energy mode hampers the usage of the second X-ray tube in the CT scanner for an improved temporal resolution as it is normally done in cardiac acquisitions. Hence, more motion artifacts are induced and it has to be verified if these artifacts still justify the usage of a contrast enhancement algorithm. Second, plaque volumes in the coronary arteries are smaller than those observed in the ascending aorta as done for this study. So, even with a contrast improvement of around 10%, the detection still remains difficult when a plaque has a volume of only a few voxels. Lastly, it is difficult to establish well-suited ground truth data for the evaluation and training of algorithms as both CT and IVUS have a moderate sensitivity in the detection of lipid plaques.

These limitations might be the reason why only the two aforementioned algorithmic approaches have been proposed so far for the assessment of coronary soft plaques in single energy CT images. The method by Renard and Yang [2008] relied on the effective cross-section area of the wall and the lumen. However, Leber *et al.* [2006] concluded in their study that a current limitation of 64-slice CT is the exact separation of lumen, plaque,

and vessel wall. Hence, it has to be questioned on how sensitive the method is towards a correct detection of the vessel wall. This cannot be answered at this point as their method was only tested on two coronary arteries. The learning approach by Teßmann *et al.* [2008] looks more promising, but it has to be verified if it is also suitable for the detection of non-stenotic soft plaques. None of the presented studies mentioned if they are also applicable on bifurcations – the preferred location for the development of atherosclerosis [Asakura and Karino 1990, Medina *et al.* 2006].

In general, plaques might be stenotic or non-stenotic and they can appear either at bifurcations or within the course of a vessel. Calcified plaques can be assessed a lot easier by using their characteristic intensity value as criterion. Unfortunately, this is not that easily transferable for noncalcified plaques. Therefore, we will briefly analyze additional features that might be used for an automatic assessment of lipid plaques in future applications. Stenotic soft plaques cause a narrowing of the vessel lumen. This property can be used in various ways. Either one can evaluate the change in the lumen as done by Renard and Yang *et al.* [2008], or one can analyze the intensities within a fixed area as proposed by Teßmann *et al.* [2008]. A more severe problem is the assessment of non-stenotic soft plaques as they do not narrow the vessel lumen. For their assessment, the outer vessel wall has to be reliably determined such that the space between vessel lumen and outer vessel wall can be analyzed for lipid tissue. Knowledge about the outer vessel wall is therefore the key issue for an automatic assessment of non-stenotic soft plaques. Renard *et al.* [2008] propose an adaptive region growing on a voxel basis for this task. However, we think that more accurate approaches have to be considered that determine the vessel wall at sub-voxel accuracy as the wall thickness of a healthy coronary artery ranges between 30 and 100 μm and is thus smaller than the in-plane resolution of a CT scanner.

Besides the differences between stenotic and non-stenotic lesions, the location of these lesions within the coronary arteries is also an important factor that influences an assessment. At bifurcations, it is difficult to reliably extract geometrical features as the branching causes a natural variation in the vessel area and diameter. This complicates a decision whether the observed change is solely based on the branching or if a plaque causes an additional change at this location. Hence, detailed knowledge about the vessel morphology, *i.e.* both its lumen and wall boundary would be of great advantage. Therefore, a precise segmentation of the vessel lumen and the vessel wall – including all plaques – is needed in general, and especially in the case for bifurcations. However, known vessel segmentation approaches only cover the vessel lumen and calcified tissue and therefore exclude lipid tissues and information about the vessel wall. To our opinion, the key elements towards an automatic assessment of lipid tissues in coronary arteries are an accurate segmentation of the vessel lumen and the outer vessel wall with sub-voxel precision. Taking advantage of this information, subsequent algorithms – which may be based on the approaches proposed for MRI and IVUS image data – can analyze the vessel wall and lumen for the presence of lipid tissues. Thereby, the algorithms can benefit from an en-

hanced contrast between the tissues as proposed within this work. Other approaches to further support the assessment of atherosclerosis, and in particular the assessment of lipid tissues, could be the incorporation of results from computational fluid dynamics simulations [Olgac *et al.* 2008] or the usage of contrast agents that enhance lipid tissues [Hyafil *et al.* 2007]. Further, an analysis of spatial plaque distribution patterns can also create additional evidence for the assessment of atherosclerosis which will be shown and discussed in the subsequent chapter.

6

Spatial Distribution Patterns of Atherosclerosis

In the preceding chapters, methods for the automatic and semi-automatic assessment of atherosclerosis have been described and developed. All these methods base their decision on the available intensity information in the CT data sets. However, due to noise or artifacts, this intensity information might be ambiguous. In these cases an automatic or manual assessment becomes difficult and a clear distinction between atherosclerosis and the surrounding tissue will be hardly possible. So it would be desirable to support the assessment with additional – non-intensity based – information to make it more robust. A possible source of information are spatial distribution patterns of atherosclerosis. When learned on a large population, knowledge about frequently observed patterns in the spatial distribution might be helpful to support the decision whether a plaque is present in a specific segment or not – both for an automatic assessment but also for a manual detection.

The aim of this work was to assess the spatial distribution patterns of atherosclerosis in coronary arteries and to research and evaluate the possibilities that arise with the knowledge of distribution patterns. As a first application that benefits from spatial distribution patterns, a *guided review* to support manual plaque detection will be introduced.

After the motivation of the proposed approach and a review of already observed plaque distributions, a framework for the extraction of spatial plaque distribution patterns will be introduced and evaluated. Besides an analysis of observed distribution patterns, the guided review process to support the manual assessment of atherosclerosis will be introduced and intensively evaluated. A final discussion of the results concludes this chapter.

6.1 Introduction

Although automatic and semi-automatic algorithms exist to support plaque detection, an ambiguity in the measured intensity values due to noise or artifacts may arise such that

a distinct differentiation between plaque and surrounding tissue becomes difficult – both for an algorithm and a human observer.

In such cases, algorithms might fail or produce false positives, whereas for an observer, her uncertainty and therefore the variability in the decision increases: so when asked to repeatedly label plaques for a patient, the results may vary (*i.e.*, *intra-observer* variability). But also the decisions between observers may not be in consensus (*i.e.*, *inter-observer* variability).

Hence, it is the objective to increase the robustness of atherosclerotic plaque detection by incorporating intensity independent information that further supports the decision for the presence of plaques. The spatial distribution patterns of atherosclerosis are a possible additional source of such information. Therefore, we have investigated the spatial distribution patterns with frequent itemset mining – an algorithm commonly used to derive relations among observed items. As a first application that benefits from the knowledge about spatial distribution patterns, we have developed guided review to support manual plaque detection. This guided review takes advantage of learned patterns and suggests segments for review showing high probability of having plaques that may be initially missed by an observer.

6.1.1 Related Work

The amount of available and applied methods for pattern recognition and data mining tasks is too comprehensive to be summarized as these techniques are researched and applied in a wide range of domains. We will therefore only focus on the frequent itemset mining technique and its usage in medical applications.

Frequent itemset mining is a method to derive relations among observed items. Originally, it was used for market basket analyses [Agrawal *et al.* 1993]. In such analyses, patterns of products frequently bought together are searched. Nowadays, frequent itemset mining is applied in many domains to search for patterns among items, like in computer vision [Quack 2009] or in medical applications. Chen and Chen [2006] identified potential correlations among the states of proteins using frequent itemset mining. Huang *et al.* [2007] used frequent itemset mining for a systematic discovery of functional modules and context-specific functional annotation of the human genome. Wright and Sittig [2006] used frequent itemset mining to create an ambulatory computerized physician order entry system. Several algorithms exist for the application of frequent itemset mining. Besides the orignal Apriori-based approach [Agrawal *et al.* 1993], other scalable frequent itemset mining methods have been proposed as alternatives [Grahne and Zhu 2003, Han *et al.* 2000, Liu *et al.* 2002, Pei *et al.* 2001]. The difference between these algorithms are both the approaches and the computational complexity for the extraction of frequent itemsets.

So far, only correlations between risk factors and coronary artery diseases or between risk factors and the pure existence of plaques were researched. Couturier *et al.* [2004] applied frequent itemset mining on the STULONG database to identify different patient groups on the basis of risk factors. Hausleiter *et al.* [2006] investigated the relation between non-calcified plaques and coronary artery diseases. The localization of thin cap fibroatheromas [Cheruvu *et al.* 2007, Virmani *et al.* 2006], ruptured plaques [Cheruvu *et al.* 2007, Pregowski *et al.* 2006], stenoses [Maehara *et al.* 2001], and occlusions [Wang *et al.* 2004] within the coronary artery tree have been reported. Shimada *et al.* [2006] assessed the circumferential distribution pattern of plaques at bifurcations. Differences in calcification patterns in patients with acute coronary syndromes versus those with stable angina pectoris have been shown [Beckman *et al.* 2001, Ehara *et al.* 2004, Fujii *et al.* 2005, Hong *et al.* 2007]. Ehara *et al.* [2004] further reported typical patterns for patients with acute myocardial infarction, acute coronary syndromes, and stable angina pectoris.

In the aforementioned studies, all plaques have been regarded independently. A possible correlation among the localization of plaques within the coronary artery tree was not regarded. For the first time, this work investigates spatial distribution patterns of atherosclerosis in the coronary artery tree by using the frequent itemset mining algorithm.

The learned spatial distribution patterns are then used to search for segments where no plaques are labeled by a reader but that simultaneously show – according to the observed frequent patterns – a high probability of having plaques which might have been missed. These segments are chosen and presented again to the reader who can revise her original decision. This process will be referred to as *guided review* because a complete second reading is omitted by guiding the reader to specific segments within the coronary tree to detect potentially missed plaques.

6.2 Methods

Frequent itemset mining [Agrawal *et al.* 1993] is used to determine rules that describe spatial correlations between plaques. The method was introduced by Agrawal *et al.* [1993] and was driven by market basket analysis. In such an analysis, the *items* in customers' baskets are analyzed to find sets of products that are frequently bought together. After the observation of a number of baskets, so-called *association rules* can be derived to express the probability that – given a set of items (*itemset*) in a basket – certain other items are also present. These association rules represent statistical correlations which can be used to research the dependencies among items and to predict the content of new baskets if only some items are given.

For the research of spatial distribution patterns of atherosclerosis, we adapted the market basket analysis by frequent itemset mining to our special purpose. Hence, a patient corre-

sponds to a basket and existing plaques are described as items. Multiple items are defined and assigned to each plaque as described in the following.

6.2.1 Itemset

For pattern analysis with frequent itemset mining, the observed plaque distribution has to be described meaningfully by items. Therefore, we developed an itemset $\mathcal{I} = \{i_1 \dots i_n\}$ that represents the set of all n possible items i available to describe spatial plaque distribution within the coronary artery tree. For each patient j $(j = 1 \dots m)$, a transaction or observation o_j is then created by determining a subset $\mathcal{A}$ of $\mathcal{I}$ containing the items that describe the observed plaque distribution. In general, such a subset $\mathcal{A}$ of $\mathcal{I}$ with l items, *i.e.* $\mathcal{A} \subseteq \mathcal{I}$, $|\mathcal{A}| = l$ is called a *l-itemset*.

For the plaque position, a multi-scale approach in form of an itemset tree was developed to assign several items per plaque position. This allows the statistical analysis within and between different levels, *i.e.* it is possible to extract correlations between various segments but also between segments and certain areas (left, right, proximal, distal, ...) of the coronary tree.

The proposed itemset tree (Fig. 6.1 and 6.2) consists of six hierarchical levels - based on the 16-segment AHA coronary artery scheme as described in Section 1.1.3. In addition to the 16 segments, the 9 bifurcations of the model are also included as position, as bifurcations are preferred locations for the development of plaques [Asakura and Karino 1990, Medina *et al.* 2006].

1. It is distinguished whether a plaque is in the *left* or *right* coronary artery tree.
2. The position is further specified as right coronary artery (*RCA*), left main artery (*LM*), left anterior descending artery (*LAD*), left circumflex artery (*CX*), or segment 16 (*EXTRA*) which is not present in each patient's anatomy.
3. The relative position within one of the main coronary arteries is determined. A plaque is either *proximal*, *mid*, or *distal*.
4. The actual position *seg_x* in one of the segments of the coronary artery tree is regarded.
5. The plaque type is distinguished, namely *hard*, *mixed*, or *soft*.
6. The plaque is either *obstructive* or *non-obstructive*.

Some items like the relative positions *proximal*, *mid*, or *distal* are not unique as they appear in different branches of the itemset tree. Therefore, those items – indicated by an elliptical shape in Figure 6.1 and 6.2 – are combined with all unique items found while going up the itemset tree from the corresponding item to the root of the tree. Hence, the non unique item *proximal* in the right coronary artery tree, for example, is specified

by the unique items *RCA_proximal* and *right_proximal*. The items for an observation are created by computing the union set of the items created for the various labeled plaques of a patient. The items for a labeled plaque are obtained by starting from the leaf in the itemset tree that describes the plaque and taking all items found while going from the leaf to the root. The patient's gender is considered by assigning either the item *gender_male* or *gender_female* to an observation. A soft plaque in segment 1 of a male patient will therefore get the following labels: *gender_male*, *right*, *rca*, *rca_proximal*, *right_proximal*, *seg_1*, *seg_1_soft*, *rca_soft*, *right_soft*.

For the subsequent analysis of spatial plaque distribution patterns in the form of association rules, the set $\mathcal{O}= \{o_1 \dots o_m\}$ of observations, also referred to as the *observation database* $\mathcal{D}$, will be used.

6.2.2 Association Rules

An *association rule* is an implication of the form $\mathcal{A} \rightarrow \mathcal{B}$ where $\mathcal{A}$ and $\mathcal{B}$ are itemsets and $\mathcal{A} \cap \mathcal{B} = \emptyset$. In general, the itemsets $\mathcal{A}$ and $\mathcal{B}$ can have arbitrary lengths, but we restricted their length to $|\mathcal{A}| = 4$ and $|\mathcal{B}| = 1$ to get more meaningful rules. The implication of an association rule can therefore be interpreted as *conditions* $\rightarrow$ *conclusion (support, confidence)* and expresses a relation of one or more items – the *conditions* – and one item as the *conclusion*. The quality of an association rule is expressed by its support and confidence measure.

The *support* [Borgelt and Kruse 2002] of an association rule is the percentage of cases in which it applies in the training set. The *confidence* [Agrawal *et al.* 1993] of an association rule is the percentage of cases in which the rule is correct relative to the number of cases in which it is applicable, *i.e.* the conditions are met. An example association rule might be *seg_2, seg_3* $\rightarrow$ *seg_1 (40%, 95%)*. So with the knowledge that plaques are present in *seg_2* and *seg_3* – which was true in 40% of all observations in the training data set – there is a probability of 95% that also a plaque in *seg_1* is present.

To select interesting rules from the set of all possible rules, constraints in form of a user-specified minimum support min_{supp} and minimum confidence min_{conf} value are used. Association rules that do not fulfill these constraints are discarded. To achieve this, the association rule generation is a two-step process. First, min_{supp} is applied to find all corresponding itemsets in the database $\mathcal{D}$. In a second step, these *frequent itemsets* (*i.e.*, itemsets that have a support $s \geq min_{supp}$) and the minimum confidence constraint min_{conf} are used to form the association rules. Finding all frequent itemsets in D in the first step is difficult since it involves searching all possible itemsets (*i.e.*, item combinations). The set of possible itemsets is the power set over $\mathcal{I}$ and has the size $2^n - 1$ with n the number of items in $\mathcal{I}$. Although the size of the power set grows exponentially with n, an efficient search is possible using the downward-closure property of support [Agrawal *et al.* 1993]. This property guarantees that for a frequent itemset also all its subsets are frequent

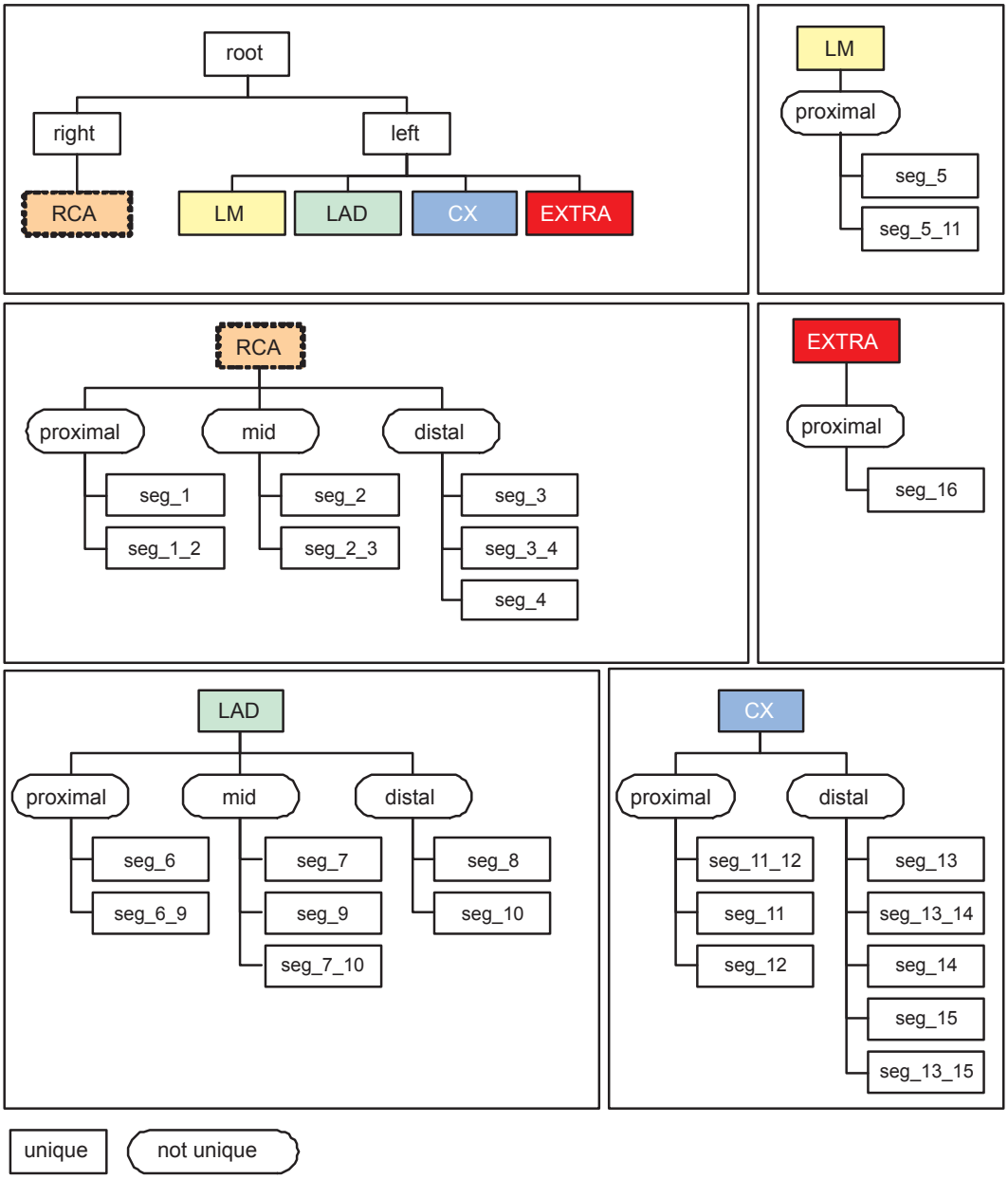

Figure 6.1: *Each plaque is described by a set of items. The items are derived from a developed itemset tree. The multi-scale approach in form of a tree allowed the statistical analysis of the plaque distribution within and between different levels. The itemset tree consists of six levels whereof level one (left/right), level two (RCA/LM/LAD/CX/EXTRA), level three (proximal/mid/distal), and level four (segment within the coronary artery tree) are illustrated in this figure.*

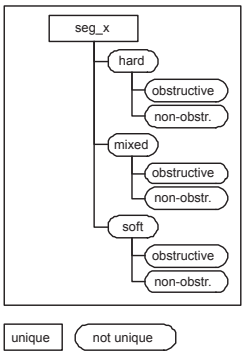

***Figure 6.2**: The itemset tree consists of six levels whereof level five (hard/mixed/soft) and level six (obstructive/non-obstructive) are illustrated in this figure.*

and thus for an infrequent itemset, all its supersets must be infrequent. The apriori algorithm by Agrawal *et al.* [1993] as shown in Algorithm 4 [Quack 2009] uses this efficient approach. It performs a breadth-first search through the search space of all itemsets by iteratively generating candidate itemsets $\mathcal{C}_{l+1}$ of size $l+1$. The algorithm alternates between two phases: (1) the database pass phase, where the support of the itemsets in $\mathcal{C}_l$ is calculated and checked if it surpasses the frequency threshold min_{supp} and (2) the phase of candidate formation for $l+1$ itemsets. A more detailed description and analysis of this algorithm can be found in [Quack 2009].

Algorithm 4 apriori

$l \leftarrow 1, \mathcal{L} \leftarrow \emptyset$
$\mathcal{C}_l \leftarrow \{\{\mathcal{A}\}$ item of size $1, \mathcal{A} \in \mathcal{D}\}$
while $\mathcal{C}_l \neq \emptyset$ **do**
  $\mathcal{L}_l \leftarrow \emptyset$
  database pass:
  for $\mathcal{A} \in \mathcal{C}_l$ **do**
    if $\mathcal{A}$ is frequent **then**
      $\mathcal{L}_l \leftarrow \mathcal{L}_l \cup \mathcal{A}$
    end if
  end for
  candidate formation:
  $\mathcal{C}_{l+1} \leftarrow$ sets of size $l+1$ whose all subsets are frequent
  $\mathcal{C}_l \leftarrow \mathcal{C}_{l+1}$
  $\mathcal{L} \leftarrow \mathcal{L} \cup \mathcal{L}_l$
end while
return $\mathcal{L}$

We used the apriori implementation of the frequent itemset mining tool *apriori* (`http://www.borgelt.net/apriori.html`) [Borgelt and Kruse 2002] to determine as-

sociation rules. The computed association rules were then filtered to only keep non trivial rules. Trivial rules are defined as those rules where the condition items are within the subtree of the itemset tree given with the conclusion item as root. An example of a discarded trivial rule would be *LAD* $\rightarrow$ *left* as it is obvious that the LAD is per definition in the left coronary artery tree.

When applied on plaque data that are labeled according to the aforementioned itemset, spatial plaque distribution patterns can be obtained with the association rules which then can be analyzed for clinically relevant dependencies. Besides this analysis, we further propose to use the spatial dependencies to support the manual detection of plaques by a guided review that will be introduced in the next paragraph.

6.2.3 Guided Review

The idea of guided review is to use the extracted spatial distribution patterns expressed by association rules to guide a reader to specific segments that were not labeled as having plaques but that show a high probability of containing plaques. So, guided review is intended to support the detection of initially missed plaques and hence to increase the robustness of plaque detection.

For this, a set of association rules has to be learned in advance from an appropriate population. Afterwards, these association rules can be used to search for initially missed plaques. To this end, the current plaque labeling of a patient is taken and the items are computed according to the defined itemset. These items are then regarded as possible conditions and the set of association rules is searched if – with the given condition items – association rules exist with a segment as conclusion that has so far not been labeled as having plaques. To assure a certain generality and quality, a required minimum support min_{supp} and confidence min_{conf} value for the association rules can be selected such that rules having lower values are discarded. All possible segments showing evidence of having unlabeled plaques are extracted and presented for review.

Guided review can be realized either as an online- or an offline-tool. In the first case, the current labeling of a reader – or the results of a detection algorithm – would be automatically analyzed and segments of potential plaque locations would be highlighted while the reader is still detecting plaques. In the latter case, the guided review would be manually triggered after the labeling and the list of segments with potentially missed plaques would then be shown to the reader.

Figure 6.3 shows a development prototype of guided review as a web application. The reader can select her labeled plaques in a schematic coronary artery tree and as a result, the web application highlights segments of potentially missed plaques.

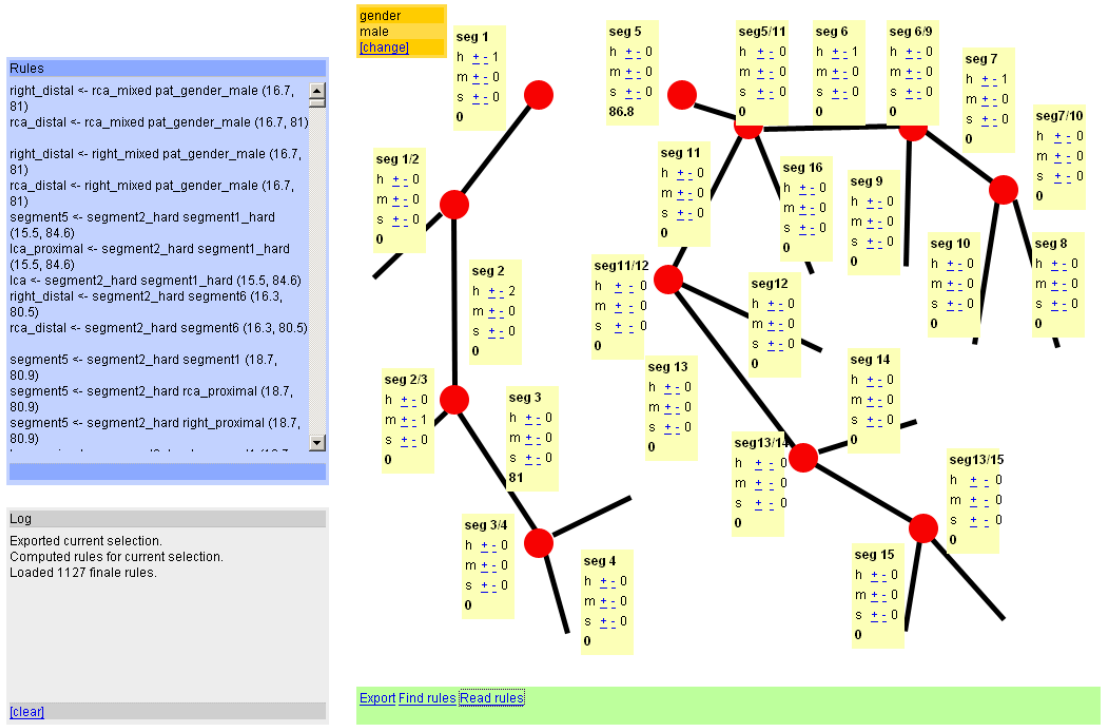

Figure 6.3: *Prototype of guided review as a web application. The reader can select her labeled plaques in a schematic coronary artery tree and as a result, the web application highlights segments of potentially missed plaques.*

To introduce guided review by frequent itemset mining and to show its benefit in making manual plaque detection more robust, we performed several simulations and clinical studies as described in the following section.

6.3 Experimental Setup and Results

For the evaluation of guided review by frequent itemset mining, labeled plaque distribution patterns from a large number of patients are used. Besides an analysis of the association rules for clinically interesting distribution patterns, guided review is applied during several simulations. First, the impact of the two parameters of frequent itemset mining, namely the minimum confidence min_{conf} and support min_{supp} value is investigated. Afterwards, with an optimal parameter setting, guided review is performed both in simulations and in clinical praxis to test its suitability to predict initially missed plaques. The performance of the method is compared with a weighted random approach.

6.3.1 Data Acquisition

The basis for the subsequent experiments are plaques observed in 252 consecutive patients (166 male, 86 female) who underwent CTCA for clinical indications. Demographic data and clinical characteristics of the patients are summarized in Table 6.1.

***Table 6.1**: Patient demographics and clinical characteristics of the study population.*

	total
number of patients	252 (100%)
age (years)	64.5±11.6 (28-88)
male/female	166/86 (65.9%/34.1%)
body mass index ($\mathrm{kg/m^2}$)	25.7±4.0 (19.1-34.1)
heart rate (bpm)	67.3±6.8 (51-88)
risk factors	
smoker	121 (48.0%)
diabetes	29 (11.5%)
high serum cholesterol	110 (43.7%)
arterial hypertension	160 (63.5%)
positive family history	101 (40.1%)
reason for referral	
typical angina	40 (15.9%)
atypical angina	66 (26.6%)
non anginal chest pain	145 (57.5%)

All patients had a low- to intermediate pre-test probability of having CAD and suffered from typical angina (15.9%), atypical angina (26.6%), or non-anginal chest pain (57.5%). None of the patients suffered from unstable angina. All patients were referred for ruling-out significant coronary stenoses. They were scanned on a Dual-Source CT scanner (Somatom Definition, Siemens Medical Solutions, Forchheim, Germany) following a standard CTCA protocol. The scanning parameters were selected as listed in Table 1.2. The CT scans were performed from the level of the tracheal bifurcation to the diaphragm in a cranio-caudal direction. CTCA scans were reconstructed with a slice thickness of $0.75\ \mathrm{mm}$, a reconstruction increment of $0.4\ \mathrm{mm}$, and using a soft-tissue convolution kernel (B26f).

A graphical user interface has been developed with the MeVisLab software (MeVis Medical Solutions AG, Bremen, Germany) for the manual labeling of the coronary plaques. Patient information from all data sets was removed prior to the data analysis in order to allow for an anonymized read-out. A radiologist with 7 years of experience in cardiovascular imaging determined type, position, and the degree of stenosis for each plaque and

associated them with one of the aforementioned 25 possible positions. A plaque is assigned to a bifuraction when it is centered in this location and does not extend more than $2\ \mathrm{mm}$ into adjacent coronary segments. If a plaque extends over more than one segment, it is labeled according to its most proximal position. For clarity, the term *segment* will be equivalently used to refer to a segment or bifurcation in the following. Three different types of plaques are differentiated, namely hard, mixed, and soft plaques as defined in Section 1.3.4. The plaques are further characterized as being *obstructive*, indicating a vessel diameter narrowing greater than 50%, or as *non-obstructive*, indicating a luminal narrowing below 50%, based on CTCA.

In total 1229 plaques (990 hard, 80.6%; 227 mixed, 18.5%; 12 soft, 1%) distributed over 916 coronary segments and 507 vessels were manually labeled (Table 6.2). In 200/252 (79.4%) of the patients, at least one coronary plaque (range 1-22 plaques) was found. The average number of plaques for patients having at least one plaque was 6.1 (median 5). Male patients had on average 6.9 plaques (5.6 hard, 1.3 mixed, and 0.05 soft plaques), being significantly ($p < 0.001$, Mann-Whitney U test) more than the average in female patients (average 4.0, 3.3 hard, 0.6 mixed, and 0.05 soft plaques). Hard and mixed plaques were most often found in segment 6 (132x hard, 48x mixed), segment 1 (126x hard, 34x mixed), and segment 7 (112x hard, 25x mixed). Due to the low number of soft plaques, no preferred location for those plaques could be identified. A total of 129 (10.5%) obstructive plaques (95 hard, 31 mixed, 3 soft) and 1100 (89.5%) non-obstructive plaques were detected in the 200 patients having plaques, as determined by CTCA. Obstructive plaques were most often located in segment 7 (23x), segment 6 (22x), and in segment 1 (18x) (see Table 6.2).

6.3.2 Spatial Plaque Distribution Patterns

In a first step, we evaluated the spatial plaque distribution patterns being present in the study population. Based on the labeled plaques, frequent itemset mining extracted a total of 70'796 association rules with a minimum confidence value of 80% and a minimum support of 15% – the values of the selected parameters are discussed in the subsequent section. In general, several rules exist showing evidence for a plaque at one and the same position. The differences between those rules are the amount of conditions but also the conditions themselves. Simple patterns are characterized by association rules with only one condition item (e.g. seg_3 $\rightarrow$ seg_6 (24.6, 88.7)) whereas more specific patterns had multiple condition items (e.g. seg_3 & CX $\rightarrow$ seg_6 (18.3, 91.3)). These specific patterns have higher confidence values. However, the support values decrease for more complex rules because their underlying plaque distribution patterns are less frequently observed in the patients.

Four special plaque distribution patterns could be identified in the 252 patients. Fifty-two of the 252 patients (20.6%) had no plaques at all; 80 of the 252 patients (31.7%) had

***Table 6.2**: Plaque distribution in the study population at 25 possible locations (segments and bifurcations) of the coronary artery tree as determined by CTCA.*

segment/	all palques			obstructive plaques		
bifurcation	hard	mixed	soft	hard	mixed	soft
1	126	34	3	11	6	1
1_2	2	1	0	1	0	0
2	73	11	2	5	2	1
2_3	0	0	0	0	0	0
3	80	20	0	5	1	0
3_4	0	0	0	0	0	0
4	45	9	0	0	0	0
5	70	21	1	5	1	0
5_11	0	0	0	0	0	0
6	132	48	2	16	6	0
6_9	3	1	0	1	0	0
7	112	25	1	18	5	0
7_10	1	1	0	0	1	0
8	78	11	2	1	2	1
9	27	5	1	3	1	0
10	20	4	0	3	2	0
11	78	15	0	10	3	0
11_12	1	0	0	0	0	0
12	25	4	0	3	0	0
13	54	9	0	10	1	0
13_14	0	0	0	0	0	0
13_15	0	0	0	0	0	0
14	19	0	0	1	0	0
15	16	1	0	1	0	0
16	28	7	0	1	0	0

plaques only in the left coronary artery tree; 117 of the 252 patients (46.4%) had plaques both in the left and the right coronary artery tree; and 3 of the 252 patients (1.2%) had plaques solely in the right coronary tree (Fig. 6.4).

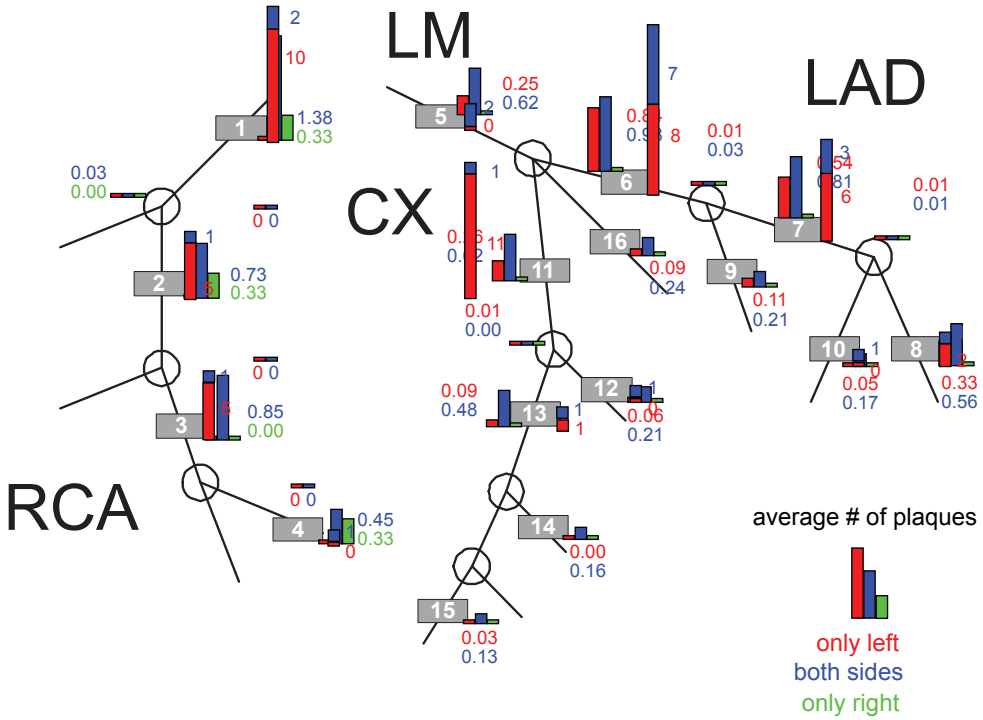

***Figure 6.4**: Schematic representation of the coronary artery tree (annotated according to the AHA scheme) illustrating the spatial plaque distribution patterns in the 200 patients with coronary plaques. The figure shows the average number of plaques encountered in each segment of the coronary artery tree for each group separately. In 31.7% of the patients, plaques were found only in the left coronary artery tree; in 46.4% of the patients, plaques were found both in the left and the right coronary artery tree, whereas in 1.2% of the patients, plaques were located solely in the right coronary tree.*

The assignment of multiple items for each plaque allows for a pattern analysis at (*i.e.*, vessel to vessel, segment to segment) and between different hierarchical levels (*i.e.*, segment to vessel and vice versa). As we can only give an overview of the extracted association rules, we focus on plaque distribution patterns with association rules having one condition item in the following. If multiple association rules fulfilled this criterion, the one with the highest confidence value is chosen.

Vessel to vessel. Strong rules having a high support and confidence value were found indicating the existence of a plaque in the left anterior descending (LAD) given a plaque

in any of the segments of the RCA. Furthermore, strong rules supporting the existence of a plaque in the LAD were found, given a plaque in the left main artery (LM) or the CX (see Table 6.3).

Segment to segment. On this hierarchical level, a plaque in segment 3, 4, 5, 11 or 13 predicted a plaque in segment 6 with a high confidence (80.5% to 90.9%). Similarly, a plaque in segment 2 predicted a plaque in segment 1 with a high confidence of 84.8% (see Table 6.3).

Segment to vessel. Various rules were found predicting plaques in other vessels giving the existence of a plaque in certain segments: for example a plaque in segment 1, 2, 3, 5, 11 or 13 predicted a plaque in the LAD with high confidence (see Table 6.3).

Vessel to segment. Rules predicting plaques in certain vessels were found based on existing plaques in other segments. For example, having a plaque in the CX, there was a confidence of 86.7% that also a plaque in segment 6 is present. A plaque in the LM predicted a plaque in segment 6 with a confidence of 80.5% (see Table 6.3).

Mixed and soft plaques. The aforementioned patterns do not predict a certain type of plaque within a specific segment or vessel, but only give evidence for a plaque in general. However, as mixed and soft plaques are more difficult to assess (see Chapter 5), it would be desirable to have association rules that indicate the presence of mixed and soft plaques. For mixed plaques, no association rules were found using the minimum confidence value of 80% and one single condition item such that we lowered the confidence threshold to 65% and allowed for up to two condition items. Then, several prediction rules were found to predict the existence of mixed plaques at the vessel level – *i.e.* either within the right coronary tree or within the left coronary tree (Table 6.4). No rules were found predicting mixed plaques in specific segments. As only 12 soft plaques were labeled in the patients of this study (representing 1% of all plaques), no relevant patterns could be discerned with regard to this plaque type.

6.3.3 Validation of Guided Review

We first studied the impact of the two parameters for frequent itemset mining, namely min_{supp} and min_{conf}. Afterwards, guided review by frequent itemset mining is validated by simulating various settings of initially missed plaques. The quality of segment selection by frequent itemset mining is compared to a weighted random approach.

Table 6.3: *Association rules including all coronary plaque types given an existing plaque as condition and a predicted plaque at certain locations as a conclusion.*

hierarchical level	condition	conclusion	support [%]	confidence [%]
vessel→vessel	RCA	LAD	47.6	92.5
	LM	LAD	32.5	90.2
	CX	LAD	38.9	95.9
segment→segment	segment 2	segment 1	26.2	84.8
	segment 3	segment 6	24.6	88.7
	segment 4	segment 6	15.1	86.8
	segment 5	segment 6	32.5	80.5
	segment 11	segment 6	28.6	87.5
	segment 13	segment 6	17.5	90.9
segment→vessel	segment 1	LAD	40.1	93.1
	segment 2	LAD	26.2	90.9
	segment 3	LAD	24.6	95.2
	segment 4	LAD	15.1	92.1
	segment 5	LAD	32.5	90.2
	segment 11	LAD	28.6	95.8
	segment 13	LAD	17.5	100.0
vessel→segment	LM	segment 6	32.5	80.5
	CX	segment 6	38.9	86.7

Table 6.4: *Association rules for mixed plaques as conclusion either in the* left *or* right *coronary tree, respectively, given the existence of plaques (hard, mixed, or soft) at certain locations as conditions.*

hierarchical level	condition	conclusion	support [%]	confidence [%]
segments→branch	segment 2 & 3	right	17.9	68.9
	segment 6 & 8	left	19.4	65.3
segment & vessel →branch	segment 3 & LM	right	15.9	65.0
	RCA mixed & segment 6	left	16.3	68.3

Segment selection by frequent itemset mining. The plaque distribution of each patient is considered separately: given the observed items of each patient as possible values for the condition items, it is tested if there are association rules indicating the presence of additional plaques in segments not yet labeled. All segments where association rules match the form *any combination of observed items* $\rightarrow$ *seg_x* are then stored in a list L_{review} of segments to be reviewed.

Segment selection by weighted random approach. For comparison, a weighted random approach to select segments of potentially missed plaques is chosen as a benchmark as it represents the most intuitive way to select segments for review: those segments where in general many plaques occur have a higher probability of containing missed plaques. So, given the plaques of the current labeling for all patients, the probability

$$p_i = \frac{\text{\# of plaques in segment } i}{\text{total \# of plaques}} \tag{6.1}$$

is computed that a plaque occurs in segment i. Then n_{review} segments having no labeled plaques are chosen by a random number generator weighted with the probability p_i for each segment.

Simulation design. For each measurement, the study population of the 252 patients is randomly divided into a training set (70%, or 176 patients) and a testing set (30%, or 76 patients). The association rules are computed based on the observations from the training set. In order to get an incomplete labeling, $p_{segments}$ percent of the plaques in the testing set are randomly removed. This parameter is introduced to simulate radiologists who initially missed a number of plaques. The incomplete labeling of the testing set is then taken to compute the list L_{review} containing n_{review} segments with potentially missed plaques. All segments in L_{review} are evaluated if plaques were initially present in the ground truth labeling. The number n_{found} finally represents the number of segments where initially removed plaques are re-found through the guided review. For comparison, the same number of segments proposed by frequent itemset mining is also chosen using the weighted random approach and evaluated for the presence of initially missed plaques. Simulations are done with varying values for $p_{segments}$, min_{conf} and min_{supp}. Each experiment is repeated 100 times to get statistically more reliable results.

Parameter study. The impact of the frequent itemset mining parameters min_{conf} and min_{supp} on the outcome of the guided review is evaluated by varying the corresponding parameter while keeping the remaining setting fixed.

The confidence expresses a probability that an association rule is valid when its conditions are met. It can thus be expected that while using association rules with low confidence

values, more segments have to be reviewed until a missed plaque is detected. To evaluate the impact of the confidence value, min_{conf} is varied between 60% and 95% in steps of 5% whereas the remaining parameters are kept constant, *i.e.* $p_{segments} = 15\%$ and $min_{supp} = 15\%$. Figure 6.5(a) shows – subject to the selected confidence level – the detection ratio $r = n_{found}/n_{segment}$ which is defined as the quotient between the number n_{found} of found plaques and the number $n_{segment}$ of removed plaques.

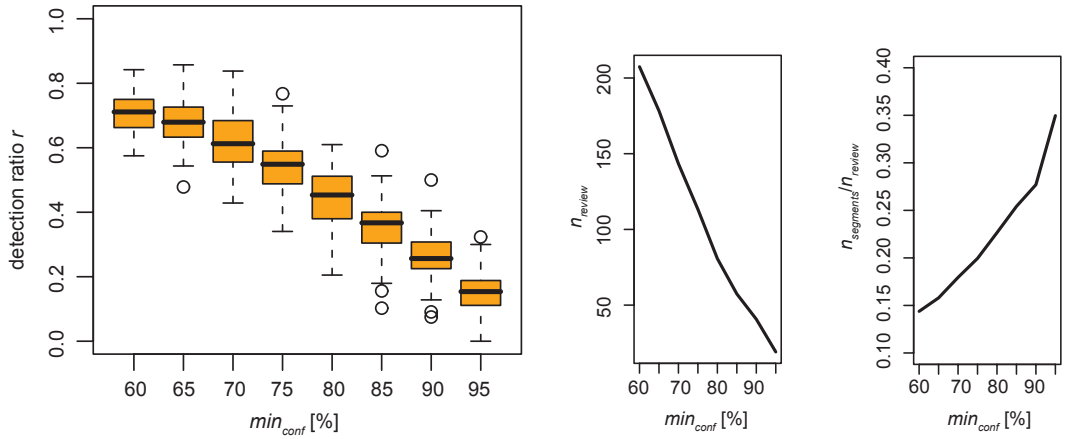

(a) Detection ratio r.

(b) Number of reviewed segments n_{review}.

(c) Average number of found plaques per reviewed segment.

***Figure 6.5**: Impact of the minimum confidence parameter min_{conf} on the detection ratio r (a) the number of segments n_{review} to be reviewed (b) and on the average number of found plaques per reviewed segment (c). Less plaques were detected with higher values for min_{conf}. The number of segments to be reviewed declined with an increasing value for min_{conf}.*

In general, a lower bound for the confidence value led to a higher percentage of detected plaques as with a small confidence value more rules and therefore more segments for review are created. A drawback of this higher detection ratio is, however, the higher number of segments to be reviewed (Fig. 6.5(b)). Figure 6.5(c) finally confirms the initial expectation that with higher confidence values less segments had to be reviewed to detect an initially missed plaque.

The support of a rule is a measure of its generality. A small value indicates that the rule was created from observations in only a small number of cases and therefore might depend more on the selection of the study population than a rule with a high support value. To evaluate the impact of the support value, min_{supp} is varied between 5% and 25% in steps of 5%, whereas the remaining parameters are kept constant, *i.e.* $p_{segments} = 15\%$ and $min_{conf} = 80\%$. Figure 6.6(a) shows the detection ratio r subject to the selected minimum support value. A lower bound for the support value led to a higher percentage of de-

tected plaques but also required a higher number of segments to be reviewed (Fig. 6.6(b)). Figure 6.6(c) finally shows the average number of detected, initially missed plaques per reviewed segment.

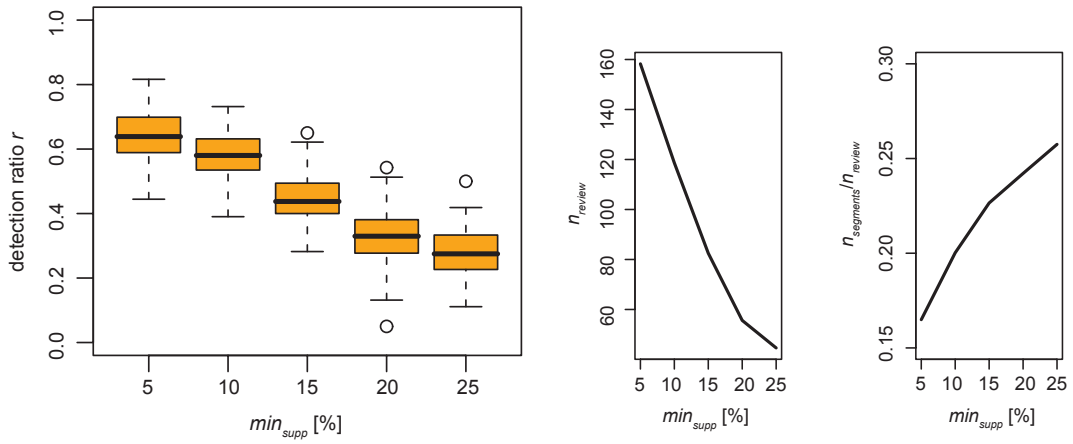

(a) Detection ratio r.

(b) Number of reviewed segments n_{review}.

(c) Average number of found plaques per reviewed segment.

***Figure 6.6**: Impact of the minimum support parameter min_{supp} on the detection ratio r (a) the number of segments n_{review} to be reviewed (b) and on the average number of found plaques per reviewed segment (c). Less plaques were detected with higher values for min_{supp}. The number of segments to be reviewed declined with an increasing value for min_{supp}.*

Considering the investigation above, the joint distribution of min_{supp} and min_{conf} does not contain one distinct optimum. Hence, for the guided review the parameters $min_{supp} = 15\%$ and $min_{conf} = 80\%$ are chosen as a good trade-off between the detection ratio and the number of segments to review.

Performance Validation. For performance validation of guided review, the parameter setting as concluded in the preceding paragraph is chosen for the selection of association rules. In doing so, guided review by frequent itemset mining clearly outperformed ($p < 0.001$, paired Student's t-test) the weighted random selection approach in terms of the detection ratio r. Up-to 47% of the initially removed plaques could be re-found with the guidance of frequent itemset mining by reviewing only 4.4% of all possible segments.

As it is generally not known how many plaques have been missed, $p_{segments}$ is varied between 5% and 95% in steps of 5%. Figure 6.7 shows boxplots of the detection ratio r for the guided review by both the frequent itemset mining and the weighted random approach. The number of reviewed segments resulting from the chosen $p_{segments}$ are shown

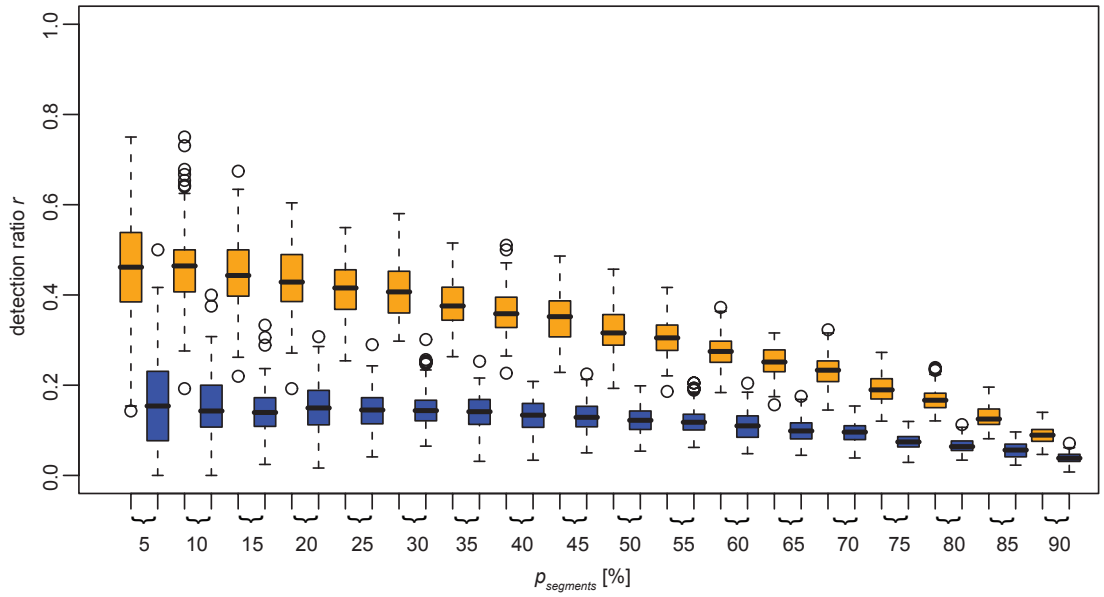

***Figure 6.7**: Performance comparison between guided review by frequent itemset mining (orange) and guided review by random selection (blue) for different values of $p_{segments}$. Frequent itemset mining clearly outperformed the random selection. Up-to 47% of the missed plaques could be detected if less than 20% of the initially labeled plaques were removed.*

in Figure 6.8. On average 84 segments – or 1.1 segments per patient – had to be reviewed, if less then 50% of the initial labeled plaques are removed. For larger values of $p_{segments}$, the performance of guided review by frequent itemset mining dropped which is predicable as in these cases, the available labeling is really sparse. So only a few association rules are valid from which segments to be reviewed could be determined.

Iterative guided review. A thinkable extension of guided review is to apply it iteratively as with each additional detected plaque, a refined distribution pattern arises that may trigger further association rules which may then predict additional segments to be reviewed. This iterative guided review is simulated by repeating the segment selection by the frequent itemset mining step until $L_{review_i} - L_{review_{i-1}} = \emptyset$, where i indicates the current and $i-1$ the preceding iteration step, respectively. After each iteration, the labeling used as input is updated with the re-found plaques from the preceding step.

Figure 6.9 shows the change $\Delta r = r_{iterative} - r$ in the detection ratio r that was measured for the iterative guided review in comparison to the standard guided review. For the validation of iterative guided review, the same parameter setting as for the validation of the standard guided review was used. In clinical praxis, it is expected that only a moderate

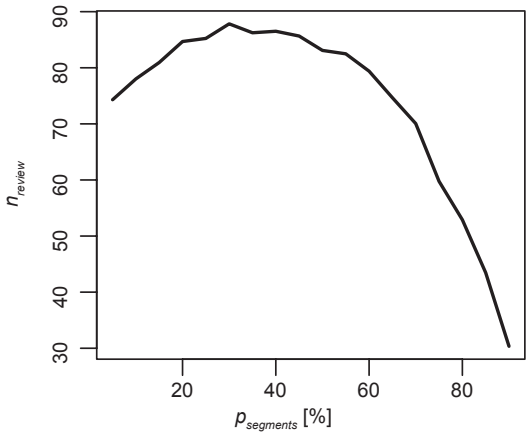

Figure 6.8: *Number of segments n_{review} proposed by frequent itemset mining for guided review. Above a certain percentage $p_{segments}$ of initially removed plaques, the labeling was too sparse such that only a small number of segments to be reviewed were proposed.*

number of plaques is missed by a radiologist. So, the expected additional benefit of iterative guided review is limited in this case.

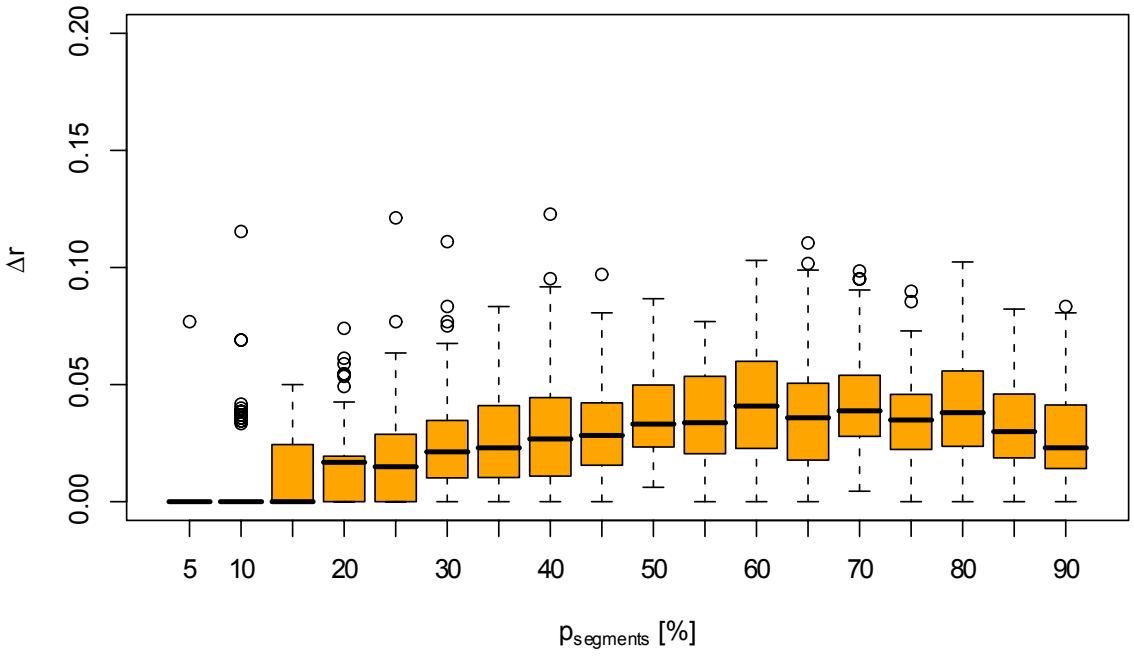

Figure 6.9: *Through the iterative application of guided review by frequent itemset mining, an increase Δr in the detection ratio could be observed which is shown in this figure in dependence on $p_{segments}$, the percentage of omitted plaques.*

Although with iterative guided review a slightly higher performance can be achieved, we evaluated the standard guided review approach in its clinical application because this approach allowed a more consistent statistical analysis of its performance.

6.3.4 Clinical Application of Guided Review

For a first clinical evaluation that uses plaque distribution patterns to improve the manual detection of plaques, we applied guided review by frequent itemset mining on the labeled 252 patients of this study to search for initially missed plaques.

Therefore, association rules ($min_{supp} = 15\%$, $min_{conf} = 80\%$) learned from the initial labeling of all patients were applied on each of the 252 data sets to search for additional plaques, *i.e.* association rules with segments as their conclusion given the current labeling of each data set as possible condition items. In this way, guided review by frequent itemset mining created a list of segments to be reviewed. For comparison, the same number of segments was determined by the weighted random approach as aforementioned. The reader from the initial labeling was then asked to review the selected segments from frequent itemset mining and the weighted random approach for the presence of missed plaques. For this second reading, the reader was blinded to the approach that selected the segment. To ascertain the presence of the initially missed plaques that were detected in the second reading, a second radiologist (also with 7 years of experience in cardiovascular imaging) was consulted for consensus. This guided review was performed three months after the initial labeling.

Based on the prediction rules extracted by frequent itemset mining, 193 segments in 133 patients were selected for the guided review. In these, an initially missed plaque was detected in 59 (30.6%) segments of 49 (36.8%) patients. From these 59 segments, 11 segments contained plaques extending over more than one segment such that those plaques were already labeled in the first reading with their most proximal segment position. Hence, in total 48 (24.9%) additionally detected plaques (32 hard, 13 mixed, 3 soft) in 41 (30.8%) patients were counted as true positives. In comparison, the weighted random approach revealed only 22 (14 hard, 5 mixed, 3 soft) initially missed plaques in the 193 segments in 131 patients selected by this approach. Guided review by frequent itemset mining performed significantly better ($p < 0.001$, Fisher's exact test) than the weighted random approach. The distribution of additionally detected plaques over the various segments is illustrated in Figure 6.10. The weighted random approach revealed 17 (77.3%) initially missed plaques in the left coronary tree and 5 (22.7%) in the right coronary tree. The results from frequent itemset mining were more balanced with 28 (58.4%) initially missed plaques in the left and 20 (41.6%) initially missed plaques in the right coronary tree, respectively.

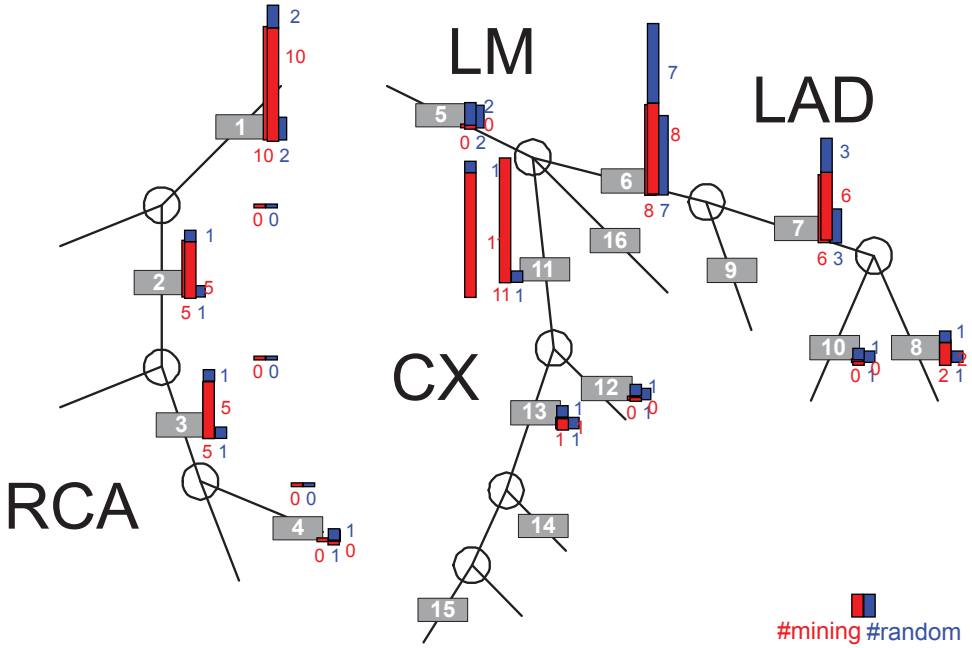

***Figure 6.10**: Schematic representation of the coronary artery tree indicating the number of plaques that were detected in the guided review by frequent itemset mining (red) and in the weighted random approach (blue). Guided review by frequent itemset mining performed significantly better ($p < 0.001$) than the random approach.*

6.4 Discussion and Conclusion

It has been well documented through a number of human epidemiological studies that atherosclerosis shows a non-uniform distribution in the coronary vasculature, not only among different coronary arteries, but also along different segments of the same vessel [Ehara *et al.* 2004, Zhu *et al.* 2008]. In this work we described spatial distribution patterns of coronary plaques while including the entire coronary artery tree into the analysis. The spatial plaque distribution patterns showed a predominance of plaques involving primarily the left coronary artery tree, whereas only 1% of the patients had plaques solely in the right coronary artery system. The observed patterns allowed for the extraction of association rules indicating the presence of plaques in certain positions, when plaques in other locations of the coronary artery tree were present. In patients with chronic CAD, the association rules mainly involved plaques being entirely calcified and – to a lesser degree – plaques being of mixed composition. Use of these association rules significantly improved the manual detection of coronary plaques.

The frequent itemset mining algorithm extracted relationships between existing plaques and those plaques that can be predicted with a certain confidence. Various general rules with a confidence above 90% were found, predicting plaques in the LAD given plaques in the segments of the other coronary arteries. At the segment level, rules existed with a confidence between 80-90%, that predicted plaques in the proximal LAD (segment 6) when plaques in different segments of the RCA, LM, or CX were present. The other way round, plaques in these patients involving any artery but not the LAD represents a very rare finding. This altogether indicates, that when a patient with chronic CAD shows plaques, these will primarily develop in the LAD. However, this theory has still to be verified by corresponding studies that track the progress of plaque development and its pattern over time. A possible reason for the observed spatial plaque distribution patterns would be that the geometry of the left coronary artery tree influencing hemodynamic features such as wall shear stress would predispose the development of plaques more than does the geometry of the right coronary artery [Friedman *et al.* 1983]. Another explanation could be a temporal evolution of plaque development, with plaques occurring first in the left coronary tree before developing later also in the right coronary artery system. The lower rate of plaques found in the RCA may also be attributable to the lower image quality in this vessel. As the RCA has larger motion within a cardiac cycle than the left coronary tree [Husmann *et al.* 2007], more blurring might be introduced that lowers the image quality and therefore interferes with the detection of plaques. In this study, prediction rules for mixed plaques were only found with a lower confidence (ranging between 60-70%), and no prediction rules could be defined for soft plaques. This is most probably related to the selected patient population which is known to have a low prevalence for mixed and soft plaques as compared to patients with unstable angina, acute coronary syndromes, or myocardial infarction.

Guided review was introduced as a tool to assist the manual detection of coronary plaques by guiding the reader to specific segments of potentially missed plaques. The method is thereby independent of the underlying applied imaging modality because it only uses knowledge about the segments where plaques have been detected. The plaque detection itself as well as a subsequent classification and quantification of plaques is up to the reader who might get support for this task by additional existing tools and measures for the assessment of plaques. This study investigated the correlation of the spatial plaque distribution with frequent itemset mining expressed in association rules. Those association rules were used for the guided review by indicating segments with possibly missed plaques. The validation by various simulations showed that up-to 47% of the removed plaques could be re-found by reviewing 84 segments, corresponding to only 4.4% of all segments. With the same number of reviewed segments, the weighted random approach revealed only 16% of the removed plaques. As no clear optimum could be determined, a parameter pair for frequent itemset mining was empirically chosen that showed a good trade-off between the number of detected plaques and the number of segments that had to be reviewed for their detection. This parameter pair was then used for the clinical evalu-

ations. In general, it would be preferable to select association rules with higher support values, as a high support value denotes that the association rule was applicable for a large number of observations. Thus, such rules could be regarded as universally valid.

As plaques have a prognostic value being independent of the presence or absence of luminal obstruction [Pundziute *et al.* 2007] they should be consistently detected in each CTCA examination. Atherosclerotic disease is a process that involves various coronary segments [Ehara *et al.* 2004]. The likelihood of co-existing additional segments with potentially symptomatic atherosclerosis has raised the question whether an interventional procedure directed to only one lesion should not tackle others as well. With regard to CTCA, it appears therefore mandatory to identify not only one, presumably obstructing plaque, but all plaques throughout the entire coronary artery tree. This, however, can be difficult because of the lower performance of CT in comparison with the reference standard IVUS. Our study results giving rise to association rules help the interpreting radiologist through directing his review – once a plaque was found – to other coronary segments which are known to have a high probability to contain additional plaques. As shown in the guided review, the association rules that encode observed spatial distribution patterns improve the plaque detection rate for manual labeling.

The association rules as determined in this study may also be implemented in plaque detection software packages for improving their detection rate. Although automatic algorithms for plaque detection have been proposed (see Chapter 4), their detection rates of 74%-85% are still not sufficient for routine clinical applications. In general, these algorithms use intensity-based criteria such that the detection of highly calcified plaques usually poses no problem. On the other hand, weakly calcified and soft plaques are more challenging to detect. Thus, uncertainties may arise whether a slight intensity anomaly might be a plaque or not. When combined with automatic segment labeling of the coronary artery tree (see Chapter 3), the detection algorithms may create additional evidence for the presence or absence of plaques in the uncertain segments by using the prediction rules in combination with the already detected plaques.

In this study, plaque distribution patterns from 252 patients have been learned and applied for the guided review. Considering the number of included patients, it is difficult to estimate an appropriate minimum number of patients for extending the study results to a broader population. At this point, variations in the spatial distribution patterns are not known, such that a power analysis or other approaches are not feasible. As different populations with different clinical presentations show variable plaque type and distribution patterns, corresponding items for the populations and presentations should be created and assigned such that association rules from the respective subgroup can be chosen in the guided review process. The larger number of training data would also allow to investigate possible correlations between cardiovascular risk factors and specific spatial plaque distribution patterns.

7

Summary and Outlook

In the preceding chapters we have discussed various aspects of atherosclerosis assessment. Due to the different nature of these aspects, nearly each chapter was self-contained and provided separate discussions about the achievements and the open issues as well as the possibilities for future research. This chapter will briefly summarize all results and provides a more general discussion and outlook for the assessment of atherosclerosis in coronary arteries.

We started by investigating calcium scoring as it is performed as an initial risk assessment for assessing coronary heart diseases by measuring the amount and volume of calcified plaques in non-enhanced CT images. It is known, that existing calcium scores are subject to high inter-scan variabilities and that they furthermore extremely depend on the selected examination parameters. In general, the main requirements that must be claimed from a calcium score are its robustness and reproducibility against changes in the underlying CT system, the selected examination parameters, and also against variabilities between examinations. Its accuracy in terms of the deviation from the ground truth volume is in our point of view rather of minor importance because with a robust and reproducible score, reliable statistical tables could be established to capture the risk between the score and cardiovascular diseases. Furthermore, a reproducible score would also allow an accurate temporal follow-up of plaque progression or regression, respectively. In Chapter 2 we have therefore proposed an algorithm that is more robust and reproducible by being independent of the selected examination parameters. However, the algorithm has only been evaluated on a cardiac CT phantom such that in a next step, its performance will have to be evaluated on in-vivo studies. Furthermore, potential differences among CT systems from different manufactures were also not considered so far.

After studying calcium scoring which is done on non-enhanced CT images, we moved the focus to the assessment of atherosclerosis in contrast-enhanced CT images in the remaining of the thesis. We first discussed methods for the extraction of anatomical structures in Chapter 3 which were then used for the automatic detection of calcified coronary plaques as discussed in Chapter 4.

Nowadays, plaque assessment is done manually which is error-prone due to inter- and intra-observer variabilities. Therefore, a (semi-)automatic detection is desirable to reduce those variabilities. Previously published methods either focused on the detection of calcified plaques in non-enhanced or in contrast-enhanced images. However, for the latter case in which stenoses are better visible, the injection of contrast agent may cause similar intensities between the vessel lumen and the plaque such that a proper differentiation becomes difficult although the same plaque might be clearly visible in the corresponding non-enhanced CT image. Although non-enhanced CT images are mostly acquired in combination with the contrast-enhanced CT images, existing approaches did not combine the information contained in both data sets for plaque detection. With our proposed framework for the automatic detection of calcified coronary plaques, we considered both the contrast-enhanced and the non-enhanced CT images for the detection and could achieve promising results. In general, besides the detection of plaques and the measurement of their stenotic characteristics, a separation of those plaques into stable and unstable ones is a very important issue of great clinical interest. In order to achieve this separation, characteristics of stable and unstable plaques have to be defined in advance by physicians. Furthermore, it has to be evaluated if CT data provide enough information for this separation or if other techniques have to be incorporated into this process. A potential source for additional information would be computational fluid dynamics (CFD) simulations to model and simulate the development of atherosclerosis based on a given patient's geometry. However, for this, the exact geometry of the coronary tree has to be obtained which in turn requires a good image quality from the CT acquisition for an appropriate segmentation of the coronary arteries. With the latest available CT systems, this is already possible and future developments from CT manufactures will even tend to further decrease the scanning time by either increasing the number of detectors, the table feed, or the rotation speed of the gantry, such that motion artifacts should be further reduced.

Another aspect that should be followed for the assessment of atherosclerosis is the usage of dual energy CT scans for tissue differentiation. In Chapter 5 we have shown the potential of this technique to improve the contrast among tissues targeted for an assessment of atherosclerosis. In general, the achieved contrast enhancement was not extraordinary high which may be caused by the fact that the source spectra of the two selected energy levels were heavily overlapping. It would thus be desirable to use separated spectra such that the varying tissue attenuation characteristics at different energy levels are more pronounced and therefore a better contrast enhancement could be achieved. This can be realized with the newly announced dual energy CT system (SOMATOM Definition Flash, Siemens Healthcare, Germany) where an additional filter truncates part of the spectrum from one X-ray source. Furthermore, this CT systems improves temporal resolution and thus should reduce motion artifacts. However, as this scanner was not yet accessible during the course of this thesis, future work must evaluate the improvements for contrast enhancement with better separated source spectra.

The assessment of atherosclerosis is difficult due to the different types and characteristics of plaques as well as the varying nature of the anatomy. Therefore, each piece of valuable information has to be considered for the diagnosis. Besides an intensity based interpretation of CT data sets as mentioned above, we have investigated spatial plaque distribution patterns in Chapter 6. With our studies, we investigated for the first time dependencies among the distribution of plaques. Based on the learned patterns, a guided review of segments was proposed to support a reader to find potentially missed plaques. For a single reader we showed that guided review made plaque detection more robust. However, we did not apply guided review on the readings of different readers and thus could not evaluate its assumed potential to reduce intra- and inter-observer variability in clinical praxis. Although being developed and evaluated to support the detection of coronary plaques, guided review by frequent itemset mining can also be applied to other arterial beds, for example the carotids. For this, only the definition of the itemset has to be adopted. For guided review, the basis of the itemset was the 16-segment coronary tree of the American Heart Association. In general, there is no restriction on the selection for the items. However, it would be desirable to choose the items for a specific arterial bed according to some recognized model. In doing so, labelings from various centers might be used to learn statistical patterns from a larger set of patients. For an intensive pattern analysis and a widespread application of the learned patterns, a future goal should be the creation of a large database.

To conclude this thesis, we can say that the assessment of atherosclerosis in coronary arteries encompasses many aspects – both medical and technical. In this thesis, we have proposed algorithms and tools to support the manual assessment of atherosclerosis by making it more robust and reproducible. Furthermore, we have developed methods towards an automatic assessment of atherosclerosis. However, there is still a big gap towards the realization of a fully automatic assessment and it has to be considered if this step will ever be feasible due to the manifold of the human anatomy and its possible diseases. Future works should definitively focus on the assessment of noncalcified and mixed plaques as they are more likely to rupture. A possible detection of vulnerable plaques would provide a high prognostic value to physicians for increasingly reliable risk assessment.

Bibliography

[Achenbach *et al.* 2004] S. Achenbach, F. Moselewski, D. Ropers, M. Ferencik, U. Hoffmann, B. MacNeill, K. Pohle, U. Baum, K. Anders, I. Jang, W. Daniel, and T. Brady. Detection of Calcified and Noncalcified Coronary Atherosclerotic Plaque by Contrast-Enhanced, Submillimeter Multidetector Spiral Computed Tomography: A Segment-Based Comparison With Intravascular Ultrasound. *Circulation*, 109(1):14–17, 2004. 5.1

[Adame *et al.* 2004] I. M. Adame, R. J. van der Geest, B. A. Wasserman, M. A. Mohamed, J. H. C. Reiber, and B. P. F. Lelieveldt. Automatic segmentation and plaque characterization in atherosclerotic carotid artery MR images. *Magnetic Resonance Materials in Physics, Biology and Medicine*, 16(5):227–234, April 2004. 4.1.1, 5.1

[Agatston *et al.* 1990] A. Agatston, W. Janowitz, F. Hildner, N. Zusmer, M. Viamonte, and R. Detrano. Quantification of coronary artery calcium using ultrafast computed tomography. *Journal of the American College of Cardiology*, 15(4):827–832, 1990. 2.1.1

[Agrawal *et al.* 1993] R. Agrawal, T. Imielinski, and A. Swami. Mining Association Rules between Sets of Items in Large Databases. In *Proceedings of the ACM SIGMOD International Conference on Management of Data*, pages 207–216, Washington, D.C., 26–28 1993. 6.1.1, 6.2, 6.2.2

[Alderman and Stadius 1992] E. Alderman and M. Stadius. The angiographic definitions of the bypass angioplasty revascularization investigation. *Coronary Artery Disease*, 3:1189–1207, 1992. 1.1.3

[Ali *et al.* 2007] A. Ali, A. Farag, and A. El-Baz. Graph Cuts Framework for Kidney Segmentation with Prior Shape Constraints. In *Medical Image Computing and Computer-Assisted Intervention – MICCAI*, volume 4791 of *LNCS*, pages 384–392. Springer, 2007. 3.3.2

[Alkadhi *et al.* 2008] H. Alkadhi, H. Scheffel, L. Desbiolles, O. Gaemperli, P. Stolzmann, A. Plass, G. Goerres, T. Luescher, M. Genoni, B. Marincek, P. Kaufmann, and S. Leschka. Dual-source computed tomography coronary angiography: influence of obesity, calcium load, and heart rate on diagnostic accuracy. *European Heart Journal*, 29(6):766–776, March 2008. 1.2

[Altman and Bland 1994] D. Altman and J. Bland. Statistics Notes: Diagnostic tests 1: sensitivity and specificity. *BMJ*, 308(6943):1552, June 1994. 5.1

[Anderson *et al.* 2007] R. Anderson, C. Stomberg, C. Hahm, V. Mani, D. Samber, V. Itskovich, L. Valera-Guallar, J. Fallon, P. Nedanov, J. Huizenga, and Z. Fayad. Automated classification of atherosclerotic plaque from magnetic resonance images using predictive models. *Biosystems*, 90(2):456–466, 2007. 5.1

[Asakura and Karino 1990] T. Asakura and T. Karino. Flow patterns and spatial distribution of atherosclerotic lesions in human coronary arteries. *Circulation Research*, 66(4):1045–1066, 1990. 5.4, 6.2.1

[Auer *et al.* 2006] M. Auer, R. Stollberger, P. Regitnig, F. Ebner, and G. Holzapfel. 3-D Reconstruction of Tissue Components for Atherosclerotic Human Arteries Using Ex Vivo High-Resolution MRI. *IEEE Transactions on Medical Imaging*, 25(3):345–357, 2006. 5.1

[Austen *et al.* 1975] W. Austen, J. Edwards, R. Frye, G. Gensini, V. Gott, L. Griffith, D. McGoon, M. Murphy, and B. Roe. A reporting system on patients evaluated for coronary artery disease. *Circulation*, 51:5–40, 1975. 1.1.3, 1.1

[Barrett and Mortensen 1996] W. Barrett and E. Mortensen. Fast, accurate, and reproducible live-wire boundary extraction. *Visualization in Biomedical Computing*, pages 183–192, 1996. 3.2.2

[Barrett and Mortensen 1997] W. Barrett and E. Mortensen. Interactive live-wire boundary extraction. *Medical Image Analysis*, 1(4):331–341, 1997. 3.2.2, 3.2.2

[Bauer and Bischof 2008] C. Bauer and H. Bischof. Edge based tube detection for coronary artery centerline extraction. In *3D Segmentation in the Clinic: A Grand Challenge II: MICCAI workshop proceedings*, 2008. 3.2.1

[Beckman *et al.* 2001] J. Beckman, J. Ganz, M. Creager, P. Ganz, and S. Kinlay. Relationship of clinical presentation and calcification of culprit coronary artery stenoses. *Arterioscler Thromb Vasc Biol*, 21(10):1618–1622, Oct 2001. 6.1.1

[Behrendt *et al.* 2009] F. Behrendt, B. Schmidt, C. Plumhans, S. Keil, S. Woodruff, D. Ackermann, G. Mühlenbruch, T. Flohr, R. Günther, and A. Mahnken. Image Fusion in Dual Energy Computed Tomography: Effect on Contrast Enhancement, Signal-to-Noise Ratio and Image Quality in Computed Tomography Angiography. *Investigative Radiology*, 44:1–6, 2009. 5.1.1, 5.4

[Berger and Hubbell 1987] M. Berger and J. Hubbell. XCOM: Photon Cross Sections on a Personal Computer. Technical Report NBSIR 87-3597, National Bureau of Standards Internal Report, 1987. 1.3.4, 2.2.3, 5.2.2

[Birnbaum *et al.* 2007] B. Birnbaum, N. Hindman, J. Lee, and J. Babb. Multi-Detector Row CT Attenuation Measurements: Assessment of Intra- and Interscanner Variability with an Anthropomorphic Body CT Phantom. *Radiology*, 242(1):109–119, 2007. 2.2.1

[Bock *et al.* 2008] S. Bock, C. Kühnel, T. Boskamp, and H.-O. Peitgen. Robust vessel segmentation. In *Medical Imaging: Computer-Aided Diagnosis*, volume 6915, page 691539. SPIE, 2008. 3.3.1, 3.5

[Boll *et al.* 2006] D. Boll, M. Hoffmann, N. Huber, A. Bossert, A. Aschoff, and T. Fleiter. Spectral Coronary Multidetector Computed Tomography Angiography: Dual Benefit

by Facilitating Plaque Characterization and Enhancing Lumen Depiction. *Journal of Computer Assisted Tomography*, 30(5):804–811, 2006. 5.1.1

[Boone 2001] J. Boone. Determination of the presampled MTF in computed tomography. *Medical Physics*, 28(3):356–360, 2001. 3

[Borgelt and Kruse 2002] C. Borgelt and R. Kruse. Induction of association rules: A priori implementation. In *15th Conference on Computational Statistics, Compstat*, 2002. 6.2.2, 6.2.2

[Boskamp *et al.* 2004] T. Boskamp, D. Rinck, F. Link, B. Kümmerlen, G. Stamm, and P. Mildenberger. New Vessel Analysis Tool for Morphometric Quantification and Visualization of Vessels in CT and MR Imaging Data Sets. *Radiographics*, 24(1):287–297, 2004. 3.3.1

[Bouraoui *et al.* 2008] B. Bouraoui, C. Ronse, J. Baruthio, N. Passat, and P. Germain. Fully automatic 3D segmentation of coronary arteries based on mathematical morphology. In *Fifth IEEE International Symposium on Biomedical Imaging: From Nano to Macro, ISBI*, pages 1059–1062, 2008. 3.1.1, 3.3.1

[Boykov and Funka-Lea 2006] Y. Boykov and G. Funka-Lea. Graph Cuts and Efficient N-D Image Segmentation. *International Journal of Computer Vision*, 70(2):109–131, 2006. 3.3.2

[Boykov and Jolly 2001] Y. Boykov and M.-P. Jolly. Interactive Graph Cuts for Optimal Boundary & Region Segmentation of Objects in N-D Images. In *Eighth IEEE International Conference on Computer Vision, ICCV*, pages 105–112 vol.1, 2001. 3.3.2

[Boykov and Kolmogorov 2004] Y. Boykov and V. Kolmogorov. An experimental comparison of min-cut/max- flow algorithms for energy minimization in vision. *IEEE Transactions on Pattern Analysis and Machine Intelligence*, 26(9):1124–1137, 2004. 3.3.2

[Boykov *et al.* 2001] Y. Boykov, O. Veksler, and R. Zabih. Fast approximate energy minimization via graph cuts. *Pattern Analysis and Machine Intelligence, IEEE Transactions on*, 23(11):1222–1239, 2001. 3.3.2, 3.3.2

[Brodoefel *et al.* 2008] H. Brodoefel, A. Reimann, M. Heuschmid, I. Tsiflikas, A. Kopp, S. Schroeder, C. Claussen, M. Clouse, and C. Burgstahler. Characterization of coronary atherosclerosis by dual-source computed tomography and HU-based color mapping: a pilot study. *European Radiology*, 18(11):2466–2474, 2008. 1.3.4

[Brown *et al.* 2008] E. Brown, R. Kronmal, D. Bluemke, A. Guerci, J. Carr, J. Goldin, and R. Detrano. Coronary Calcium Coverage Score: Determination, Correlates, and Predictive Accuracy in the Multi-Ethnic Study of Atherosclerosis. *Radiology*, 247(3):669–675, 2008. 2.1.4

[Bruijns 2001] J. Bruijns. Fully-Automatic Branch Labelling of Voxel Vessel Structures. In *Proceedings of the Vision Modeling and Visualization Conference*, pages 341–350, 2001. 3.3.1

[Brunner *et al.* 2008] G. Brunner, U. Kurkure, D. Chittajallu, R. Yalamanchili, and I. Kakadiaris. Toward unsupervised classification of calcified arterial lesions. *Medi-*

cal Image Computing and Computer-Assisted Intervention - MICCAI, pages 144–152, 2008. 4.1.1, 4.4

[Bühler *et al.* 2003] K. Bühler, P. Felkel, and A. La Cruz. Geometric Methods for Vessel Visualization and Quantification - A Survey. In *Geometric Modelling for Scientific Visualization*. Springer, 2003. 3.3.1

[Cademartiri *et al.* 2006] F. Cademartiri, L. La Grutta, A. Palumbo, E. Maffei, G. Runza, T. Bartolotta, F. Pugliese, N. Mollet, M. Midiri, and G. Krestin. Coronary plaque imaging with multislice computed tomography: technique and clinical applications. *European Radiology*, 16 Suppl 7:M44–M53, 2006. 4

[Cademartiri *et al.* 2007] F. Cademartiri, L. La Grutta, G. Runza, A. Palumbo, E. Maffei, N. Mollet, T. Bartolotta, P. Somers, M. Knaapen, S. Verheye, M. Midiri, R. Hamers, and N. Bruining. Influence of convolution filtering on coronary plaque attenuation values: observations in an ex vivo model of multislice computed tomography coronary angiography. *European Radiology*, 17(7):1842–1849, 2007. 2.2.1, 2.6

[Cademartiri *et al.* 2008] F. Cademartiri, L. La Grutta, R. Malagò, F. Alberghina, W. Meijboom, F. Pugliese, E. Maffei, A. Palumbo, A. Aldrovandi, M. Fusaro, V. Brambilla, P. Coruzzi, M. Midiri, N. Mollet, and G. Krestin. Prevalence of anatomical variants and coronary anomalies in 543 consecutive patients studied with 64-slice CT coronary angiography. *European Radiology*, 18(4):781–791, 2008. 1.1.2, 3.4

[Callister *et al.* 1998] T. Callister, B. Cooil, S. Raya, N. Lippolis, D. Russo, and P. Raggi. Coronary artery disease: improved reproducibility of calcium scoring with an electron-beam CT volumetric method. *Radiology*, 208(3):807–814, 1998. 2.1.2

[Carrascosa *et al.* 2003] P. Carrascosa, C. Capunay, J. Parodi, L. Padilla, P. Johnson, J. Carrascosa, S. Chandra, D. Smith, and J. Belardi. General Utilities of Multislice Tomography in the Cardiac Field. *Herz*, 28(1):44–51, 2003. 1.3.4

[Carrillo *et al.* 2007] J. Carrillo, M. Hoyos, E. Davila, and M. Orkisz. Recursive tracking of vascular tree axes in 3D medical images. *International Journal of Computer Assisted Radiology and Surgery*, 1(6):331–339, 2007. 3.2.1

[Castro *et al.* 2008] C. Castro, M. Luengo-Oroz, A. Santos, and M. Ledesma-Carbayo. Coronary Artery Tracking in 3D Cardiac CT Images Using Local Morphological Reconstruction Operators. In *3D Segmentation in the Clinic: A Grand Challenge II: MICCAI workshop proceedings*, 2008. 3.2.1

[Catalano and Passariello 2005] C. Catalano and R. Passariello, editors. *Multidetector-Row CT Angiography*. Springer Berlin Heidelberg, 2005. 1.3.4

[Chalopin *et al.* 1998] C. Chalopin, I. Magnin, and G. Finet. Automatic labeling of the coronary tree using a three dimensional reference prior model. In *Computers in Cardiology*, pages 761–764, 1998. 3.4.1

[Chalopin *et al.* 2001] C. Chalopin, G. Finet, and I. Magnin. Modeling the 3D coronary tree for labeling purposes. *Medical Image Analysis*, 5(4):301–315, 2001. 3.4.1, 3.4.2

[Chen and Chen 2006] Q. Chen and Y.-P. Chen. Mining frequent patterns for AMP-activated protein kinase regulation on skeletal muscle. *BMC Bioinformatics*, 7:394, 2006. 6.1.1

[Chen *et al.* 2005] Z. Chen, R. Ning, D. Conover, Y. Yu, and X. Lu. Dual-basis-material decomposition for dual-kvp cone-beam CT breast imaging. volume 5745, pages 1322–1333. SPIE, 2005. 5.1.1

[Cheruvu *et al.* 2007] P. Cheruvu, A. Finn, C. Gardner, J. Caplan, J. Goldstein, G. Stone, R. Virmani, and J. Muller. Frequency and Distribution of Thin-Cap Fibroatheroma and Ruptured Plaques in Human Coronary Arteries: A Pathologic Study. *Journal of the American College of Cardiology*, 50(10):940–949, 2007. 6.1.1

[Chiro *et al.* 1979] G. D. Chiro, R. A. Brooks, R. M. Kessler, G. S. Johnston, A. E. Jones, J. R. Herdt, and W. T. Sheridan. Tissue signatures with dual-energy computed tomography. *Radiology*, 131(2):521–523, May 1979. 5.1.1

[Cormen *et al.* 2001] T. Cormen, C. Leiserson, R. Rivest, and C. Stein. *Introduction to Algorithms, Second Edition*. McGraw-Hill Science/Engineering/Math, July 2001. 3.3.2, 3.3.2

[Costa *et al.* 2007] M. Costa, M. Sabate, R. Staico, F. Alfonso, A. Seixas, M. Albertal, A. Crossman, D. Angiolillo, M. Zenni, J. E. Sousa, C. Macaya, and T. Bass. Anatomical and physiologic assessments in patients with small coronary artery disease: Final results of the Physiologic and Anatomical Evaluation Prior to and After Stent Implantation in Small Coronary Vessels (PHANTOM) trial. *American Heart Journal*, 153(2):296.e1–296.e7, 2007. 1.3.2

[Couturier *et al.* 2004] O. Couturier, H. Delalin, H. Fu, G. Edouard, Kouamou, and E. Mephu-Nguifo. A three-step approach for STULONG database analysis: characterization of patients' groups. In *Proceedings of the 9th European Conference on Machine Learning*, 2004. 6.1.1

[Dehmeshki *et al.* 2007] J. Dehmeshki, X. Ye, H. Amin, M. Abaei, X. Lin, and S. D. Qanadli. Volumetric Quantification of Atherosclerotic Plaque in CT Considering Partial Volume Effect. *IEEE Transactions on Medical Imaging*, 26(3):273–282, 2007. 2.1.4

[del Rio and Dejus 1998] M. del Rio and R. J. Dejus. XOP: Recent developments. In *SPIE proceedings 3448*, 1998. 5.2.2

[Dijkstra 1959] E. Dijkstra. A note on two problems in connexion with graphs. *Numerische Mathematik*, 1:269–271, 1959. 3.2.2

[Dikici *et al.* 2008] E. Dikici, T. O'Donnell, L. Grady, R. Setser, and R. White. Coronary artery centerline tracking using axial symmetries. In *3D Segmentation in the Clinic: A Grand Challenge II: MICCAI workshop proceedings*, 2008. 3.2.1

[Dodge *et al.* 1988] J. Dodge, B. Brown, E. Bolson, and H. Dodge. Intrathoracic spatial location of specified coronary segments on the normal human heart. Applications in quantitative arteriography, assessment of regional risk and contraction, and anatomic display. *Circulation*, 78(5):1167–1180, 1988. 3.3.2, 3.4.2

[Dodge *et al.* 1992] J. Dodge, B. Brown, E. Bolson, and H. Dodge. Lumen diameter of normal human coronary arteries. Influence of age, sex, anatomic variation, and left ventricular hypertrophy or dilation. *Circulation*, 86(1):232–246, 1992. 3.3.2, 3.4.2

[Dumay *et al.* 1994] A. Dumay, J. Gerbrands, and J. Reiber. Automated extraction, labelling and analysis of the coronary vasculature from arteriograms. *The International Journal of Cardiac Imaging*, 10(3):205–215, 1994. 3.4.1

[Ehara *et al.* 2004] S. Ehara, Y. Kobayashi, M. Yoshiyama, K. Shimada, Y. Shimada, D. Fukuda, Y. Nakamura, H. Yamashita, H. Yamagishi, K. Takeuchi, T. Naruko, K. Haze, A. Becker, J. Yoshikawa, and M. Ueda. Spotty Calcification Typifies the Culprit Plaque in Patients With Acute Myocardial Infarction: An Intravascular Ultrasound Study. *Circulation*, 110(22):3424–3429, 2004. 6.1.1, 6.4

[El Harchaoui *et al.* 2009] K. El Harchaoui, B. J. Arsenault, R. Franssen, J. Despres, G. Hovingh, E. Stroes, J. Otvos, N. Wareham, J. Kastelein, K.-T. Khaw, and S. Boekholdt. High-density lipoprotein particle size and concentration and coronary risk. *Ann Intern Med*, 150(2):84–93, 2009. 1.2.2

[Estes *et al.* 1998] J. Estes, W. Quist, F. Lo Gerfo, and P. Costello. Noninvasive characterization of plaque morphology using helical computed tomography. *Journal of Cardiovascular Surgery*, 39(5):527–534, 1998. 1.3.4

[Eusemann *et al.* 2008] C. Eusemann, D. Holmes III, B. Schmidt, T. Flohr, R. Robb, C. McCollough, D. Hough, J. Huprich, M. Wittmer, H. Siddiki, and J. Fletcher. Dual energy CT: How to best blend both energies in one fused image? In *Proc. SPIE Int. Soc. Opt. Eng.*, volume 6918, pages 691803–8, 2008. 5.1.1, 5.4

[Ezquerra *et al.* 1998] N. Ezquerra, S. Capell, L. Klein, and P. Duijves. Model-guided labeling of coronary structure. *IEEE Transactions on Medical Imaging*, 17(3):429–441, 1998. 3.4.1

[Falcao *et al.* 1998] A. Falcao, J. Udupa, S. Samarasekera, S. Sharma, B. Hirsch, and R. Lotufo. User-Steered Image Segmentation Paradigms: Live Wire and Live Lane. *Graphical Models and Image Processing*, 60(4):233–260, 1998. 3.2.2

[Falcao *et al.* 1999] A. Falcao, J. Udupa, and F. Miyazawa. Ultrafast user-steered image segmentation paradigm: live-wire-on-the-fly. In *Proc. SPIE*, volume 3661, pages 184–191, 1999. 3.2.2

[Falcao *et al.* 2000] A. Falcao, J. Udupa, and F. Miyazawa. An ultra-fast user-steered image segmentation paradigm: live wire on the fly. *IEEE Transactions on Medical Imaging*, 19(1):55–62, 2000. 3.2.2

[Faller and Schünke 2004] A. Faller and M. Schünke. *The Human Body*. Thieme, 2004. 1.1

[Fauci *et al.* 2008] A. Fauci, D. Kasper, D. Longo, E. Braunwald, S. Hauser, and J. Jameson. *Harrison's principles of internal medicine.* Mcgraw-Hill Professional, 2008. 1.3.1

[Felkel *et al.* 2001] P. Felkel, R. Wegenkittl, and A. Kanitsar. Vessel Tracking in Peripheral CTA Datasets - An Overview. In *Spring Conference on Computer Graphics*, pages 232–239, 2001. 3.2.1

[Flohr *et al.* 2005] T. Flohr, S. Schaller, K. Stierstorfer, H. Bruder, B. Ohnesorge, and U. Schoepf. Multi-Detector Row CT Systems and Image-Reconstruction Techniques. *Radiology*, 235(3):756–773, 2005. 1.3.4

[Flohr *et al.* 2006] T. Flohr, C. McCollough, H. Bruder, M. Petersilka, K. Gruber, C. Süß, M. Grasruck, K. Stierstorfer, B. Krauss, R. Raupach, A. Primak, A. Küttner, S. Achenbach, C. Becker, A. Kopp, and B. Ohnesorge. First performance evaluation of a dual-source CT (DSCT) system. *European Radiology*, 16(2):256–268, 2006. 2.4.2, 5.1, 5.1.1

[Florin *et al.* 2006] C. Florin, N. Paragios, and J. Williams. Globally Optimal Active Contours, Sequential Monte Carlo and On-Line Learning for Vessel Segmentation. In *Computer Vision – ECCV*, volume 3953 of *LNCS*, pages 476–489, 2006. 3.3.1

[Frangi *et al.* 2000] A. Frangi, W. Niessen, P. Nederkoorn, O. Elgersma, and M. Viergever. Three-dimensional model-based stenosis quantification of the carotid arteries from contrast-enhanced MR angiography. In W. Niessen, editor, *IEEE Workshop on Mathematical Methods in Biomedical Image Analysis*, pages 110–118, 2000. 3.2.1, 4.1.1

[Freund and Schapire 1995] Y. Freund and R. Schapire. A decision-theoretic generalization of on-line learning and an application to boosting. In *Proceedings of the Second European Conference on Computational Learning Theory*, pages 23–37, 1995. 4.1.1

[Friedman *et al.* 1983] M. Friedman, O. Deters, F. Mark, C. Brent Bargeron, and G. Hutchins. Arterial geometry affects hemodynamics : A potential risk factor for atherosclerosis. *Atherosclerosis*, 46(2):225–231, February 1983. 6.4

[Friman *et al.* 2008a] O. Friman, M. Hindennach, and H.-O. Peitgen. Template-based multiple hypotheses tracking of small vessels. In *Fifth IEEE International Symposium on Biomedical Imaging: From Nano to Macro, ISBI*, pages 1047–1050, 2008. 3.2.1, 3.3.1

[Friman *et al.* 2008b] O. Friman, C. Kühnel, and H.-O. Peitgen. Coronary Centerline Extraction Using Multiple Hypothesis Tracking and Minimal Paths. In *3D Segmentation in the Clinic: A Grand Challenge II: MICCAI 2008 workshop proceedings*, 2008. 3.2.1

[Fritz *et al.* 2008] D. Fritz, A. Wiedemann, R. Dillmann, and M. Scheuering. Fully automatic detection and visualization of patient specific coronary supply regions. In *Proc. SPIE Int. Soc. Opt. Eng.*, volume 6916, pages 691602–9, 2008. 3.1.1, 3.4.1, 3.5

[Fujii *et al.* 2005] K. Fujii, S. Carlier, G. Mintz, H. Takebayashi, T. Yasuda, R. Costa, I. Moussa, G. Dangas, R. Mehran, and A. Lansky. Intravascular Ultrasound Study of Patterns of Calcium in Ruptured Coronary Plaques. *The American Journal of Cardiology*, 96(3):352–357, 2005. 6.1.1

[Fürnstahl *et al.* 2008] P. Fürnstahl, T. Fuchs, A. Schweizer, L. Nagy, G. Székely, and M. Harders. Automatic and robust forearm segmentation using graph cuts. In *Fifth IEEE International Symposium on Biomedical Imaging: From Nano to Macro, ISBI*, pages 77–80, 2008. 3.3.2

[Garreau *et al.* 1991] M. Garreau, J. Coatrieux, R. Collorec, and C. Chardenon. A knowledge-based approach for 3-D reconstruction and labeling of vascular networks from biplane angiographic projections. *IEEE Transactions on Medical Imaging*, 10(2):122–131, 1991. 3.4.1

[Genant and Boyd 1977] H. K. Genant and D. Boyd. Quantitative bone mineral analysis using dual energy computed tomography. *Investigative Radiology*, 12(6):545–551, 1977. 5.1.1

[Glagov *et al.* 1987] S. Glagov, E. Weisenberg, C. Zarins, R. Stankunavicius, and G. Kolettis. Compensatory enlargement of human atherosclerotic coronary arteries. *New England Journal of Medicine*, 316(22):1371–1375, 1987. 3.3

[Goel *et al.* 2008] V. Goel, R. Greenberg, and D. Greenberg. Automated vascular geometric analysis of aortic aneurysms. *IEEE Computer Graphics and Applications*, 28(3):76–86, 2008. 3.2.1

[Goo *et al.* 2008] H. Goo, E. Chae, J. Seo, and S.-J. Hong. Xenon ventilation CT using a dual-source dual-energy technique: dynamic ventilation abnormality in a child with bronchial atresia. *Pediatric Radiology*, 38(10):1113–1116, 2008. 5.1.1

[Grahne and Zhu 2003] G. Grahne and J. Zhu. Efficiently Using Prefix-trees in Mining Frequent Itemsets. In *International Workshop on Frequent Itemset Mining Implementations*, 2003. 6.1.1

[Graser *et al.* 2008] A. Graser, T. Johnson, M. Bader, M. Staehler, N. Haseke, K. Nikolaou, M. Reiser, C. Stief, and C. Becker. Dual energy CT characterization of urinary calculi: Initial in vitro and clinical experience. *Investigative Radiology*, 43:112–119, 2008. 5.1.1

[Graser *et al.* 2009] A. Graser, T. Johnson, H. Chandarana, and M. Macari. Dual energy CT: preliminary observations and potential clinical applications in the abdomen. *European Radiology*, 19:13–23, 2009. 5.1.1, 5.1.1

[Gülsün and Tek 2008] M. Gülsün and H. Tek. Robust vessel tree modeling. *Medical Image Computing and Computer-Assisted Intervention - MICCAI*, pages 602–611, 2008. 3.2.1

[Hall *et al.* 1997] P. Hall, M. Ngan, and P. Andreae. Reconstruction of vascular networks using three-dimensional models. *IEEE Transactions on Medical Imaging*, 16(6):919–929, 1997. 3.4.1

[Halliburton *et al.* 2005] S. S. Halliburton, A. E. Stillman, M. Lieber, J. M. Kasper, S. A. Kuzmiak, and R. D. White. Potential Clinical Impact of Variability in the Measurement of Coronary Artery Calcification with Sequential MDCT. *American Journal of Roentgenology*, 184(2):643–648, 2005. 2.2

[Han *et al.* 2000] J. Han, J. Pei, and Y. Yin. Mining frequent patterns without candidate generation. In *Proceedings of the ACM SIGMOD international conference on Management of data*, pages 1–12, 2000. 6.1.1

[Haris *et al.* 1999] K. Haris, S. Efstratiadis, N. Maglaveras, C. Pappas, J. Gourassas, and G. Louridas. Model-based morphological segmentation and labeling of coronaryangiograms. *IEEE Transactions on Medical Imaging*, 18(10):1003–1015, 1999. 3.4.1

[Hausleiter *et al.* 2006] J. Hausleiter, T. Meyer, M. Hadamitzky, A. Kastrati, S. Martinoff, and A. Schomig. Prevalence of Noncalcified Coronary Plaques by 64-Slice Computed Tomography in Patients With an Intermediate Risk for Significant Coronary Artery Disease. *Journal of the American College of Cardiology*, 48:312–318, 2006. 6.1.1

[Hein *et al.* 2007] P. Hein, J. Mews, and P. Rogalla. Cardiac MSCT Study Assessment with Sure Plaque-Software. *Toshiba Medial Systems Journal - Visions*, 2:22–26, 2007. 1.3.4

[Heismann and Mahnken 2006] B. Heismann and A. Mahnken. Quantitative CT characterization of body fluids with spectral ρZ projection method. In *IEEE Nuclear Science Symposium Conference*, volume 4, pages 2079–2080, 2006. 5.1.1

[Heismann *et al.* 2003] B. Heismann, J. Leppert, and K. Stierstorfer. Density and atomic number measurements with spectral x-ray attenuation method. *Journal of Applied Physics*, 94(3):2073–2079, 2003. 5.1.1, 5.2.2

[Hennemuth *et al.* 2005] A. Hennemuth, T. Boskamp, D. Fritz, C. Kühnel, S. Bock, D. Rinck, M. Scheuering, and H.-O. Peitgen. One-click coronary tree segmentation in CT angiographic images. *International Congress Series*, 1281:317–321, 2005. 3.5

[Hiro *et al.* 1997] T. Hiro, C. Y. Leung, S. Guzman, V. Caiozzo, A. Farvid, H. Karimi, R. Helfant, and J. Tobis. Are soft echoes really soft? Intravascular ultrasound assessment of mechanical properties in human atherosclerotic tissue. *American Heart Journal*, 133(1):1–7, 1997. 1.3.2

[Hoff *et al.* 2003] J. Hoff, M. Daviglus, E. Chomka, A. Krainik, A. Sevrukov, and G. Kondos. Conventional Coronary Artery Disease Risk Factors and Coronary Artery Calcium Detected by Electron Beam Tomography in 30,908 Healthy Individuals. *Annals of Epidemiology*, 13(3):163–169, 2003. 2.1.1

[Hoffmann *et al.* 2008] H. Hoffmann, K. Frieler, B. Hamm, and M. Dewey. Intra- and interobserver variability in detection and assessment of calcified and noncalcified coronary artery plaques using 64-slice computed tomography. *The International Journal of Cardiovascular Imaging (formerly Cardiac Imaging)*, 24(7):735–742, 2008. 4

[Holmes III *et al.* 2008] D. Holmes III, J. Fletcher, A. Apel, J. Huprich, H. Siddiki, D. Hough, B. Schmidt, T. Flohr, R. Robb, C. McCollough, M. Wittmer, and C. Eusemann. Evaluation of non-linear blending in dual-energy computed tomography. *European Journal of Radiology*, 68(3):409–413, 2008. 5.1.1, 5.3

[Holtzman-Gazit *et al.* 2006] M. Holtzman-Gazit, R. Kimmel, N. Peled, and D. Goldsher. Segmentation of Thin Structures in Volumetric Medical Images. *IEEE Transactions on Image Processing*, 15(2):354–363, 2006. 3.3.1

[Hong *et al.* 2002] C. Hong, C. Becker, U. Schoepf, B. Ohnesorge, R. Bruening, and M. Reiser. Coronary Artery Calcium: Absolute Quantification in Nonenhanced and

Contrast-enhanced Multi-Detector Row CT Studies. *Radiology*, 223(2):474–480, 2002. 2.1.3, 2.4.1, 2.5

[Hong *et al.* 2003] C. Hong, K. Bae, and T. Pilgram. Coronary Artery Calcium: Accuracy and Reproducibility of Measurements with Multi-Detector Row CT - Assessment of Effects of Different Thresholds and Quantification Methods. *Radiology*, 227(3):795–801, 2003. 2.1.1, 2.2, 2.2.2, 2.4.1, 2.5

[Hong *et al.* 2007] M.-K. Hong, G. Mintz, C. Lee, K.-M. Park, B.-K. Lee, Y.-H. Kim, D.-H. Kang, S.-S. Cheong, J.-K. Song, and J.-J. Kim. Plaque ruptures in stable angina pectoris compared with acute coronary syndrome. *International Journal of Cardiology*, 114:78–82, 2007. 6.1.1

[Horn 1987] B. K. P. Horn. Closed-form solution of absolute orientation using unit quaternions. *Journal of the Optical Society of America*, 4:629–642, 1987. 4.2

[Hough 1962] P. Hough. Method and means for recognizing complex patterns, 1962. Patent No 3069654. 3.1.1

[Hoyos *et al.* 2008] M. Hoyos, M. Zuluaga, M. Lozano, J. Prieto, P. Douek, I. Magnin, and M. Orkisz. Coronary centerline tracking in CT images with use of an elastic model and image moments. In *3D Segmentation in the Clinic: A Grand Challenge II: MICCAI workshop proceedings*, 2008. 3.2.1

[Huang *et al.* 2007] Y. Huang, H. Li, H. Hu, X. Yan, M. Waterman, H. Huang, and X. Zhou. Systematic discovery of functional modules and context-specific functional annotation of human genome. *Bioinformatics*, 23(13):i222–i229, 2007. 6.1.1

[Husmann *et al.* 2007] L. Husmann, S. Leschka, L. Desbiolles, T. Schepis, O. Gaemperli, B. Seifert, P. Cattin, T. Frauenfelder, T. Flohr, B. Marincek, P. Kaufmann, and H. Alkadhi. Coronary Artery Motion and Cardiac Phases: Dependency on Heart Rate Implications for CT Image Reconstruction. *Radiology*, 245(2):567–576, November 2007. 6.4

[Hyafil *et al.* 2007] F. Hyafil, J.-C. Cornily, J. Feig, R. Gordon, E. Vucic, V. Amirbekian, E. Fisher, V. Fuster, L. Feldman, and Z. Fayad. Noninvasive detection of macrophages using a nanoparticulate contrast agent for computed tomography. *Nature Medicine*, 13(5):636–641, 2007. 5.4

[International Commission on Radiation Units and Measurements 1989] International Commission on Radiation Units and Measurements. Tissue substitutes in radiation dosimetry and measurement. *ICRU Report 44*, 1989. 5.1

[Išgum *et al.* 2003] I. Išgum, B. van Ginneken, and M. Viergever. Automatic detection of calcifications in the aorta from abdominal CT scans. In *Computer-Assisted Radiology and Surgery*, volume 1256 of *International Congress Series*, pages 1037–1042, 2003. 4.1.1

[Išgum *et al.* 2004] I. Išgum, B. van Ginneken, and M. Prokop. A pattern recognition approach to automated coronary calcium scoring. In *Proceedings of the 17th International Conference on Pattern Recognition*, pages 746–749 Vol.3, 2004. 4.1.1

[Išgum *et al.* 2005] I. Išgum, B. van Ginneken, A. Rutten, and M. Prokop. Automated coronary calcification detection and scoring. In *Proceedings of the 4th International Symposium on Image and Signal Processing and Analysis*, pages 127–132, 2005. 4.1.1

[Išgum *et al.* 2007] I. Išgum, A. Rutten, M. Prokop, and B. van Ginneken. Detection of coronary calcifications from computed tomography scans for automated risk assessment of coronary artery disease. *Medical Physics*, 34(4):1450–1461, 2007. 4.1.1, 4.4

[Johnson *et al.* 2007] T. Johnson, B. Krauß, M. Sedlmair, M. Grasruck, H. Bruder, D. Morhard, C. Fink, S. Weckbach, M. Lenhard, B. Schmidt, T. Flohr, M. Reiser, and C. Becker. Material differentiation by dual energy CT: initial experience. *European Radiology*, 17(6):1510–1517, June 2007. 5.1.1, 5.3

[Jones *et al.* 2003] A. K. Jones, D. E. Hintenlang, and W. E. Bolch. Tissue-equivalent materials for construction of tomographic dosimetry phantoms in pediatric radiology. *Medical Physics*, 30(8):2072–2081, 2003. 5.1

[Jougla 2003] E. Jougla. *Health Statistics - Atlas on mortality in the European Union*. European Communities, 2003. 1

[Kanitsar 2001] A. Kanitsar. Advanced visualization techniques for vessel investigation. Master's thesis, TU Wien, 2001. 3.2.2

[Katouzian *et al.* 2008] A. Katouzian, B. Baseri, E. Konofagou, and A. Laine. Texture-driven coronary artery plaque characterization using wavelet packet signatures. In *Fifth IEEE International Symposium on Biomedical Imaging: From Nano to Macro, ISBI*, pages 197–200, 2008. 5.1

[Kelcz *et al.* 1979] F. Kelcz, P. Joseph, and S. Hilal. Noise considerations in dual energy CT scanning. *Medical Physics*, 6(5):418–425, 1979. 5.1.1

[Kerwin *et al.* 2001] W. Kerwin, C. Han, B. Chu, D. Xu, Y. Luo, J.-N. Hwang, T. Hatsukami, and C. Yuan. A Quantitative Vascular Analysis System for Evaluation of Atherosclerotic Lesions by MRI. In *Medical Image Computing and Computer-Assisted Intervention - MICCAI*, pages 786–794, 2001. 5.1

[Kimme *et al.* 1975] C. Kimme, D. Ballard, and J. Sklansky. Finding circles by an array of accumulators. *Communications of the ACM*, 18(2):120–122, 1975. 3.1.1

[Kirbas and Quek 2004] C. Kirbas and F. Quek. A review of vessel extraction techniques and algorithms. *ACM Computing Surveys*, 36(2):81–121, 2004. 3.3.1

[Kitslaar *et al.* 2008] P. Kitslaar, M. Frenay, E. Oost, J. Dijkstra, B. Stoel, and J. Reiber. Connected Component and Morphology Based Extraction of Arterial Centerlines of the Heart (CocomoBeach). In *3D Segmentation in the Clinic: A Grand Challenge II: MICCAI workshop proceedings*, 2008. 3.2.1

[Kolmogorov and Zabin 2004] V. Kolmogorov and R. Zabin. What energy functions can be minimized via graph cuts? *IEEE Transactions on Pattern Analysis and Machine Intelligence*, 26(2):147–159, 2004. 3.3.2, 3.3.2

[Komatsu *et al.* 2005] S. Komatsu, A. Hirayama, Y. Omori, Y. Ueda, I. Mizote, Y. Fujisawa, M. Kiyomoto, T. Higashide, and K. Kodama. Detection of Coronary Plaque

by Computed Tomography With a Novel Plaque Analysis System, 'Plaque Map', and Comparison With Intravascular Ultrasound and Angioscopy. *Circulation Journal*, 69(1):72–77, 2005. 4.1.1

[Kopp *et al.* 2002] A. Kopp, B. Ohnesorge, C. Becker, S. Schröder, M. Heuschmid, A. Küttner, R. Kuzo, and C. Claussen. Reproducibility and Accuracy of Coronary Calcium Measurements with Multi-Detector Row versus electron-beam CT. *Radiology*, 225(1):113–119, 2002. 2.2

[Kovacs *et al.* 2006] T. Kovacs, P. Cattin, H. Alkadhi, S. Wildermuth, and G. Székely. Automatic Segmentation of the Vessel Lumen from 3D CTA Images of Aortic Dissection. In *Bildverarbeitung für die Medizin*, pages 161–5, 2006. 3.1.1

[Krissian *et al.* 2008] K. Krissian, H. Bogunovic, J. Pozo, M. Villa-Uriol, and A. Frangi. Minimally Interactive Knowledge-based Coronary Tracking in CTA using a Minimal Cost Path. In *3D Segmentation in the Clinic: A Grand Challenge II: MICCAI workshop proceedings*, 2008. 3.2.1

[Kurkure *et al.* 2008a] U. Kurkure, O. Avila-Montes, and I. Kakadiaris. Automated segmentation of thoracic aorta in non-contrast CT images. In *Biomedical Imaging: From Nano to Macro, 2008. ISBI 2008. 5th IEEE International Symposium on*, pages 29–32, 2008. 3.1.1

[Kurkure *et al.* 2008b] U. Kurkure, D. Chittajallu, G. Brunner, R. Yalamanchili, and I. Kakadiaris. Detection of Coronary Calcifications Using Supervised Hierarchical Classification. In *Proc. of 2nd MICCAI Workshop on Computer Vision for Intravascular and Intracardiac Imaging*, 2008. 4.1.1, 4.4

[Law and Chung 2007] M. W. K. Law and A. C. S. Chung. Weighted Local Variance-Based Edge Detection and Its Application to Vascular Segmentation in Magnetic Resonance Angiography. *IEEE Transactions on Medical Imaging*, 26(9):1224–1241, 2007. 3.3.1

[Leber *et al.* 2004] A. Leber, A. Knez, A. Becker, C. Becker, F. von Ziegler, K. Nikolaou, C. Rist, M. Reiser, C. White, G. Steinbeck, and P. Boekstegers. Accuracy of multidetector spiral computed tomography in identifying and differentiating the composition of coronary atherosclerotic plaques: A comparative study with intracoronary ultrasound. *Journal of the American College of Cardiology*, 43(7):1241–1247, 2004. 1.3.4, 1.3.4, 5.1

[Leber *et al.* 2006] A. Leber, A. Becker, A. Knez, F. von Ziegler, M. Sirol, K. Nikolaou, B. Ohnesorge, Z. Fayad, C. Becker, and M. Reiser. Accuracy of 64-Slice Computed Tomography to Classify and Quantify Plaque Volumes in the Proximal Coronary System: A Comparative Study Using Intravascular Ultrasound. *Journal of the American College of Cardiology*, 47:672–677, 2006. 5.1, 5.4

[Lehmann *et al.* 1981] L. A. Lehmann, R. E. Alvarez, A. Macovski, W. R. Brody, N. J. Pelc, S. J. Riederer, and A. L. Hall. Generalized image combinations in dual KVP digital radiography. *Medical Physics*, 8(5):659–667, 1981. 5.1.1, 5.1.1, 5.2, 5.1, 5.2.1, 5.2.1, 5.2.3, 5.3, 5.3

[Lesage *et al.* 2008] D. Lesage, E. Angelini, I. Bloch, and G. Funka-Lea. Medial-based Bayesian tracking for vascular segmentation: Application to coronary arteries in 3D CT angiography. In *Fifth IEEE International Symposium on Biomedical Imaging: From Nano to Macro, ISBI*, pages 268–271, 2008. 3.2.1

[Li and Yezzi 2007] H. Li and A. Yezzi. Vessels as 4-D Curves: Global Minimal 4-D Paths to Extract 3-D Tubular Surfaces and Centerlines. *IEEE Transactions on Medical Imaging*, 26(9):1213–1223, 2007. 3.2.1, 3.3.1

[Lima *et al.* 2004] J. Lima, M. Desai, H. Steen, W. Warren, S. Gautam, and S. Lai. Statin-Induced Cholesterol Lowering and Plaque Regression After 6 Months of Magnetic Resonance Imaging-Monitored Therapy. *Circulation*, 110(16):2336–2341, 2004. 1.2.3

[Liu *et al.* 2002] J. Liu, Y. Pan, K. Wang, and J. Han. Mining frequent item sets by opportunistic projection. In *Proceedings of the eighth ACM SIGKDD international conference on Knowledge discovery and data mining*, pages 229–238, 2002. 6.1.1

[Lloyd-Jones *et al.* 2009] D. Lloyd-Jones, R. Adams, M. Carnethon, G. De Simone, T. B. Ferguson, K. Flegal, E. Ford, K. Furie, A. Go, K. Greenlund, N. Haase, S. Hailpern, M. Ho, V. Howard, B. Kissela, S. Kittner, D. Lackland, L. Lisabeth, A. Marelli, M. McDermott, J. Meigs, D. Mozaffarian, G. Nichol, C. O'Donnell, V. Roger, W. Rosamond, R. Sacco, P. Sorlie, R. Stafford, J. Steinberger, T. Thom, S. Wasserthiel-Smoller, N. Wong, J. Wylie-Rosett, Y. Hong, and Committee, American Heart Association Statistics and Stroke Statistics Subcommittee. Heart Disease and Stroke Statistics–2009 Update. A Report From the American Heart Association Statistics Committee and Stroke Statistics Subcommittee. *Circulation*, 119:e21–e181, 2009. 1

[Lorensen and Cline 1987] W. Lorensen and H. Cline. Marching cubes: A high resolution 3d surface construction algorithm. *ACM SIGGRAPH Computer Graphics*, 21(4):163–169, 1987. 1, 4.2

[Lorenz and von Berg 2005] C. Lorenz and J. von Berg. Fast automated object detection by recursive casting of search rays. *International Congress Series*, 1281:230–235, 2005. 3.1.1

[Lorenz *et al.* 2004a] C. Lorenz, J. Lessick, G. Lavi, T. Bulow, and S. Renisch. Fast automatic delineation of cardiac volume of interest in MSCT images. In *Proc. SPIE Int. Soc. Opt. Eng.*, volume 5370, pages 456–466, 2004. 3.1.1, 3.1.2, 3.1.2, 3.1.2

[Lorenz *et al.* 2004b] C. Lorenz, J. von Berg, T. Bulow, S. Renisch, and S. Wengandt. Modeling the coronary artery tree. In *Shape Modeling Applications*, pages 354–357, 2004. 3.4.1, 3.5

[Lu *et al.* 2002] B. Lu, M. Budoff, N. Zhuang, J. Child, H. Bakhsheshi, S. Carson, and S.-S. Mao. Causes of Interscan Variability of Coronary Artery Calcium Measurements at Electron-Beam CT. *Academic Radiology*, 9(6):654–661, 2002. 2.2

[Maddah *et al.* 2002] M. Maddah, A. Afzali-Kusha, and H. Soltanian-Zadeha. Fast center-line extraction for quantification of vessels in confocal microscopy images. In *IEEE International Symposium on Biomedical Imaging*, pages 461–464, 2002. 3.2.1

[Maehara *et al.* 2001] A. Maehara, G. Mintz, M. Castagna, A. Pichard, L. Satler, R. Waksman, J. Laird, W. Suddath, K. Kent, and N. Weissman. Intravascular ultrasound assessment of the stenoses location and morphology in the left main coronary artery in relation to anatomic left main length. *The American Journal of Cardiology*, 88(1):1–4, 2001. 6.1.1

[Marziani *et al.* 2002] M. Marziani, A. Taibi, A. Tuffanelli, and M. Gambaccini. Dual-energy tissue cancellation in mammography with quasi-monochromatic x-rays. *Physics in Medicine and Biology*, 47(2):305, 2002. 5.1.1, 5.1.1

[McCollough *et al.* 2007] C. McCollough, S. Ulzheimer, S. Halliburton, K. Shanneik, R. White, and W. Kalender. Coronary Artery Calcium: A Multi-institutional, Multimanufacturer International Standard for Quantification at Cardiac CT. *Radiology*, 243(2):527–538, 2007. 2.1.3, 2.4.1

[McPherson *et al.* 1991] D. McPherson, S. Sirna, L. Hiratzka, L. Thorpe, M. Armstrong, M. Marcus, and R. Kerber. Coronary arterial remodeling studied by high-frequency epicardial echocardiography: an early compensatory mechanism in patients with obstructive coronary atherosclerosis. *Journal of the American College of Cardiology*, 17(1):79–86, 1991. 3.3

[Medina *et al.* 2006] A. Medina, J. Suarez de Lezo, and M. Pan. A New Classification of Coronary Bifurcation Lesions. *Revista Espanola de Cardiologia*, 59(2):183–183, 2006. 5.4, 6.2.1

[Merges *et al.* 2006] R. Merges, D. Rinck, M. Sühling, O. Dössel, and M. Scheuering. Anatomical-based segmentation with stenosis bridging and gap closing in atherosclerotic cardiac MSCT. In *Proc. SPIE Int. Soc. Opt. Eng.*, volume 6144, pages 61440B–8, 2006. 3.2.1, 3.5

[Metz *et al.* 2007] C. Metz, M. Schaap, A. van der Giessen, T. van Walsum, and W. Niessen. Semi-automatic cornary artery centerline extraction in computed tomography angiography data. In *Fourth IEEE International Symposium on Biomedical Imaging: From Nano to Macro, ISBI*, pages 856–859, 2007. 3.2.1

[Millner *et al.* 1979] M. R. Millner, W. D. McDavid, R. G. Waggener, M. J. Dennis, W. H. Payne, and V. J. Sank. Extraction of information from CT scans at different energies. *Medical Physics*, 6(1):70–71, 1979. 5.1.1

[Mintz *et al.* 1997] G. Mintz, K. Kent, A. Pichard, L. Satler, J. Popma, and M. Leop. Contribution of inadequate arterial remodeling to the development of focal coronary artery stenoses. an intravascular ultrasound study. *Circulation*, 95(7):1791–1798, 1997. 3.3

[Mortensen and Barrett 1995] E. Mortensen and W. Barrett. Intelligent scissors for image composition. In *Proceedings of the 22nd annual conference on Computer graphics and interactive techniques*, pages 191–198, 1995. 3.2.2

[Motoyama *et al.* 2007a] S. Motoyama, T. Kondo, H. Anno, A. Sugiura, Y. Ito, K. Mori, J. Ishii, T. Sato, K. Inoue, M. Sarai, H. Hishida, and J. Narula. Atherosclerotic Plaque Characterization by 0.5-mm-Slice Multislice Computed Tomographic Imaging - Com-

parison With Intravascular Ultrasound. *Circulation Journal*, 71(3):363–366, 2007. 1.3.4

[Motoyama *et al.* 2007b] S. Motoyama, T. Kondo, M. Sarai, A. Sugiura, H. Harigaya, T. Sato, K. Inoue, M. Okumura, J. Ishii, H. Anno, R. Virmani, Y. Ozaki, H. Hishida, and J. Narula. Multislice Computed Tomographic Characteristics of Coronary Lesions in Acute Coronary Syndromes. *Journal of the American College of Cardiology*, 50(4):319–326, 2007. 5.1

[Mühlenbruch *et al.* 2005] G. Mühlenbruch, C. Thomas, J. Wildberger, R. Koos, M. Das, C. Hohl, M. Katoh, R. Günther, and A. Mahnken. Effect of Varying Slice Thickness on Coronary Calcium Scoring With Multislice Computed Tomography in Vitro and in Vivo. *Investigative Radiology*, 40(11):695–699, 2005. 2.4.1, 2.5

[Mühlenbruch *et al.* 2007] G. Mühlenbruch, E. Klotz, J. Wildberger, R. Koos, M. Das, M. Niethammer, C. Hohl, D. Honnef, C. Thomas, R. Günther, and A. Mahnken. The accuracy of 1- and 3-mm slices in coronary calcium scoring using multi-slice CT in vitro and in vivo. *European Radiology*, 17(2):321–329, 2007. 2.2.4, 2.6

[Nair *et al.* 2001] A. Nair, B. Kuban, N. Obuchowski, and D. Vince. Assessing spectral algorithms to predict atherosclerotic plaque composition with normalized and raw intravascular ultrasound data. *Ultrasound in Medicine & Biology*, 27(10):1319–1331, 2001. 5.1

[Nair *et al.* 2004] A. Nair, D. Calvetti, and D. Vince. Regularized autoregressive analysis of intravascular ultrasound backscatter: improvement in spatial accuracy of tissue maps. *IEEE Transactions on Ultrasonics, Ferroelectrics and Frequency Control*, 51(4):420–431, 2004. 5.1

[Nishioka *et al.* 1996] T. Nishioka, H. Luo, N. Eigler, H. Berglund, C. Kim, and R. Siegel. Contribution of inadequate compensatory enlargement to development of human coronary artery stenosis: an in vivo intravascular ultrasound study. *Journal of the American College of Cardiology*, 27(7):1571–1576, 1996. 3.3

[Nissen *et al.* 2006] S. Nissen, S. Nicholls, I. Sipahi, P. Libby, J. Raichlen, C. Ballantyne, J. Davignon, R. Erbel, J. Fruchart, J.-C. Tardif, P. Schoenhagen, T. Crowe, V. Cain, K. Wolski, M. Goormastic, E. Tuzcu, and for the ASTEROID Investigators. Effect of Very High-Intensity Statin Therapy on Regression of Coronary Atherosclerosis: The ASTEROID Trial. *Journal of the American Medical Association*, 295(13):1556–1565, 2006. 1.2.3

[Nissen 2004] S. Nissen. Seeing is believing: imaging techniques to measure atherosclerosis progression. *International Congress Series*, 1262:257–260, 2004. 1.3.2

[O'Donnell *et al.* 2001] L. O'Donnell, C.-F. Westin, W. E. Grimson, J. Ruiz-Alzola, M. Shenton, and R. Kikinis. Phase-Based User-Steered Image Segmentation. *Medical Image Computing and Computer-Assisted Intervention - MICCAI*, pages 1022–1030, 2001. 3.2.2

[Ohnesorge *et al.* 2002] B. Ohnesorge, T. Flohr, R. Fischbach, A. Kopp, A. Knez, S. Schröder, U. Schöpf, A. Crispin, E. Klotz, M. Reiser, and C. Becker. Reproducibility

of coronary calcium quantification in repeat examinations with retrospectively ECG-gated multisection spiral CT. *European Radiology*, 12(6):1532–1540, 2002. 2.2

[Ohnsorge *et al.* 2007] B. Ohnsorge, T. Flohr, C. Becker, A. Knez, and M. Reiser. *Multi-slice and Dual-source CT in Cardiac Imaging*. Springer Berlin Heidelberg, 2007. 1.3.1, 1.3.4, 1.13, 1.3.4

[Olgac *et al.* 2008] U. Olgac, V. Kurtcuoglu, S. C. Saur, and D. Poulikakos. Identification of Atherosclerotic Lesion-Prone Sites through Patient-Specific Simulation of Low-Density Lipoprotein Accumulation. In *Medical Image Computing and Computer-Assisted Intervention MICCAI*, pages 774–781, 2008. 5.4

[Ota *et al.* 2008] S. Ota, D. Deguchi, T. Kitasaka, K. Mori, Y. Suenaga, Y. Hasegawa, K. Imaizumi, H. Takabatake, M. Mori, and H. Natori. Automated anatomical labeling of bronchial branches using multiple classifiers and its application to bronchoscopy guidance based on fusion of virtual and real bronchoscopy. In *Proc. SPIE Int. Soc. Opt. Eng.*, volume 6916, pages 69160G–12, 2008. 3.4.1

[Oudkerk *et al.* 2008] M. Oudkerk, A. Stillman, S. Halliburton, W. Kalender, S. Möhlenkamp, C. McCollough, R. Vliegenthart, L. Shaw, W. Stanford, A. Taylor, P. van Ooijen, L. Wexler, and P. Raggi. Coronary artery calcium screening: current status and recommendations from the European Society of Cardiac Radiology and North American Society for Cardiovascular Imaging. *European Radiology*, 18(12):2785–2807, 2008. 2.2

[Palmer *et al.* 1999] N. Palmer, D. Northridge, A. Lessells, W. McDicken, and K. Fox. In vitro analysis of coronary atheromatous lesions by intravascular ultrasound. Reproducibility and histological correlation of lesion morphology: Reproducibility and histological correlation of lesion morhology. *European Heart Journal*, 20(23):1701–1706, 1999. 1.3.2

[Pasterkamp *et al.* 1995] G. Pasterkamp, P. Wensing, M. Post, B. Hillen, W. Mali, and C. Borst. Paradoxical arterial wall shrinkage may contribute to luminal narrowing of human atherosclerotic femoral arteries. *Circulation*, 91(5):1444–1449, 1995. 3.3

[Pei *et al.* 2001] J. Pei, J. Han, B. Mortazavi-asl, H. Pinto, Q. Chen, U. Dayal, and M. Hsu. PrefixSpan: Mining sequential patterns efficiently by prefix-projected pattern growth. In *International Conference on Data Engineering*, pages 215–224, 2001. 6.1.1

[Peters *et al.* 2008] J. Peters, O. Ecabert, C. Lorenz, J. von Berg, M. J. Walker, T. B. Ivanc, M. Vembar, M. E. Olszewski, and J. Weese. Segmentation of the heart and major vascular structures in cardiovascular CT images. In *Proc. SPIE Int. Soc. Opt. Eng.*, volume 6914, pages 691417–12, 2008. 3.3.1

[Petersilka *et al.* 2008] M. Petersilka, H. Bruder, B. Krauss, K. Stierstorfer, and T. Flohr. Technical principles of dual source CT. *European Journal of Radiology*, 68(3):362–368, 2008. 5.1.1, 5.1.1

[Pham *et al.* 2000] D. L. Pham, C. Xu, and J. L. Prince. Current Methods in Medical Image Segmentation. *Annual Review of Biomedical Engineering*, 2(1):315–337, 2000. 3.3.1

[Pisupati *et al.* 1996] C. Pisupati, L. Wolff, W. Mitzner, and E. Zerhouni. Geometric tree matching with applications to 3D lung structures. In *Proceedings of the twelfth annual symposium on Computational geometry*, pages 419–420, 1996. 3.4.1

[Pohle *et al.* 2007] K. Pohle, S. Achenbach, B. MacNeill, D. Ropers, M. Ferencik, F. Moselewski, U. Hoffmann, T. Brady, I. Jang, and W. Daniel. Characterization of non-calcified coronary atherosclerotic plaque by multi-detector row CT: Comparison to IVUS. *Atherosclerosis*, 190(1):174–180, 2007. 1.3.4

[Poon *et al.* 2007] K. Poon, G. Hamarneh, and R. Abugharbieh. Live-Vessel: Extending Livewire for Simultaneous Extraction of Optimal Medial and Boundary Paths in Vascular Images. In *Medical Image Computing and Computer-Assisted Intervention – MICCAI*, volume 4792 of *LNCS*, pages 444–451, 2007. 3.2.1, 3.2.2, 3.2.2

[Pregowski *et al.* 2006] J. Pregowski, P. Tyczynski, G. Mintz, S.-W. Kim, A. Witkowski, L. Satler, M. Kruk, R. Waksman, A. Maehara, and N. Weissman. Intravascular ultrasound assessment of the spatial distribution of ruptured coronary plaques in the left anterior descending coronary artery. *American Heart Journal*, 151(4):898–901, 2006. 6.1.1

[Prevrhal *et al.* 1999] S. Prevrhal, K. Engelke, and W. Kalender. Accuracy limits for the determination of cortical width and density: the influence of object size and CT imaging parameters. *Physics in Medicine and Biology*, 44(3):751–764, 1999. 2.1.4, 3

[Primak *et al.* 2007] A. Primak, J. Fletcher, T. Vrtiska, O. Dzyubak, J. Lieske, M. Jackson, J. Williams Jr, and C. McCollough. Noninvasive Differentiation of Uric Acid versus Non-Uric Acid Kidney Stones Using Dual-Energy CT. *Academic Radiology*, 14(12):1441–1447, 2007. 5.1.1

[Principal Investigators of CASS and their associates 1981] Principal Investigators of CASS and their associates. National heart, lung, and blood institute coronary artery surgery study. A multicenter comparison of the effects of randomized medical and surgical treatment of mildly symptomatic patients with coronary artery disease, and a registry of consecutive patients undergoing coronary angiography. *Circulation*, 63:I–1–81, 1981. 1.1.3

[Pujol *et al.* 2004] O. Pujol, P. Radeva, J. Vitria, and J. Mauri. Adaboost to Classify Plaque Appearance in IVUS Images. In *Progress in Pattern Recognition, Image Analysis and Applications*, pages 629–636, 2004. 5.1

[Pundziute *et al.* 2007] G. Pundziute, J. Schuijf, J. W. Jukema, E. Boersma, A. de Roos, E. van der Wall, and J. Bax. Prognostic Value of Multislice Computed Tomography Coronary Angiography in Patients With Known or Suspected Coronary Artery Disease. *Journal of the American College of Cardiology*, 49(1):62–70, 2007. 6.4

[Quack 2009] T. Quack. *Large-Scale Mining and Retrieval of Visual Data in a Multimodal Context*. PhD thesis, ETH Zurich, 2009. 6.1.1, 6.2.2

[Quirante Ruiz 2007] V. Quirante Ruiz. Segmentation of Coronray Arteries in MSCT Datasets Using Livewire. Master's thesis, ETH Zurich, 2007. 3.2.2

[Reiser *et al.* 2009] M. Reiser, C. Becker, K. Nikolaou, and G. Glazer, editors. *Multislice CT*. Springer Berlin Heidelberg, 2009. 1.3.4, 1.3.4

[Renard and Yongyi 2008] F. Renard and Y. Yongyi. Image analysis for detection of coronary artery soft plaques in MDCT images. In *Fifth IEEE International Symposium on Biomedical Imaging: From Nano to Macro, ISBI*, pages 25–28, 2008. 5.1, 5.4

[Rinck *et al.* 2006] D. Rinck, S. Krüger, A. Reimann, and M. Scheuering. Shape-based segmentation and visualization techniques for evaluation of atherosclerotic plaques in coronary artery disease. In *Proc. SPIE Int. Soc. Opt. Eng.*, volume 6141, pages 61410G–9, 2006. 4.1.1

[Rollano-Hijarrubia *et al.* 2006a] E. Rollano-Hijarrubia, R. Stokking, and W. Niessen. Accuracy Comparison of a 16 and 64 Multidetector-Row Computed Tomography Scanner to Image Small High-Density Structures. *Investigative Radiology*, 41(11):781–792, 2006. 2.1.4

[Rollano-Hijarrubia *et al.* 2006b] E. Rollano-Hijarrubia, R. Stokking, F. van der Meer, and W. Niessen. Imaging of Small High-Density Structures in CT: A Phantom Study. *Academic Radiology*, 13(7):893–908, 2006. 2.2, 2.2.1, 3

[Rosamond *et al.* 2008] W. Rosamond, K. Flegal, K. Furie, A. Go, K. Greenlund, N. Haase, S. Hailpern, M. Ho, V. Howard, B. Kissela, S. Kittner, D. Lloyd-Jones, M. McDermott, J. Meigs, C. Moy, G. Nichol, C. O'Donnell, V. Roger, P. Sorlie, J. Steinberger, T. Thom, M. Wilson, Y. Hong, and Committee for the American Heart Association Statistics and Stroke Statistics Subcommittee. Heart Disease and Stroke Statistics–2008 Update: A Report From the American Heart Association Statistics Committee and Stroke Statistics Subcommittee. *Circulation*, 117(4):e25–146, 2008. 1

[Ruzsics *et al.* 2008] B. Ruzsics, H. Lee, P. Zwerner, M. Gebregziabher, P. Costello, and U. Schoepf. Dual-energy CT of the heart for diagnosing coronary artery stenosis and myocardial ischemia - initial experience. *European Radiology*, 18:2414–2424, 2008. 5.1.1

[Saur *et al.* 2008a] S. C. Saur, H. Alkadhi, L. Desbiolles, G. Székely, and P. C. Cattin. Automatic Detection of Calcified Coronary Plaques in Computed Tomography Data Sets. In *Medical Image Computing and Computer-Assisted Intervention - MICCAI*, LNCS, pages 170–177, 2008. 1.4

[Saur *et al.* 2008b] S. C. Saur, C. Kühnel, T. Boskamp, G. Székely, and P. C. Cattin. Automatic Ascending Aorta Detection in CTA Datasets. In *Bildverarbeitung für die Medizin 2008*, pages 323–327, 2008. 1.4

[Saur *et al.* 2009a] S. C. Saur, H. Alkadhi, L. Desbiolles, T. J. Fuchs, G. Székely, and P. C. Cattin. Guided review by frequent itemset mining: additional evidence for plaque detection. *International Journal of Computer Assisted Radiology and Surgery*, 4(3):263–271, May 2009. 1.4

[Saur *et al.* 2009b] S. C. Saur, H. Alkadhi, L. Desbiolles, G. Székely, and P. C. Cattin. ACCURATUM: improved calcium volume scoring using a mesh-based algorithm - a phantom study. *European Radiology*, 19:591–598, 2009. 1.4

[Saur *et al.* 2009c] S. C. Saur, H. Alkadhi, L. Regazzoni, S. Eugster, G. Székely, and P. C. Cattin. Contrast Enhancement with Dual Energy CT for the Assessment of Atherosclerosis. In *Bildverarbeitung für die Medizin 2009*, 2009. 1.4

[Saur *et al.* 2009d] S. C. Saur, P. C. Cattin, L. Desbiolles, T. J. Fuchs, G. Székely, and H. Alkadhi. Prediction Rules for the Detection of Coronary Artery Plaques: Evidence from Cardiac CT. *Investigative Radiology*, 44:483–490, 2009. 1.4

[Scheffel *et al.* 2007] H. Scheffel, P. Stolzmann, T. Frauenfelder, T. Schertler, L. Desbiolles, S. Leschka, B. Marincek, and H. Alkadhi. Dual-energy contrast-enhanced computed tomography for the detection of urinary stone disease. *Investigative Radiology*, 42:823–829, 2007. 5.1.1

[Schroeder *et al.* 2001] S. Schroeder, A. Kopp, A. Baumbach, C. Meisner, A. Küttner, C. Georg, B. Ohnesorge, C. Herdeg, C. Claussen, and K. Karsch. Noninvasive detection and evaluation of atherosclerotic coronary plaques with multislice computed tomography. *Journal of the American College of Cardiology*, 37(5):1430–1435, 2001. 1.3.4, 1.3.4

[Schwarz *et al.* 2008] F. Schwarz, B. Ruzsics, U. J. Schoepf, G. Bastarrika, S. Chiaramida, J. Abro, R. Brothers, S. Vogt, B. Schmidt, P. Costello, and P. Zwerner. Dual-energy CT of the heart - Principles and protocols. *European Journal of Radiology*, 68(3):423–433, 2008. 4.1, 4.2

[Sengupta *et al.* 2005] S. Sengupta, S. Jha, D. Walter, Y. Du, and E. Tkaczyk. Dual energy for material differentiation in coronary arteries using electron-beam CT. volume 5745, pages 1306–1316. SPIE, 2005. 5.1.1

[Serra 1982] J. Serra. *Image Analysis and Mathematical Morphology*. Academic Press, 1982. 3.1.1

[Shimada *et al.* 2006] Y. Shimada, B. Courtney, M. Nakamura, Y. Hongo, S. Sonoda, A. Hassan, P. Yock, Y. Honda, and P. Fitzgerald. Intravascular Ultrasonic Analysis of Atherosclerotic Vessel Remodeling and Plaque Distribution of Stenotic Left Anterior Descending Coronary Arterial Bifurcation Lesions Upstream and Downstream of the Side Branch. *The American Journal of Cardiology*, 98:193–196, 2006. 6.1.1

[Shinohara *et al.* 2008] M. Shinohara, T. Yamashita, H. Tawa, M. Takeda, N. Sasaki, T. Takaya, R. Toh, A. Takeuchi, T. Ohigashi, K. Shinohara, S. Kawashima, M. Yokoyama, K.-i. Hirata, and A. Momose. Atherosclerotic plaque imaging using phase-contrast X-ray computed tomography. *American Journal of Physiology - Heart and Circulatory Physiology*, 294(2):H1094–1100, 2008. 1

[Slabaugh and Unal 2005] G. Slabaugh and G. Unal. Graph cuts segmentation using an elliptical shape prior. In *IEEE International Conference on Image Processing*, pages II–1222–5, 2005. 3.3.2

[Smets *et al.* 1990] C. Smets, F. van de Werf, P. Suetens, and A. Oosterlinck. An expert system for the labeling and 3D reconstruction of the coronary arteries from two projections. *The International Journal of Cardiac Imaging*, 5(2):145–154, 1990. 3.4.1

[Socher *et al.* 2008] R. Socher, A. Barbu, and D. Comaniciu. A learning based hierarchical model for vessel segmentation. In *Fifth IEEE International Symposium on Biomedical Imaging: From Nano to Macro, ISBI*, pages 1055–1058, 2008. 3.3.1

[Stary *et al.* 1992] H. Stary, D. Blankenhorn, A. Chandler, S. Glagov, W. Insull, M. Richardson, M. Rosenfeld, S. Schaffer, C. Schwartz, W. Wagner, and R. Wissler. A Definition of the Intima of Human Arteries and of Its Atherosclerosis-Prone Regions - A Report From the Committee on Vascular Lesions of the Council on Arteriosclerosis, American Heart Association. *Arteriosclerosis and Thrombosis*, 12(1):120–134, 1992. 1.2.1

[Stary *et al.* 1994] H. Stary, A. Chandler, S. Glagov, J. Guyton, W. Insull, M. Rosenfeld, S. Schaffer, C. Schwartz, W. Wagner, and R. Wissler. A Definition of Initial, Fatty Streak, and Intermediate Lesions of Atherosclerosis - A Report From the Committee on Vascular Lesions of the Council on Arteriosclerosis, American Heart Association. *Circulation*, 89(5):2462–2478, 1994. 1.2.2

[Stary *et al.* 1995] H. Stary, A. Chandler, R. Dinsmore, V. Fuster, S. Glagov, W. Insull, M. Rosenfeld, C. Schwartz, W. Wagner, and R. Wissler. A Definition of Advanced Types of Atherosclerotic Lesions and a Histological Classification of Atherosclerosis : A Report From the Committee on Vascular Lesions of the Council on Arteriosclerosis, American Heart Association. *Circulation*, 92(5):1355–1374, 1995. 1.2.2, 1.2.2

[Stary 2000] H. Stary. Natural History and Histological Classification of Atherosclerotic Lesions : An Update. *Arteriosclerosis, Thrombosis, and Vascular Biology*, 20(5):1177–1178, 2000. 1.2.2, 1.6

[Stolzmann *et al.* 2008a] P. Stolzmann, T. Frauenfelder, T. Pfammatter, N. Peter, H. Scheffel, M. Lachat, B. Schmidt, B. Marincek, H. Alkadhi, and T. Schertler. Endoleaks after Endovascular Abdominal Aortic Aneurysm Repair: Detection with Dual-Energy Dual-Source CT. *Radiology*, 249(2):682–691, 2008. 5.3

[Stolzmann *et al.* 2008b] P. Stolzmann, S. Leschka, H. Scheffel, T. Krauss, L. Desbiolles, A. Plass, M. Genoni, T. Flohr, S. Wildermuth, B. Marincek, and H. Alkadhi. Dual-source CT in step-and-shoot mode: noninvasive coronary angiography with low radiation dose. *Radiology*, 249(1):71–80, 2008. 3.3.2, 3.5, 4.2

[Stolzmann *et al.* 2008c] P. Stolzmann, H. Scheffel, K. Rentsch, T. Schertler, T. Frauenfelder, S. Leschka, T. Sulser, B. Marincek, and H. Alkadhi. Dual-energy computed tomography for the differentiation of uric acid stones: ex vivo performance evaluation. *Urological Research*, 36(3-4):133–138, 2008. 5.1.1

[Sun *et al.* 2008a] B. Sun, D. Giddens, L. R., W. Taylor, D. Weiss, G. Joseph, D. Vega, and J. Oshinski. Automatic plaque characterization employing quantitative and multicontrast MRI. *Magnetic Resonance in Medicine*, 59(1):174–180, 2008. 4.1.1

[Sun *et al.* 2008b] J. Sun, Z. Zhang, B. Lu, W. Yu, Y. Yang, Y. Zhou, Y. Wang, and Z. Fan. Identification and Quantification of Coronary Atherosclerotic Plaques: A Comparison of 64-MDCT and Intravascular Ultrasound. *American Journal of Roentgenology*, 190(3):748–754, March 2008. 1.3.4

[Sun *et al.* 2008c] Z. Sun, C. Lin, R. Davidson, C. Dong, and Y. Liao. Diagnostic value of 64-slice CT angiography in coronary artery disease: A systematic review. *European Journal of Radiology*, 67:78–84, 2008. 5.1

[Szymczak 2008] A. Szymczak. Vessel tracking by connecting the dots. In *3D Segmentation in the Clinic: A Grand Challenge II: MICCAI workshop proceedings*, 2008. 3.2.1

[Taibi *et al.* 2003] A. Taibi, S. Fabbri, P. Baldelli, C. di Maggio, G. Gennaro, M. Marziani, A. Tuffanelli, and M. Gambaccini. Dual-energy imaging in full-field digital mammography: a phantom study. *Physics in Medicine and Biology*, 48(13):1945–1956, 2003. 5.1.1

[Takahashi and Bae 2003] N. Takahashi and K. Bae. Quantification of Coronary Artery Calcium with Multi-Detector row CT: Assessing Interscan Variability with Different Tube Currents - Pilot Study. *Radiology*, 228(1):101–106, 2003. 2.2

[Tek *et al.* 2008] H. Tek, S. Gülsün, L. Grady, D. Lesage, and G. Funka-Lea. Automatic Coronary Tree Modeling. In *3D Segmentation in the Clinic: A Grand Challenge II: MICCAI workshop proceedings*, 2008. 3.2.1

[Teßmann *et al.* 2008] M. Teßmann, F. Vega-Higuera, D. Fritz, M. Scheuering, and G. Greiner. Learning-Based Detection of Stenotic Lesions in Coronary CT Data. In *Proceedings of Vision, Modeling, and Visualization*, pages 189–198, 2008. 4.1.1, 4.4, 5.1, 5.4

[Thomas *et al.* 2006] C. Thomas, G. Mühlenbruch, J. Wildberger, C. Hohl, M. Das, R. Günther, and A. Mahnken. Coronary Artery Calcium Scoring With Multislice Computed Tomography - In Vitro Assessment of a Low Tube Voltage Protocol. *Investigative Radiology*, 41(9):668–673, 2006. 2.2.3, 2.6

[Toumoulin *et al.* 2003] C. Toumoulin, C. Boldak, M. Garreau, and D. Boulmier. Coronary characterization in multi-slice computed tomography. In C. Boldak, editor, *Computers in Cardiology*, pages 749–752, 2003. 3.2.1, 4.1.1

[Ukai *et al.* 1995] Y. Ukai, N. Niki, H. Satoh, S. Watanabe, H. Ohmatsu, K. Eguchi, and N. Moriyama. An algorithm for coronary calcification diagnosis based on helical CT images. In *IEEE Nuclear Science Symposium and Medical Imaging Conference Record*, volume 3, pages 1617–1621, 1995. 4.1.1, 4.4

[Ukai *et al.* 1998] Y. Ukai, N. Niki, H. Satoh, S. Watanabe, H. Ohmatsu, K. Eguchi, and N. Moriyama. A coronary calcification diagnosis system based on helical CT images. *IEEE Transactions on Nuclear Science*, 45(6):3083–3088, 1998. 4.1.1

[Ulzheimer and Kalender 2003] S. Ulzheimer and W. Kalender. Assessment of calcium scoring performance in cardiac computed tomography. *European Radiology*, V13(3):484–497, 2003. 2.4.1

[van Andel *et al.* 2004] H. van Andel, E. Meijering, A. van der Lugt, H. Vrooman, and R. Stokking. VAMPIRE: Improved Method for Automated Center Lumen Line Definition in Atherosclerotic Carotid Arteries in CTA Data. *Medical Image Computing and Computer-Assisted Intervention - MICCAI*, pages 525–532, 2004. 3.2.1, 3.2.2

[Van Hoe *et al.* 2003] L. Van Hoe, K. De Meerleer, P. Leyman, and P. Vanhoenacker. Coronary Artery Calcium Scoring Using ECG-Gated Multidetector CT: Effect of Individually Optimized Image-Reconstruction Windows on Image Quality and Measurement Reproducibility. *American Journal of Roentgenology*, 181(4):1093–1100, 2003. 2.2

[van Velsen *et al.* 2007] E. van Velsen, W. Niessen, T. de Weert, C. de Monye, A. van der Lugt, E. Meijering, and R. Stokking. Evaluation of an improved technique for lumen path definition and lumen segmentation of atherosclerotic vessels in CT angiography. *European Radiology*, 17(7):1738–1745, 2007. 3.3.1

[Virmani *et al.* 2000] R. Virmani, F. Kolodgie, A. Burke, A. Farb, and S. Schwartz. Lessons From Sudden Coronary Death : A Comprehensive Morphological Classification Scheme for Atherosclerotic Lesions. *Arteriosclerosis, Thrombosis, and Vascular Biology*, 20(5):1262–1275, May 2000. 1.2.2

[Virmani *et al.* 2006] R. Virmani, A. P. Burke, A. Farb, and F. D. Kolodgie. Pathology of the vulnerable plaque. *Journal of the American College of Cardiology*, 47(8, Supplement 1):C13–C18, 2006. 6.1.1

[Walter *et al.* 2004] D. Walter, X. Wu, Y. Du, J. E. Tkaczyk, and W. Ross. Dual kVp material decomposition using flat-panel detectors. volume 5368, pages 29–39. SPIE, 2004. 5.1.1

[Wang and Smedby 2007] C. Wang and Ö. Smedby. Coronary Artery Segmentation and Skeletonization Based on Competing Fuzzy Connectedness Tree. In *Medical Image Computing and Computer-Assisted Intervention – MICCAI*, volume 4791 of *LNCS*, pages 311–318, 2007. 3.2.1

[Wang and Smedby 2008] C. Wang and Ö. Smedby. An Automatic Seeding Method For Coronary Artery Segmentation and Skeletonization in CTA. In *3D Segmentation in the Clinic: A Grand Challenge II: MICCAI workshop proceedings*, 2008. 3.2.1

[Wang *et al.* 2004] J. Wang, S.-L. Normand, L. Mauri, and R. Kuntz. Coronary Artery Spatial Distribution of Acute Myocardial Infarction Occlusions. *Circulation*, 110(3):278–284, 2004. 6.1.1

[Watanabe *et al.* 2009] Y. Watanabe, K. Uotani, T. Nakazawa, M. Higashi, N. Yamada, Y. Hori, S. Kanzaki, T. Fukuda, T. Itoh, and H. Naito. Dual-energy direct bone removal CT angiography for evaluation of intracranial aneurysm or stenosis: comparison with conventional digital subtraction angiography. *European Radiology*, 19(4):1019–1024, 2009. 5.1.1

[Wesarg and Firle 2004] S. Wesarg and E. Firle. Segmentation of vessels: the corkscrew algorithm. volume 5370, pages 1609–1620. SPIE, 2004. 3.3.1

[Wesarg *et al.* 2006] S. Wesarg, M. Khan, and E. Firle. Localizing Calcifications in Cardiac CT Data Sets Using a New Vessel Segmentation Approach. *Journal of Digital Imaging*, 19(3):249–257, 2006. 4.1.1, 4.4

[Wörz and Rohr 2007] S. Wörz and K. Rohr. Segmentation and Quantification of Human Vessels Using a 3-D Cylindrical Intensity Model. *IEEE Transactions on Image Processing*, 16(8):1994–2004, 2007. 3.3.1

[Wright and Sittig 2006] A. Wright and D. Sittig. Automated development of order sets and corollary orders by data mining in an ambulatory computerized physician order entry system. *AMIA Annual Symposium Proceedings*, pages 819–823, 2006. 6.1.1

[Yang *et al.* 2007] Y. Yang, A. Tannenbaum, D. Giddens, and A. Stillman. Automatic segmentation of coronary arteries using bayesian driven implicit surfaces. In *Fourth IEEE International Symposium on Biomedical Imaging: From Nano to Macro, ISBI*, pages 189–192, 2007. 3.3.1

[Yoon *et al.* 1997] H.-C. Yoon, L. Greaser, R. Mather, S. Sinha, M. F. McNitt-G., and J. Goldin. Coronary artery calcium: Alternate methods for accurate and reproducible quantitation. *Academic Radiology*, 4(10):666–673, 1997. 2.1.3

[Yoon *et al.* 2000] H.-C. Yoon, J. Goldin, L. Greaser, J. Sayre, and G. Fonarow. Interscan Variation in Coronary Artery Calcium Quantification in a Large Asymptomatic Patient Population. *American Journal of Roentgenology*, 174(3):803–809, 2000. 2.2

[Zambal *et al.* 2008] S. Zambal, J. Hladuvka, A. Kanitsar, and K. Bühler. Shape and Appearance Models for Automatic Coronary Artery Tracking. In *3D Segmentation in the Clinic: A Grand Challenge II: MICCAI workshop proceedings*, 2008. 3.2.1

[Zheng *et al.* 2008] L. Zheng, J. Yu, J. Li, X. Li, Y. Luo, B. Hasimu, Z. Sun, Y. Sun, and D. Hu. Prevalence of and risk factors for peripheral arterial disease among Chinese hypertensive patients with and without known cardiovascular disease. *Acta Cardiologica*, 63(6):693–699, 2008. 1.2.2

[Zhu *et al.* 2008] H. Zhu, Z. Ding, R. Piana, T. Gehrig, and M. Friedman. Cataloguing the geometry of the human coronary arteries: A potential tool for predicting risk of coronary artery disease. *International Journal of Cardiology*, page in press, 2008. 6.4

Curriculum Vitae

Personal Data

Name	Stefan Saur
Date of birth	1^{st} December 1979
Place of birth	Buchen (Odenwald), Germany
Citizenship	German

Education

2005 – 2009	*ETH Zurich, Computer Vision Laboratory, Switzerland*
	Doctoral studies
2004	*National University of Singapore, Singapore*
	Semester abroad
2000 – 2005	*University of Karlsruhe, Germany*
	Studies of Electrical Engineering and Information Technology
	Graduation with the degree Dipl.-Ing.
1990 – 1999	*Ganztagsgymnasium Osterburken, Germany*

Work Experience

2005 – 2008	*ETH Zurich, Computer Vision Laboratory, Switzerland*
	Teaching and research assistant
2000 – 2005	*Siemens AG, Germany*
	Several internships, semester project, and master thesis
2001 – 2009	*Webdesign, self-employed*

Awards

2004 *Baden-Württemberg Stipendium*, Landesstiftung Baden-Württemberg, Germany
2000 *IPP award*, University of Karlsruhe, Germany